A Measurement of the Polarization Asymmetry of the Tau Lepton Using the L3 Detector at LEP

Doris Yangsoo Kim

A dissertation submitted to

The Johns Hopkins University

in conformity with the requirements for the degree of
Doctor of Philosophy

Baltimore, Maryland
1996

Abstract

With a data sample of 58,000 $e^-e^+ \to \tau^-\tau^+(\gamma)$ events collected in the L3 detector at LEP during 1994, we did a measurement of the polarization of τ leptons as a function of the τ^- production polar angle with respect to the incident e^- beam direction. We used the following 1-prong τ decay channels: $\tau^- \to e^-\overline{\nu}_e\nu_\tau$, $\tau^- \to \mu^-\overline{\nu}_\mu\nu_\tau$, $\tau^- \to \pi^-\nu_\tau$, $\tau^- \to \rho^-\nu_\tau$, and $\tau^- \to a_1^-\nu_\tau$. As the result, we obtained the asymmetries $\mathcal{A}_\tau = 0.156 \pm 0.017 \pm 0.009$ and $\mathcal{A}_e = 0.155 \pm 0.025 \pm 0.005$.

Combining this with the previous 1990-1993 data measurement by L3, we obtained $\mathcal{A}_\tau = 0.152 \pm 0.010 \pm 0.009$, and $\mathcal{A}_e = 0.156 \pm 0.016 \pm 0.005$. These asymmetries gave the ratio of vector to axial-vector weak neutral coupling constants for electrons as $g_V^e/g_A^e = 0.0787 \pm 0.0078 \pm 0.0025$ and for taus as $g_V^\tau/g_A^\tau = 0.0763 \pm 0.0051 \pm 0.0044$. The numbers are consistent with the hypothesis of $e - \tau$ lepton universality. Assuming the $e - \tau$ neutral current universality, the effective electroweak mixing angle is calculated as $\sin^2\theta_w^{\rm eff} = 0.2308 \pm 0.0013$.

Advisor: Professor Aihud Pevsner

Acknowledgment

I'm grateful that I was given this unusual opportunity of participating in the L3 experiment at LEP as a member of the Johns Hopkins group. It was God's blessing that I could make a contribution in high energy physics. I'd like to give my appreciation to Prof. Aihud Pevsner and Prof. Peter Fisher. They showed me the road to this exciting field of physics and provided me of the excellent view on nature. I'd like to give thanks to Prof. Chih-Yung Chien and Dr. Andreas Gougas from the Johns Hopkins University, who supported me and gave me a constant encouragement.

I'd like to give thanks to the tau group people of the L3 experiment. Without them, it would have been impossible to understand one of the most complex machines in the world. Especially, I'd like to thank Dr. Andrei Kunin, who gave me valuable pieces of advice and consultation during my analysis without limit. I'd like to thank Dr. Tom Paul, Prof. John Swain, and Dr. Jayant Shukla in their willingness to discuss about the tau physics with me. Also Dr. Ivan Korolko, Mr. Ronald Moore, Dr. Werner Lustermann, Dr. Lucas Taylor, Dr. Igor Vorobiev, Dr. Maurizio Biasini, Dr. Pavel Kapinos, Dr. David McNally and Dr. James Gerald gave me valuable help whenever it was necessary. I'd like to thank my fellows in the tau group, Mr. Tome Anticic, Dr. Simonetta Gentile, Mr. Frank Ziegler, Prof. Maria Teresa Dova, Prof. Richard Mount and Mr. Reinhold Voelkert. We've held interesting discussions about the nature of the tau lepton. Moreover, I would thank Dr. Martin Pohl and Prof. Wolfgang Lohmann of the tau group. I received gracious supports from them.

Also I have to thank people of the L3 analysis group. Their help was essential in my analysis. I'm grateful to Dr. David Sticklan, Dr. Vincenzo Innocente, Dr. Ghita Hahal-Callot, Dr. Juan Alcaraz, Dr. Tofiqh Azemoon, Dr. Sudanda Banerjee, Dr. Bruna Bertucci, Dr. Dimitri Bourilkov, Mr. Vuco Brigljevic, Dr. Ingrid Clare, Dr. Robert Clare, Dr. Dominique Duchesneau, Dr. Sajan Easo, Dr. Martin W. Gruenewald, Dr. Paul de Jong, Dr. Christopher Paus, Dr. Marco Pieri, Mr. Juan Pinto, Prof. Howard Stone, Mr. Chris Tully, and Dr. Ulrich Uwer.

Without the effort from the L3 online group, there would be no data we could analyze. I learned valuable basics from the online people about the L3 detector itself. I'd like to give special thanks to Prof. Jean-Jaques Blaising, Prof. Hans Anderhup, Dr. Michael MacDermott and Prof. Rudolf Leiste in helping me understand the L3 online software and the overall online structure. I'd like to thank my fellow TEC people, Prof. Botio Betev, Mr. Lubomir Djambazov, Dr. Hanna

Nowak, Dr. Peter Schmitz, Dr. Henry Suter, Dr. Frank Tonisch, Dr. Peter Levtchenko and Dr. Joachim Mnich. It was a pleasure to learn from them about the function of the central tracking system. I'd like to appreciate my colleagues in the SMD group. There I learned lessons of the detector construction. I'm giving thanks to Prof. Roberto Battiston, Dr. Jon Kapustinsky, Dr. Leonello Servoli, Dr. Giovanni Passaleva, Dr. Giovanni Ambrosi, Prof. Nicolas Produit, Dr. Oscar Adriani and Prof. Raymond Weill. Again I'm grateful for technical assistant from Mr. Ferninando Dalla Santa, Mr. Erick Lejeune and Mr. Pierre-Alain Baehler.

I'd like to give tribute to Prof. S.C.C. Ting. His excellent leadership is vital to the L3 group. And I'm thankful for the supreme performance of the LEP group.

Finally, I would appreciate Prof. Gordon Feldman, Prof. Leon Madansky, Prof. Gerard Meyer and Prof. Warner Love from the Johns Hopkins University. It was a delight to exchange views with them about the nature of my analysis. I'd like to give thanks to Prof. Chung W. Kim and Ms. J.H. Song of the Johns Hopkins University for their kind encouragements. In addition, I have to remember the cheerful encouragement of my family, my friends and the JHU high energy group people during my years in the Johns Hopkins University. I give my thanks to them collectively.

Contents

1 Introduction **1**

2 τ Polarization in the Standard Electroweak Model **3**
2.1 The Standard Electroweak Model 3
2.2 Asymmetries in the $e^+e^- \to \tau^+\tau^-$ Interaction 10
2.3 Radiative Corrections 12
2.4 Discovery of the Tau Lepton 12

3 The Experimental Method **14**
3.1 Polarization in $\tau^- \to \pi^-\nu_\tau$ Channel 14
3.2 Polarization in $\tau^- \to e^-\overline{\nu}_e\nu_\tau$ and in $\tau^- \to \mu^-\overline{\nu}_\mu\nu_\tau$ 18
3.3 Polarization in $\tau^- \to \rho^-\nu_\tau$ 18
3.4 Polarization in $\tau^- \to a_1^-\nu_\tau$ 20
3.5 Sensitivity 21

4 The L3 Detector **24**
4.1 The Magnet 26
4.2 The Central Tracking System 28
4.3 The Electromagnetic Calorimeter 32
4.4 The Scintillators 34
4.5 The Hadron Calorimeter and the Muon Filter 35
4.6 The Muon Spectrometer 36
4.7 The Luminosity Monitor 38
4.8 The Trigger 40
4.9 The Offline Computer Facilities 43

5 Data Analysis **45**
5.1 Detector Alignment 46
5.1.1 The Fill Vertex 47
5.1.2 Alignment of the BGO Calorimeter 47
5.1.3 Alignment of The Z-Chamber 48
5.2 Event Selection 48
5.2.1 Preselection 49
5.2.2 Electron Identification 50
5.2.3 Selection of $\tau^- \to e^- \overline{\nu}_e \nu_\tau$ 51
5.2.4 Muon Identification 52
5.2.5 Selection of $\tau^- \to \mu^- \overline{\nu}_\mu \nu_\tau$ 52
5.2.6 Selection of $\tau^- \to \pi^- \nu_\tau$ 53
5.2.7 Neutral Pion (Photon) Identification in Hadronic τ Decay . 54
5.2.8 Selection of $\tau^- \to \rho^- \nu_\tau$ 56
5.2.9 Selection of $\tau^- \to a_1^- \nu_\tau$ 58

6 Energy Scale and Resolution **60**
6.1 Energy Determination of Electrons and Neutral Particles 60
6.2 Momentum Determination of Muons 60
6.3 Energy Determination of Charged Pions 62
6.3.1 TEC Momentum Resolution 62
6.3.2 The Calorimeter Gains 63

7 The Measurement of τ Polarization **65**
7.1 The Fitting Method 65
7.2 Charge Assignment 67
7.3 The Measurement of τ Polarization 68
7.3.1 Fitting in $\tau^- \to e^- \overline{\nu}_e \nu_\tau$ 68
7.3.2 Fitting in $\tau^- \to \mu^- \overline{\nu}_\mu \nu_\tau$ 69
7.3.3 Fitting in $\tau^- \to \pi^- \nu_\tau$ 70
7.3.4 Fitting in $\tau^- \to \rho^- \nu_\tau$ 71
7.3.5 Fitting in $\tau^- \to a_1^- \nu_\tau$ 74
7.4 The Measurement of $\mathcal{A}_e$ and $\mathcal{A}_\tau$ 74

8 Conclusion and Discussion **78**
8.1 Conclusion 78
8.2 Discussion 80

A Helicity **83**

B The TEC Momentum Resolution with SMD Hits **85**

List of Figures

3.1 (a) Two helicity states of τ^- in its rest frame when it decays into $\pi^-\nu_\tau$. The bold arrow indicates the spin state (or handedness) of each particle. Spin of π^- is 0. ν_τ is always left-handed. (b) The expected energy spectra of π^- generated from τ^- according to helicity of τ^-, without the detector effect in the LEP frame. The shape of the spectra is resulted from angular momentum preservation. . . . 15

3.2 (a) Two cases of the spin distribution in the τ^- rest frame when τ decays in lepton modes and its helicity is positive. The first case shows when two neutrinos head in the same direction, the second case shows when they head in the opposite direction each other. (b) The expected energy spectra of e^- and μ^- generated from τ^- according to its helicity, without the detector effect in the LEP frame. 17

3.3 (a) Two helicity states of ρ^- in the τ^- rest frame, when helicity of τ^- is $+1/2$. The bold arrow indicates the spin state (or handedness) of each particle. ν_τ is assumed left-handed. (b) The definition of $\cos\psi^*$, the angle of π^- with respect to the ρ^- flight direction in the ρ^- rest frame. 19

4.1 A perspective view of the LEP site 25

4.2 (a) A view of L3 in $r-\phi$ plane (b) An L3 perspective view 27

4.3 (a) A TEC perspective view (b) One sector of the TEC 29

4.4 (a) A perspective view of the SMD (b) The face of the SMD in xy plane 31

4.5 (a) A BGO crystal (b) Half of the barrel detector and one endcap detector 33

4.6 The hadron calorimeter, the muon filter and the scintillator counters 35

4.7 (a) An octant of the barrel muon spectrometer (b) A profile of P-chambers from an octant (c) The forward-backward muon detector 37

4.8 The BGO calorimeter and the SLUM as the luminosity monitor . . 39
4.9 The L3 trigger structure 41

5.1 (a) An electron candidate (b) The selection efficiency of $\tau^- \to e^- \overline{\nu_e} \nu_\tau$ 50
5.2 (a) A muon candidate (b) The selection efficiency of $\tau^- \to \mu^- \overline{\nu_\mu} \nu_\tau$. 51
5.3 (a) A hadron candidate (b) The selection efficiency of $\tau^- \to \pi^- \nu_\tau$. 53
5.4 The algorithm used to separate the charged cluster and the neutral cluster in the BGO calorimeter 55
5.5 (a) The reconstructed mass of π^0 in ρ^- candidates. (b) The reconstructed mass of ρ^- candidates. 56
5.6 The selection efficiency of $\tau^- \to \rho^- \nu_\tau$ in terms of $\cos\theta^*$ and $\cos\psi^*$, the kinematic variables used in the polarization fit. Their meaning is explained in Section 3.3. 57

6.1 The energy resolution of the L3 detector for various particles. . . . 61

7.1 A cross-check of the measurement of τ polarization in $\tau^- \to e^- \overline{\nu_e} \nu_\tau$ channel. The $\mathcal{P}_\tau$ fit using the entire barrel region events is shown [49]. 68
7.2 A cross-check of the measurement of τ polarization in $\tau^- \to \mu^- \overline{\nu_\mu} \nu_\tau$ channel. The $\mathcal{P}_\tau$ fit using the entire barrel region events is shown [49]. 70
7.3 A cross-check of the measurement of τ polarization in $\tau^- \to \pi^- \nu_\tau$ channel. The $\mathcal{P}_\tau$ fit using the entire barrel region events is shown [49]. 71
7.4 A cross-check of the measurement of τ polarization in $\tau^- \to \rho^- \nu_\tau$ channel, in 4 slices of $\cos\theta^*$. The $\mathcal{P}_\tau$ fitted from the entire barrel region events. 72
7.5 $\mathcal{A}_\tau$ and $\mathcal{A}_e$ from $\tau^- \to \rho^- \nu_\tau$ channel. 73
7.6 The final $\mathcal{A}_\tau$ and $\mathcal{A}_e$ from '94 data. 75

8.1 $\mathcal{P}_\tau$-$(\cos\theta)$ from the '90-'94 combined L3 result, together with the fitted curves for $\mathcal{A}_\tau$, $\mathcal{A}_e$ and $\mathcal{A}_{e-\tau}$. The QED correction by the **ZFITTER** program is already applied. The errors at the data points include the data and MC statistics, and the systematics. . . 79

B.1 TEC momentum resolution versus the local TEC ϕ with various reconstruction options. 86

Chapter 1

Introduction

For centuries, physicists have sought the fundamental law of nature. In 20th century physics, this endeavor produced a unification theory of forces called the Standard Model. The first phase of the Standard Model, established during the 1970's, could explain the relation between the electroweak force and the masses of various particles with several parameters. Since then there has been a tremendous effort to refine and test the model, to include the strong force and the masses of quarks in a clean way.

As an e^+e^- collider, LEP at CERN has a clean interaction environment and is capable of high luminosity at the Z^0 pole. Hence, it provides an excellent opportunity to study the validity of the Standard Model. One interesting method to check the Standard Model parameters at LEP is looking at asymmetries in the $e^+e^- \to f^-f^+$ cross-sections. From the asymmetries, we can measure $\sin^2\vartheta_W$, which itself is a sensitive gauge of the Standard Model parameters and gives indirect information about the top particle mass and the Higgs particle mass. In this analysis, we study τ polarization asymmetry, one of the asymmetries in the $e^+e^- \to \tau^+\tau^-$ process, in which the spin of the outgoing τ particles can be measured from their decay kinematics, giving a second handle with which to grasp the Standard Model parameters.

According to the Standard Model, the $e^+e^- \to Z^0 \to \tau^+\tau^-$ event at the Z^0 pole is produced mostly via the neutral current channel of the electroweak interaction, which makes the outgoing τ particles polarized. In the first order, the polarization asymmetry in the process is sensitive to the vector and the axial vector coupling constants of both e and τ particles. Hence, the measurement of τ polarization provides a good opportunity to test the lepton universality hypothesis, as well as

$\sin^2 \vartheta_W$ explained in the previous article.

With the benefit of high luminosity at the LEP machine, the measurement of tau polarization at the LEP detectors leads us to a good precision test of the Standard Model and it will help us to find the road to the ultimate theory.

Chapter 2

τ Polarization in the Standard Electroweak Model

The electroweak interaction part of the Standard Model is summarized. The tau polarization measurement is explained in the context of the Standard Model parameters. The minimal Higgs particle model is assumed in this version of the Standard Model.

2.1 The Standard Electroweak Model

The Elementary Particles In modern physics, we sort out elementary particles in two groups, fermions and bosons, according to their statistical character. Two fermions cannot occupy the same eigenstate. Usually fermions are constituents of matter. Several bosons can occupy the same eigenstate. Bosons usually behave as mediators of fundamental forces, electromagnetic, strong and weak interactions. The fermions group is divided again in the lepton group and the quark group. Leptons are electrons, neutrinos and their cousins. A lepton can exit by itself naturally and can be detected separately. Quarks are named as ups, downs and their cousins. A quark cannot exist by itself and are found only as constituents of hadrons and mesons. We call a family of fermion siblings "a generation". For example, an electron and an electron neutrino comprise the first generation of the lepton group. Currently there are three generations in the fermion group. Particles of one generation have different masses from particles of the other two generations, but the physical behavior is about the same within the group. The

Table 2.1: The list of fermions and bosons

generation	leptons	quarks
1st	e, ν_e	u, d
2nd	μ, ν_μ	s, c
3rd	τ, ν_τ	b, t

interaction	bosons
electromagnetic	γ
weak	Z^0, W^+, W^-
strong	gluons
gravitational	??

elementary bosons which are mediators of forces are called gauge bosons. The gauge boson for the gravitational force is suggested theoretically but has not been found experimentally. The Higgs particle is a special type of boson. It does not mediate a force. Its existence is necessary in the Standard Model to give proper mass parameters, but it hasn't been found yet, either. Table 2.1 shows names of the elementary particles.

The U(1) Gauge Symmetry The Lagrangian density for a free Dirac electron in the spinor language is written as [1,2]:

$$\mathcal{L}_e = \bar{\psi}(x)(i\gamma^\lambda \partial_\lambda - m_e)\psi(x). \tag{2.1}$$

This simple Lagrangian is invariant under the global phase transformation. Usually, invariance of a Lagrangian under a certain symmetry implies a corresponding conservation law. But a constant phase (global) transformation does not mean much in physics, so a position dependent phase (local) transformation is tried instead.

$$\begin{array}{rcll} \psi(x) & \rightarrow & e^{i\alpha}\psi(x) & global\ transformation, \\ \psi(x) & \rightarrow & e^{i\alpha(x)}\psi(x) & local\ transformation. \end{array} \tag{2.2}$$

Since Equation 2.1 is not invariant under the local phase transformation, modification of the Lagrangian is required. One solution is to introduce vector field terms in the Lagrangian as follows:

$$\mathcal{L}'_e = \bar{\psi}(x)(i\gamma^\lambda \partial_\lambda + e\gamma^\lambda A_\lambda(x) - m_e)\psi, \tag{2.3}$$

with the local phase transformation rule,

$$\psi(x) \rightarrow e^{i\alpha(x)}\psi(x) \tag{2.4}$$

$$A_\lambda(x) \rightarrow A_\lambda(x) + \frac{1}{e}\partial_\lambda \alpha(x). \tag{2.5}$$

If we include an additional kinematic term for the vector field, $-\frac{1}{4}F_{\lambda\rho}F^{\lambda\rho}$, the new Lagrangian can describe an electron in the electromagnetic vector potential A_λ. This formalism was developed by H. Weyl, who suggested that the invariance of the Dirac field under the local phase transformation, or the U(1) gauge transformation, might be the very reason of the existence of the photon [5].

The SU(2) Gauge Symmetry β decay as a phenomenon has been known since the discovery of radiation in the late 19th century. In 1933, Fermi developed the first successful theory on β decay of nuclei, today known as the four fermion coupling interaction [4]. But it was found that his ansatz could not explain all the weak processes and another theory was required to fill the gap. In 1956, Lee and Yang suggested that parity is not conserved in weak decay processes, which was confirmed by experiments the next year [6]. In the following years, the vector − axial-vector (V - A) structure was postulated for weak processes, and the more complex theory was developed with the discovery of next generation fermions.

In typical high energy experiments, we can ignore the electron mass. A neutrino is assumed to be massless, too. Hence, we can regard electrons and neutrinos as helicity[1] eigenstates. Due to the (V - A) structure, the lepton current for electrons and neutrinos in the weak processes is written as follows:

$$\bar{\mathbf{e}}(x)\gamma_\lambda(1-\gamma_5)\nu(x). \tag{2.6}$$

We deduce from the above equation that the left-handed electron interacts with the left-handed neutrino only and not with the right-handed neutrino, and vice versa for the right-handed electron. Experiments indicate that there are only left-handed neutrinos in nature [7], so the right-handed electron does not participate in the weak processes. In the other words, the left-handed electron and the neutrino form a doublet while the right-handed electron forms a singlet in the weak interactions.

As a first step to unify the weak process and the electromagnetic process, let's ask the Lagrangian density for an electron and a neutrino written as

$$\mathcal{L}(x) = (\bar{\nu}_{e\mathbf{L}}(x), \bar{\mathbf{e}_{\mathbf{L}}}(x))\,(i\gamma^\lambda\partial_\lambda)\begin{pmatrix}\nu_{e\mathbf{L}}(x)\\ \mathbf{e}_{\mathbf{L}}(x)\end{pmatrix} + \bar{\mathbf{e}_{\mathbf{R}}}(x)i\gamma^\lambda\partial_\lambda\mathbf{e}_{\mathbf{R}}(x), \tag{2.7}$$

[1] See Appendix A for the definition of helicity and its relation to **handed**-ness. In the massless limit, a positive(/negative) helicity state can be regarded as the same as a right-handed(/left-handed) spinor state.

where

$$\begin{array}{rcl} \mathbf{e_L}(x) & = & \frac{1}{2}(1-\gamma_5)\mathbf{e}(x), \\ \mathbf{e_R}(x) & = & \frac{1}{2}(1+\gamma_5)\mathbf{e}(x). \end{array} \tag{2.8}$$

As we did with the U(1) gauge transformation, let's require invariance of the Lagrangian under the local SU(2) transformations in the weak isospin space,

$$\begin{array}{rcl} \begin{pmatrix} \nu_{e\mathbf{L}}(x) \\ \mathbf{e_L}(x) \end{pmatrix} & \rightarrow & \mathbf{U}(x) \begin{pmatrix} \nu_{e\mathbf{L}}(x) \\ \mathbf{e_L}(x) \end{pmatrix}, \\ \mathbf{e_R}(x) & \rightarrow & \mathbf{e_R}(x). \end{array} \tag{2.9}$$

In the SU(2) case, the Lagrangian becomes invariant by introducing vector fields $\mathbf{W}_\lambda$ defined by the Pauli spin matrices, generators of the SU(2) group having a field strength g:

$$\mathbf{W}_\lambda = \mathbf{W}^i_\lambda(x)\frac{\tau_i}{2} \;\; (i = 1,2,3), \tag{2.10}$$

with corresponding transformation rules. The charged current of the weak processes reveals itself at this step. If we rearrange the $\mathbf{W}$ fields with the definitions

$$\mathbf{W}^\pm_\lambda = \frac{1}{\sqrt{2}}(\mathbf{W}^1_\lambda \mp i\mathbf{W}^2_\lambda), \tag{2.11}$$

then the e–ν–W coupling term of the invariant Lagrangian becomes

$$\begin{array}{rcl} \mathcal{L}_{e\nu W} & = & -g(\bar{\nu}_{e\mathbf{L}}(x), \bar{\mathbf{e}_\mathbf{L}}(x))\,\gamma^\lambda \mathbf{W}^i_\lambda \frac{\tau_i}{2} \begin{pmatrix} \nu_{e\mathbf{L}}(x) \\ \mathbf{e_L}(x) \end{pmatrix} \\ & = & -\frac{g}{2}\{\mathbf{W}^3_\lambda\,(\bar{\nu_{e\mathbf{L}}}\gamma^\lambda\nu_{e\mathbf{L}} - \bar{\mathbf{e}_\mathbf{L}}\gamma^\lambda\mathbf{e_L}) \\ & & + \sqrt{2}\,\mathbf{W}^+_\lambda\bar{\nu_{e\mathbf{L}}}\gamma^\lambda\mathbf{e_L} + \sqrt{2}\,\mathbf{W}^-_\lambda\bar{\mathbf{e}_\mathbf{L}}\gamma^\lambda\nu_{e\mathbf{L}}\}. \end{array} \tag{2.12}$$

The terms including $\mathbf{W}^\pm$ have the (V - A) structure, and $\mathbf{W}^\pm$ fields act as charge raising/lowering operators, hence the name of the charged current.

The next step is to introduce an additional vector field $\mathbf{B}$ with a corresponding field strength g' to make the Lagrangian invariant under U(1) phase transformation. Considering the fact that the left-handed and the right-handed electron should couple with photon fields by the same strength, we obtain the following Lagrangian after some algebra:

$$\mathcal{L}' = -\frac{g}{\sqrt{2}}(\mathbf{W}^+_\lambda\bar{\nu_{e\mathbf{L}}}\gamma^\lambda\mathbf{e_L} + \mathbf{W}^-_\lambda\bar{\mathbf{e}_\mathbf{L}}\gamma^\lambda\nu_{e\mathbf{L}})$$

$$
\begin{aligned}
&- \sqrt{g^2+g'^2}\mathbf{Z}_\lambda\{\frac{1}{2}\bar{\nu_{e\mathbf{L}}}\gamma^\lambda\nu_{e\mathbf{L}} - \frac{1}{2}\bar{\mathbf{e_L}}\gamma^\lambda\mathbf{e_L} \\
&+ \sin\vartheta_W(\bar{\mathbf{e_L}}\gamma^\lambda\mathbf{e_L} + \bar{\mathbf{e_R}}\gamma^\lambda\mathbf{e_R})\} \\
&+ \frac{gg'}{\sqrt{g^2+g'^2}}\mathbf{A}_\lambda(\bar{\mathbf{e_L}}\gamma^\lambda\mathbf{e_L} + \bar{\mathbf{e_R}}\gamma^\lambda\mathbf{e_R}).
\end{aligned} \tag{2.13}
$$

Where $\mathbf{A}, \mathbf{Z}, \sin\vartheta_W, \cos\vartheta_W$ are defined as follows:

$$\mathbf{A}_\lambda = \sin\vartheta_W\mathbf{W}^3_\lambda + \cos\vartheta_W\mathbf{B}_\lambda, \tag{2.14}$$

$$\mathbf{Z}_\lambda = \cos\vartheta_W\mathbf{W}^3_\lambda - \sin\vartheta_W\mathbf{B}_\lambda, \tag{2.15}$$

$$\sin\vartheta_W = \frac{g'}{\sqrt{g^2+g'^2}}, \tag{2.16}$$

$$\cos\vartheta_W = \frac{g}{\sqrt{g^2+g'^2}}. \tag{2.17}$$

$\mathbf{Z}_\lambda$ represents another aspect of the weak processes in the Lagrangian, named the neutral current field. $\mathbf{A}_\lambda$ couples to $\mathbf{e_L}$ and $\mathbf{e_R}$ in the same way. If $\mathbf{A}_\lambda$ remains massless, it will behave in the same way as $\mathbf{A}_\lambda$ of the U(1) gauge symmetry and become the electromagnetic field. Therefore, we conclude the relations between the field strengths as follows:

$$e = g\sin\vartheta_W = g'\cos\vartheta_W. \tag{2.18}$$

Thus, starting from β decay, we can explain the origin of the electromagnetic field and the weak processes by the SU(2) $\times$ U(1) gauge transformation. This was first done by Glashow in 1961 [8]. Still all the gauge fields and Dirac particles described in 2.13 are massless, which is not true except in the case of the electromagnetic field. Since the weak interaction is a short-range force, the weak gauge bosons $W^\pm$ and B should have masses. Simply adding gauge boson masses in 2.13 does not solve the problem, because such terms are not renormalizable.

Spontaneous Symmetry Breaking Several years later after Glashow's work, Weinberg and Salam found one possible solution to the mass paradox of 2.13, by introducing spontaneous symmetry breaking [9, 10]. Sometimes in nature, the equation describing a system has a certain symmetries even though its ground states do not show them. The symmetries of the Hamiltonian results into degenerate ground states. This phenomenon is called spontaneous symmetry breaking.

One example is a ferromagnet. Its Hamiltonian is rotationally invariant, but the ground state below the Curie temperature has a particular spin direction. If we rotate the spin of a ground state by a certain angle, it becomes another ground state, different from the previous.

Let's assume that our vacuum is described by a complex scalar field.

$$\mathcal{L} = (\partial_\mu \phi)(\partial^\mu \phi^*) - V(\phi, \phi^*). \tag{2.19}$$

(Neither by a vector nor by a tensor field since we haven't detected any "spin" of the vacuum.) If we require that the potential should be invariant under the global U(1) gauge transformation and renormalizable, then

$$V(\phi, \phi^*) = \mu^2 \phi\phi^* + \frac{1}{4}\lambda(\phi\phi^*)^2. \tag{2.20}$$

When μ^2 is negative and λ is positive, V will be a minimum at $\phi = \phi_c$ with

$$|\phi_c|^2 = -2\frac{\mu^2}{\lambda}. \tag{2.21}$$

Since Equation 2.21 does not fix the phase of ϕ field, there will be a circle of the degenerate states, in the other words, we break the symmetry. The physically meaningful field will be rather the perturbation from the ground state then the ground state itself. The equation of the perturbation turns out to be a system of two particles, one massive and the other massless. The massless particle is called a Goldstone boson.

As before, let's try the local U(1) gauge invariant Lagrangian for the complex scalar field:

$$\begin{aligned} \mathcal{L} &= (\partial_\mu + iqA_\mu)\phi(\partial_\mu - iqA_\mu)\phi^* \\ &\quad - \mu^2\phi\phi^* - \frac{1}{4}\lambda(\phi\phi^*)^2 - \frac{1}{4}F_{\mu\nu}F^{\mu\nu}. \end{aligned} \tag{2.22}$$

When the symmetry is broken, the Lagrangian will be described by two perturbation fields and one gauge field A. We can transform the Lagrangian with a special gauge such that all the terms concerning the Goldstone boson disappear and a mass term for the gauge field A appears. In other words, the degree of freedom is transferred from the Goldstone to the gauge field. This procedure is called the Higgs mechanism [11].

To generate masses for W and Z bosons, Weinberg and Salam introduced the Higgs mechanism. The simplest version requires isodoublet complex fields. Before the symmetry is broken, the isodoublet Higgs fields has four degrees of freedom. After the symmetry is broken, three massless Goldstone boson are "eaten" by W and Z bosons, generating the masses for them. The remaining degree of freedom is the so-called the Higgs particle, the massive part from the original perturbation fields.

$$\begin{aligned} m_W^2 &= \frac{e^2\rho_0^2}{4\sin^2\vartheta_W}, \\ m_Z^2 &= \frac{e^2\rho_0^2}{4\sin^2\vartheta_W\cos^2\vartheta_W}, \end{aligned} \tag{2.23}$$

$$m_H^2 = 2\lambda\rho_0^2. \tag{2.24}$$

The masses of fermions are generated at the same time. The interaction between the Higgs fields and fermions can be described by a Yukawa coupling:

$$\mathcal{L}_{Yuk} = -c_e \bar{\mathbf{e}_\mathbf{R}}(\phi_1,\phi_2)^\dagger \begin{pmatrix} \nu_{e\mathbf{L}} \\ \mathbf{e_L} \end{pmatrix} + h.c.. \tag{2.25}$$

After the symmetry breaking which gives the vacuum expectation value of the Higgs fields,

$$< 0|\phi(x)|0 >= \begin{pmatrix} 0 \\ \frac{1}{\sqrt{2}}\rho_0 \end{pmatrix}, \tag{2.26}$$

the Yukawa term transforms into $-c_e\frac{\rho_0}{\sqrt{2}}\bar{\mathbf{e}}\mathbf{e}$, generating the mass term for the electron.

$\sin^2\vartheta$ and Quantum Correction Equation 2.23 is obtained by the tree level standard electroweak calculation. In fact, $\sin^2\vartheta$ is subject to corrections coming from other interactions. For example, W and Z bosons can interact with the virtual heavy quarks, the Higgs field, etc [12]. Hence, $\sin^2\vartheta$ with correction terms can be an indirect analyzer to the top quark and the Higgs particle mass. Usually, the correction to $\sin^2\vartheta$ is expressed as follows:

$$\sqrt{2}\,G_\mu m_Z^2\cos^2\vartheta\sin^2\vartheta = \pi\alpha\frac{1}{1-\Delta r(m_t,m_H)}, \tag{2.27}$$

where G_μ, m_Z^2, α are well known quantities and m_t is the mass of a top quark. The leading correction term in Δr coming from top quarks depends on the square

of the top quark mass, while the term coming from the Higgs field depends on the logarithm of the Higgs particle mass. So the correction term is more sensitive to the top quark mass than the Higgs particle mass.

2.2 Asymmetries in the $e^+e^- \rightarrow \tau^+\tau^-$ Interaction

In the LEP I experiment, the total energy of the incoming beams is about the Z^0 mass, so the primary interaction channels in the $ee \rightarrow ff$ processes are the weak neutral current interaction and the photon exchange interaction. In addition to the Z lineshape study, an interesting way to extract the Standard Model numbers from these processes is to measure the forward-backward asymmetry, A_{FB} [13],

$$A_{FB} = \frac{\sigma_F - \sigma_B}{\sigma_F + \sigma_B}. \tag{2.28}$$

If we ignore the mass of the fermions and the $(\Gamma_Z/M_Z)^2$ terms in the first order Born cross-section, A^0_{FB} is simply

$$A^0_{FB} = \frac{3}{4}\mathcal{A}_e\mathcal{A}_\tau, \tag{2.29}$$

where A_e, A_τ are parameterizations of the Standard Model numbers,

$$\mathcal{A}_f = \frac{2v_f a_f}{v_f^2 + a_f^2} = \frac{2(1 - 4|q_f|\sin\vartheta_W^2)}{1 + (1 - 4|q_f|\sin\vartheta_W^2)}. \tag{2.30}$$

v_f^2 and a_f^2 are vector and axial-vector coupling constants of the corresponding fermion to the $\mathbf{Z}_\lambda$ field and defined as follows:

$$v_f = \frac{I_3^f - 2\sin^2\vartheta_W\, Q_f}{2\sin\vartheta_W\, \cos\vartheta_W}, \tag{2.31}$$

$$a_f = \frac{I_3^f}{2\sin\vartheta_W\, \cos\vartheta_W}, \tag{2.32}$$

where I_3^f and Q_f are the weak isospin and the charge of the fermion, respectively.

In reality, this simple expression is subject to large radiative corrections and interference terms:

$$A_{FB} = A^0_{FB} + \triangle A^{Correction}_{FB} \tag{2.33}$$

Also, A_{FB} depends heavily on the center of mass energy $\sqrt{s}$ around the Z^0 resonance, causing technical problems.

In the $e^+e^- \to \tau^+\tau^-$ process, spin of the outgoing τ particles can be measured from their decay kinematics, generating another kind of asymmetry called τ polarization asymmetry, A_{pol} [14–16] or $\mathcal{P}_\tau(\cos\theta)$. Since an outgoing τ has energy around 45 GeV, it is of negligible mass and it is considered in a helicity eigenstate. Measuring A_{pol} is more difficult than measuring A_{FB}, but A_{pol} suffers less from the radiative corrections and $\sqrt{s}$ dependency. The first order Born differential cross-section and A_{pol} are written as follows, where p is the τ^- longitudinal helicity[2]:

$$\begin{aligned}\frac{d\sigma_{Born}}{d\cos\theta}(s,\cos\theta,p) &= (1+\cos^2\theta)F_0(s) + 2\cos\theta F_1(s) \\ &\quad + p\,((1+\cos^2\theta)F_2(s) + 2\cos\theta F_3(s)),\end{aligned} \tag{2.34}$$

$$\begin{aligned}A_{pol}^{Born}(s,\cos\theta) &= -\frac{d\sigma^{Born}(\cos\theta,p=+1) - d\sigma^{Born}(\cos\theta,p=-1)}{2d\sigma^{Born}(\cos\theta,p=0)} \\ &= -\frac{(1+\cos^2\theta)F_2(s) + 2\cos\theta F_3(s)}{(1+\cos^2\theta)F_0(s) + 2\cos\theta F_1(s)}.\end{aligned} \tag{2.35}$$

The form factors used are defined as follows:

$$\begin{aligned}F_0(s) &= \tfrac{\pi\alpha^2}{2s}\ (q_e^2q_\tau^2 + 2Re\,\chi(s)q_eq_\tau v_ev_\tau + |\chi(s)|^2(v_e^2+a_e^2)(v_\tau^2+a_\tau^2)), \\ F_1(s) &= \tfrac{\pi\alpha^2}{2s}\ (2Re\,\chi(s)q_eq_\tau a_ea_\tau + |\chi(s)|^2 2v_ea_e2v_\tau a_\tau), \\ F_2(s) &= \tfrac{\pi\alpha^2}{2s}\ (2Re\,\chi(s)q_eq_\tau v_ea_\tau + |\chi(s)|^2(v_e^2+a_e^2)2v_\tau a_\tau), \\ F_3(s) &= \tfrac{\pi\alpha^2}{2s}\ (2Re\,\chi(s)q_eq_\tau a_ev_\tau + |\chi(s)|^2 2v_eq_e(v_\tau^2+a_\tau^2)),\end{aligned} \tag{2.36}$$

with

$$\chi(s) = \frac{s}{s - M_Z^2 + is\Gamma_Z/M_Z}. \tag{2.37}$$

As in the case of A_{FB}, Equation 2.35 can be simplified at the Z^0 resonance,

$$A_{pol}(\cos\theta) = \frac{\mathcal{A}_\tau + \frac{2\cos\theta}{1+\cos^2\theta}\mathcal{A}_e}{1 + \frac{2\cos\theta}{1+\cos^2\theta}\mathcal{A}_e\mathcal{A}_\tau}, \tag{2.38}$$

[2]The transverse portion of the τ spin is negligible in this analysis.

with $\mathcal{A}_f$ defined in Equation 2.30.

$\mathcal{P}_\tau(\cos\theta)$ is defined in the usual way, the difference between the positive helicity τ cross-section and the negative helicity τ cross-section, which results into $-A_{pol}(\cos\theta)$ [3]. Hence,

$$\begin{aligned} \mathcal{P}_\tau(\cos\theta) &\equiv \frac{d\sigma(\cos\theta, p=+1) - d\sigma(\cos\theta, p=-1)}{d\sigma(\cos\theta, p=+1) + d\sigma(\cos\theta, p=-1)} \\ &= -\frac{\mathcal{A}_\tau + \frac{2\cos\theta}{1+\cos^2\theta}\mathcal{A}_e}{1 + \frac{2\cos\theta}{1+\cos^2\theta}\mathcal{A}_e\mathcal{A}_\tau}. \end{aligned} \tag{2.39}$$

In the experiment we can't measure the τ direction precisely because of missing neutrinos, but the phase space of the neutrino direction is limited and $\cos\theta$ direction, on the average, can be replaced by the τ decay particle direction.

2.3 Radiative Corrections

The QED processes affect A_{pol} asymmetry either by changing the helicity of the τ lepton (the direct influence) or by deforming the final energy spectrum of the tau decay particles (the indirect influence) [14].

The effect from the initial state bremsstrahlung is negligible, since A_{pol} depends weakly on the center of mass energy, $\sqrt{s}$, and the smearing of $\sqrt{s}$ near the Z^0 pole is strongly cut off by the Z^0 line shape. The direct influence from the final state bremsstrahlung is also small, since the effect on the tau lepton helicity is of order $\frac{\alpha}{\pi} \cdot A_{pol} \sim 10^{-4}$. The indirect influence from the final state bremsstrahlung is not negligible, since photon emissions can render the energy spectrum of the tau lepton itself or that of the decay particle soft in a sizable amount.

The bias coming from the QED processes is corrected when we finalize the polarization measurement. We will refer to the method in the later chapters.

2.4 Discovery of the Tau Lepton

The existence of the third sequential lepton following an electron and a muon was postulated in the late 1960's. There had been several experimental trials to find the

[3] The sign of $A_{pol}(\cos\theta)$ is defined differently in some literatures. To avoid confusion, from now on, $\mathcal{P}_\tau(\cos\theta)$ will be used in the context, if possible.

Mode		Fraction
leptonic	$\tau^- \to e^-\nu_e\nu_\tau$	$18.01 \pm 0.18\%$
	$\tau^- \to \mu^-\nu_\mu\nu_\tau$	$17.65 \pm 0.24\%$
hadronic	$\tau^- \to \rho^-\nu_\tau$	$25.2 \pm 0.4\ \%$
	$\tau^- \to \pi^-\nu_\tau$	$11.7 \pm 0.4\ \%$
	$\tau^- \to h^- 2\pi^0\nu_\tau$	$9.6 \pm 0.4\ \%$
	$\tau^- \to h^- h^- h^+\nu_\tau$	$8.42 \pm 0.31\%$

Table 2.2: Major decay modes of τ, from the Review of Particle Properties [57]

lepton while the detailed theoretical predictions on the character and the possible decay modes of the would-be lepton were produced in the parallel [17]. The first signature of the third sequential lepton appeared in the Mark I experiment at SPEAR in 1974 [18]. The group led by Perl saw the events with the following topologies,

$$e^+e^- \to e^+\mu^- \; and \; e^+e^- \to e^-\mu^+,$$

where the outgoing electron and muon could be explained as the decay of the third sequential lepton pairs [18]. In the following years, the hadronic decay mode $\tau \to \pi + \nu$ and $\tau \to \rho + \nu$ were found and the discovery of τ as the third sequential lepton was confirmed. Table 2.4 illustrates the major decay modes of the τ particle.

Chapter 3

The Experimental Method

As mentioned in the previous chapter, the kinematic distribution of decay particles from the τ lepton is used for the measurement of τ polarization, where the distribution depends on helicity of τ, spin of the decay particles, and the number of the decay particles. In this analysis, energy of the decay particles is used as the polarization analyzer. However, due to the τ-W coupling involved in τ decay, the quantity we measure becomes $\xi \cdot \mathcal{P}_\tau$, actually. ξ is helicity of the neutrino ν_τ and defined as

$$\xi = \frac{2 g_V g_A}{(g_V)^2 + (g_A)^2}, \tag{3.1}$$

if only vector and axial vector couplings are involved between τ and W. We will assume the theory that the τ-W coupling is described by the pure $V - A$ structure, which is supported by other experiments [19]. Therefore, ξ will be fixed at -1 throughout the analysis.

The other option of the polarization analyzer is acollinearity between decay particles from two τ's. The detail of the acollinearity option is in Reference [53]. In the following sections, the relation between the decay distribution and τ helicity will be explained case by case.

3.1 Polarization in $\tau^- \rightarrow \pi^- \nu_\tau$ Channel

In this channel, τ^- decays into two particles, π^- and ν_τ. We don't observe τ^- and ν_τ visibly. But energy of τ^- is constrained by incident e^- and e^+ beam energy. Also, the available space for ν_τ momentum is constrained by the momentum con-

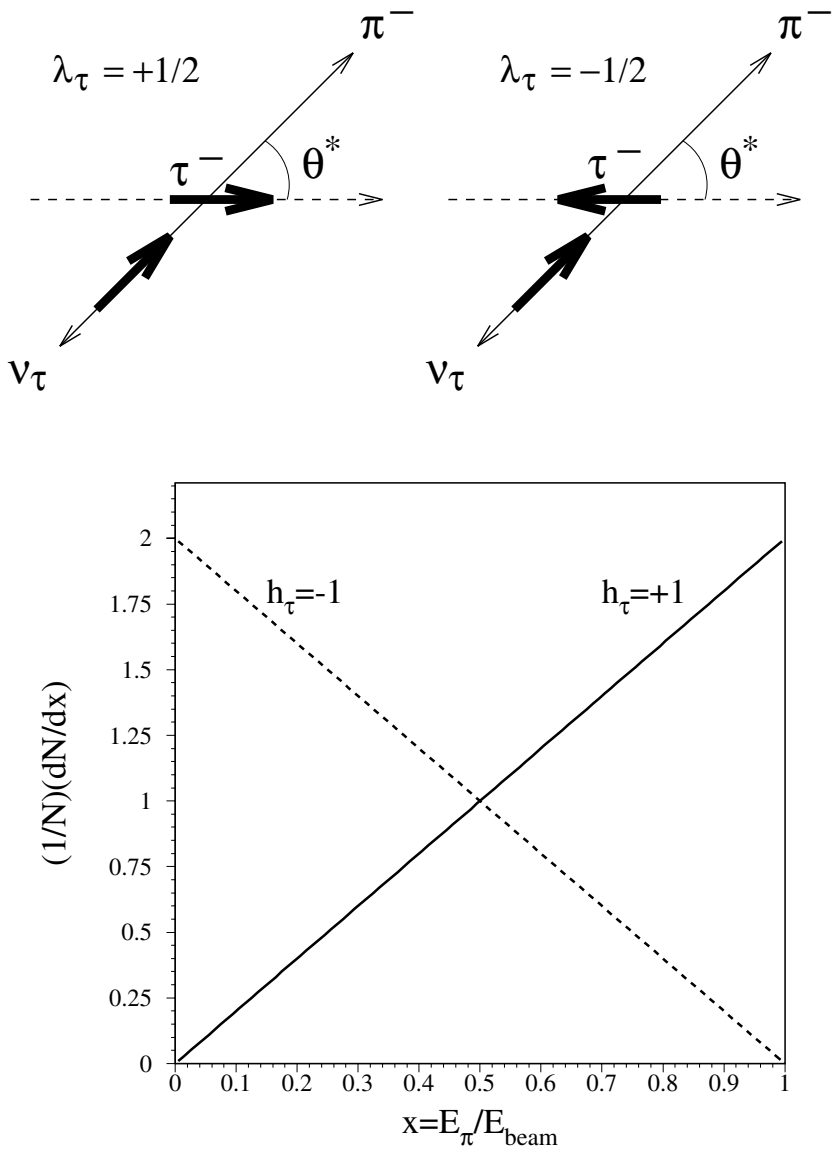

Figure 3.1: (a) Two helicity states of τ^- in its rest frame when it decays into $\pi^-\nu_\tau$. The bold arrow indicates the spin state (or handedness) of each particle. Spin of π^- is 0. ν_τ is always left-handed. (b) The expected energy spectra of π^- generated from τ^- according to helicity of τ^-, without the detector effect in the LEP frame. The shape of the spectra is resulted from angular momentum preservation.

servation rule. In the LEP frame, the movement of ν_τ is limited in a cone around the π^- direction. Hence, when we do the fit for the polarization, we can use a distribution function over which kinematic degrees of freedom from the invisible ν_τ are integrated.

Figure 3.1 (a) shows two helicity states of τ^- in its rest frame. Spin of π^- is 0, and ν_τ is assumed to be left-handed due to the V $-$ A structure. Because of the angular momentum conservation rule, π^- prefers the forward direction when the helicity of τ^- is positive and π^- prefers the backward direction when the helicity of τ^- is negative. In other words, the decay amplitudes for positive and negative helicity taus are written as

$$\begin{aligned} \mathcal{M}_{h_\tau=+1/2} &\propto d^{1/2}_{+1/2}(\theta^*) \propto \cos(\theta^*/2) \\ \mathcal{M}_{h_\tau=-1/2} &\propto d^{1/2}_{-1/2}(\theta^*) \propto \sin(\theta^*/2). \end{aligned} \tag{3.2}$$

$d^{1/2}_{+1/2}(\theta^*)$ and $d^{1/2}_{-1/2}(\theta^*)$ are the spin 1/2 rotation matrices and θ^* is the angle between the π^- flight direction and τ^- flight direction in the τ^- rest frame.

After the integration over the unknown ν_τ direction, $\cos\theta^*$ is described as

$$\cos\theta^* = \frac{2x - m_\pi^2/m_\tau^2 - 1}{(1 - m_\pi^2/m_\tau^2)(1 - m_\tau^2/E^2_{beam})^{1/2}}, \tag{3.3}$$

where x is defined as $\mathrm{E}_{\pi^-}/\mathrm{E}_{\mathrm{beam}}$ in the LEP frame. Since we can ignore m_τ with respect to $\mathrm{E}_{\mathrm{beam}}$ and m_π with respect to m_τ, $\cos\theta^*$ becomes

$$\cos\theta^* \sim 2x - 1. \tag{3.4}$$

Therefore, the energy distribution of π^- generated from τ^- decay can be written as follows [14]:

$$\begin{aligned} h(x) &= \frac{1}{N}\frac{dN}{dx} \\ &\propto \frac{1+\mathcal{P}_\tau}{2}|\mathcal{M}_{h_\tau=+1/2}|^2 + \frac{1-\mathcal{P}_\tau}{2}|\mathcal{M}_{h_\tau=-1/2}|^2 \\ &= 1 + \mathcal{P}_\tau \cdot (2x-1). \end{aligned} \tag{3.5}$$

Figure 3.1 (b) shows the expected energy spectra of π^- in the LEP frame without the detector effect. It indicates the linearity of Equation 3.5.

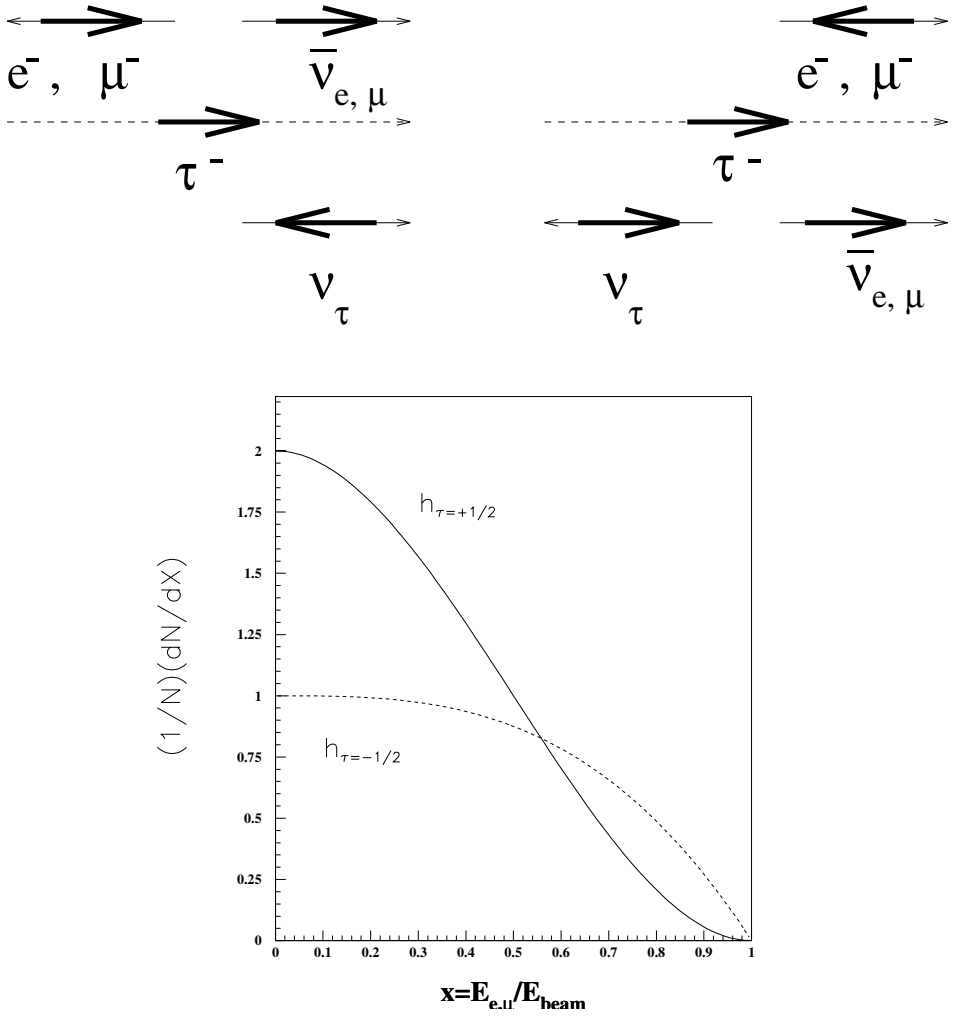

Figure 3.2: (a) Two cases of the spin distribution in the τ^- rest frame when τ decays in lepton modes and its helicity is positive. The first case shows when two neutrinos head in the same direction, the second case shows when they head in the opposite direction each other. (b) The expected energy spectra of e^- and μ^- generated from τ^- according to its helicity, without the detector effect in the LEP frame.

3.2 Polarization in $\tau^- \rightarrow e^-\overline{\nu}_e\nu_\tau$ and in $\tau^- \rightarrow \mu^-\overline{\nu}_\mu\nu_\tau$

Since there are two invisible neutrinos in these channels, sensitivity to polarization is not as good as that of the $\tau^- \rightarrow \pi^-\nu_\tau$ channel. Still, energy spectra of e^- and μ^- are sensitive to τ polarization. The energy distribution of e^- and μ^- coming from τ^- decay after we average over kinematic degrees of freedom from two neutrinos is as follows:

$$h(x) = \frac{1}{3}[(5 - 9x^2 + 4x^3) + \mathcal{P}_\tau \cdot (1 - 9x^2 + 8x^3)], \tag{3.6}$$

where x is defined as $E_{e,\mu}/E_{beam}$ and the masses of e and μ are ignored.

Figure 3.2 (a) shows two cases of the spin distribution in the τ^- rest frame when its helicity is positive. Due to the charged weak current involved in τ^- decay, e^- and μ^- are assumed left-handed. If two neutrinos head in the same direction, e^- and μ^- go in the backward direction with a strong tendency due to angular momentum conservation. If two neutrinos head in the opposite direction from each other, e^- and μ^- go in the forward direction with a weak tendency. If the helicity of the τ^- is negative, e^- and μ^- behave in just the opposite way. This tendency is shown in Figure 3.2(b), the expected energy spectra of e and μ in the LEP frame without the detector effect.

3.3 Polarization in $\tau^- \rightarrow \rho^-\nu_\tau$

This decay mode involves one neutrino, like in the $\tau^- \rightarrow \pi^-\nu_\tau$ channel. But ρ^- is a spin 1 particle, hence freedom coming from helicity of ρ^- reduces sensitivity to τ polarization. Since the total angular momentum should be conserved and ν_τ is assumed left-handed, there are two possibilities in the helicity of ρ^-, -1 and 0, with corresponding amplitudes A_1 and A_0. Figure 3.3 shows what happens when helicity of τ^- is $+1/2$. Due to angular momentum conservation, ρ^- with helicity 0 prefers the forward direction and ρ^- with helicity -1 prefers the backward direction. When helicity of τ^- is -1/2, ρ^- behaves in the opposite way. Hence, the angular distribution of ρ^- in the τ^- frame is described as,

$$\begin{aligned} \frac{1}{N}\frac{dN}{d\cos\theta^*} &\propto \frac{1+\mathcal{P}_\tau}{2}[|A_0|^2(1+cos\theta^*) + |A_1|^2(1-cos\theta^*)] \\ &\quad + \frac{1-\mathcal{P}_\tau}{2}[|A_0|^2(1-cos\theta^*) + |A_1|^2(1+cos\theta^*)] \\ &= 1 + \mathcal{P}_\tau\alpha\cos\theta^*, \end{aligned} \tag{3.7}$$

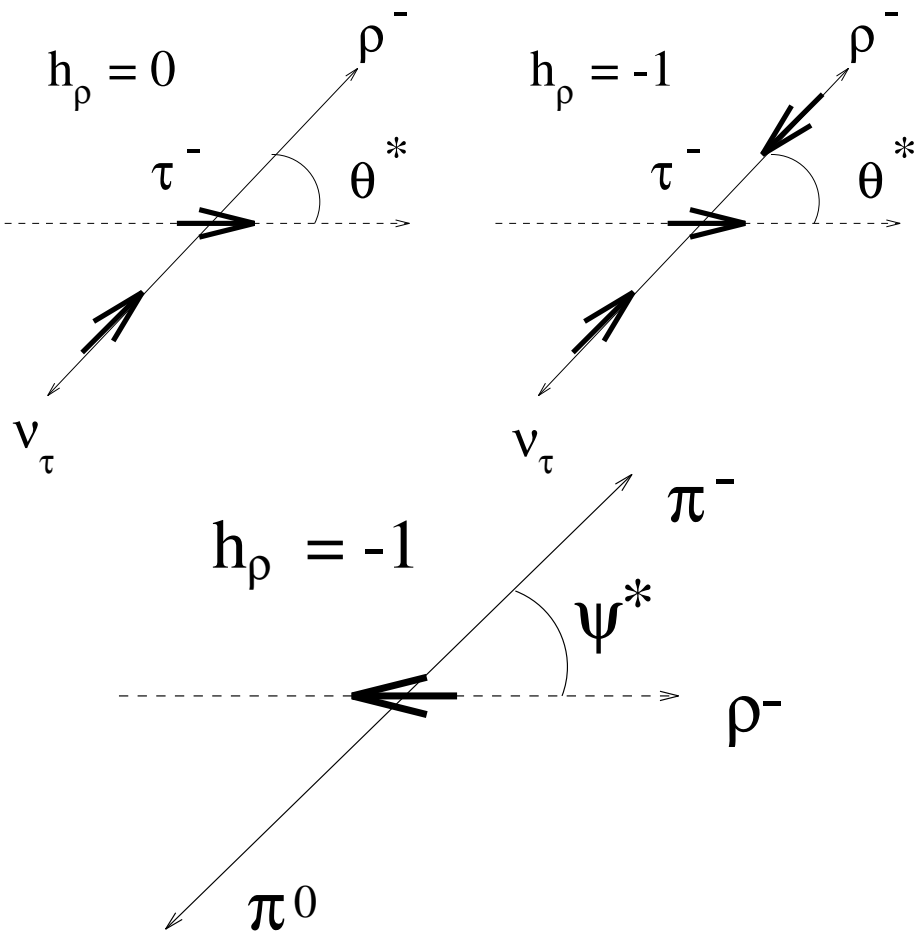

Figure 3.3: (a) Two helicity states of ρ^- in the τ^- rest frame, when helicity of τ^- is $+1/2$. The bold arrow indicates the spin state (or handedness) of each particle. ν_τ is assumed left-handed. (b) The definition of $\cos\psi^*$, the angle of π^- with respect to the ρ^- flight direction in the ρ^- rest frame.

with α defined as $(|A_0|^2 - |A_1|^2)/(|A_0|^2 + |A_1|^2)$. Since the ratio of $|A_0|/|A_1|$ is $\sqrt{2}\, m_\rho/m_\tau$ [20], α is about 0.46, contrary to the case of $\tau \to \pi^-\nu_\tau$, where α is -1.

The lost sensitivity can be recovered by looking at the decay distribution of ρ^- going into π^- and π^0 [21]. The angular distribution of π^- in the ρ^- frame depends on the helicity of ρ^-. Therefore, we fit the data with two kinematic variables, $\cos\theta^*$ and $\cos\psi^*$ to optimize the sensitivity[1]. The following equations show the definitions of $\cos\theta^*$ and $\cos\psi^*$. Approximately, $\cos\theta^* \sim \mathrm{E}_\rho/\mathrm{E}_{\mathrm{beam}}$, like in the other τ^- decay modes, and $\cos^p si^* \sim (\mathrm{E}_{\pi^-} - \mathrm{E}_{\pi^0})/\mathrm{E}_\rho$.

$$\cos\theta^* = \frac{4m_\tau^2}{m_\tau^2 - m_\rho^2}\frac{E_{\pi^0} + E_{\pi^-}}{E_{beam}} - \frac{m_\tau^2 + m_\rho^2}{m_\tau^2 - m_\rho^2} \tag{3.8}$$

$$\cos\psi^* = \frac{m_\rho}{\sqrt{m_\rho^2 - 4m_\pi^2}}\frac{E_{\pi^-} - E_{\pi^0}}{\left|\vec{P}_{\pi^-} + \vec{P}_{\pi^0}\right|}. \tag{3.9}$$

3.4 Polarization in $\tau^- \to \mathrm{a}_1^-\nu_\tau$

This decay channel behaves similarly to $\tau^- \to \rho^-\nu_\tau$, but a_1^- decays into three pions instead of two pions, either into three charged pions or into one charged pion and two neutral pions[2]. The full kinematic distribution is described by 6 variables, 3 parameters for angular and 3 parameters for mass. The angular variables are $\cos\theta^*$, $\cos\beta$ and $\cos\gamma$. θ^* is the angle of a_1^- with respect to the τ^- flight direction in the τ^- rest frame. β is the angle between the normal to the 3π decay plane and the a_1^- flight direction in the LEP frame. γ is the angle between the unlikely signed π and the projection of the a_1^- flight direction on the 3π decay plane. The mass variables are the invariant mass of 3πs, and two invariant masses of the unlikely signed *pi*s.

The problem of mass parameters for a_1^- hasn't been settled yet, nor that of the structure function of a_1^- involved in a_1^- decay [22,57]. Among 3 angular variables, γ depends on the structure function, hence, fitting with this variable will induce the systematic error coming from the structure function. It we use only the former two angular variables in the fit, the uncertainty coming from the structure function will be avoided but we lose sensitivity to τ polarization. One way to remedy

[1] It is also possible to do 1-dimensional fitting with the optimal variable.

[2] The following article is valid for both a_1^- decay modes. However, we will deal with only the 1-prong decay mode in selection and fitting. We will discuss about the 3-prong decay mode in Chapter 8.

the situation is to fit data with the 1-dimensional optimal variable [24]. The dependency on the a_1^- Breit-Wigner term is canceled out and the systematic error coming from the structure function becomes tolerable [51]. At the same time, the sensitivity stays at the same level of the full-dimensional fit. Exact formulae of the angular variables and the optimal variable can be found in Reference [23].

3.5 Sensitivity

As referred in Section 3.2, sensitivity to the τ polarization measurement is different channel by channel. Also the branching ratio of each decay channel plays a role in contribution to the measurement. The sensitivity of each decay channel can be calculated from its contribution to the statistical error of the measurement. Let's assume that σ_i is the statistical error from a particular decay channel and N_i is the number of events in the channel. Then the sensitivity of the channel, S_i, is defined as:

$$S_i^2 = \frac{1}{N_i \, \sigma_i^2}. \tag{3.10}$$

Since σ_i^2 is proportional to N_i, S_i does not depend on the number of events. If we know the branching ratio of the channel, B_i, then

$$S_i^2 = \frac{1}{N \, B_i \sigma_i^2} \tag{3.11}$$

where N is the total number of tau leptons.

Let's assume that we are using an unbinned likelihood function to fit data with the kinematic analyzers mentioned in the previous sections. In reality we use a binned likelihood function, but the approximation is enough to get the picture. The likelihood function for a particular decay channel, $\mathcal{L}_i$, will be

$$\mathcal{L}_i = \prod_j^{N_i} \mathcal{W}_i(\vec{\eta_j}, \mathcal{P}_\tau), \tag{3.12}$$

where $\mathcal{W}_i$ is normalized probability density for each event j in the i-th decay channel. Since the tau lepton cross-section is a linear function of $\mathcal{P}_\tau$, $\mathcal{W}_i$ can be written as [20]

$$\mathcal{W}_i = f_i(\vec{\eta_j}) + \mathcal{P}_\tau \cdot g_i(\vec{\eta_j}), \tag{3.13}$$

with the normalization condition $\int f_i(\vec{\eta_j})\, d\vec{\eta_j} = 1$ and the positivity condition $\int g_i(\vec{\eta_j})\, d\vec{\eta_j} = 1$.

We get the estimator of $\mathcal{P}_\tau$, $\hat{\mathcal{P}}_\tau$ by maximizing the logarithm of Equation 3.12.

$$\frac{\partial \ln \mathcal{L}_i}{\partial \mathcal{P}_\tau} = \sum_j^{N_i} \frac{g_i}{f_i + \mathcal{P}_\tau g_i} = 0. \tag{3.14}$$

The error on $\hat{\mathcal{P}}_\tau$ can be obtained from the second derivative of the logarithm,

$$\frac{1}{\sigma_i^2} = -\frac{\partial^2 \ln \mathcal{L}}{\partial \mathcal{P}_\tau^2}|_{\hat{\mathcal{P}}_\tau} = \sum_j^{N_i} \frac{g_i^2}{|f_i + \hat{\mathcal{P}}_\tau g_i|^2} \tag{3.15}$$

$$\sim N_i \int \frac{g_i^2}{|f_i + \hat{\mathcal{P}}_\tau g_i|^2} \mathcal{W} d\vec{\eta_j} \tag{3.16}$$

Hence, the sensitivity is expressed as,

$$S_i^2 = \int \frac{g_i^2}{f_i + \hat{\mathcal{P}}_\tau g_i} d\vec{\eta_j}. \tag{3.17}$$

In case of small $\mathcal{P}_\tau$, the integrand of the above equation can be solved by a Taylor series expansion. Table 3.5 shows the sensitivity of each decay channel with $\hat{\mathcal{P}}_\tau = -0.14$. It is obtained without considering event selection efficiency. The final weight of each decay channel for the polarization measurement is the sensitivity of each channel multiplied by the branching ratio. For the case of $\tau^- \to \rho^- \nu_\tau$, the result is obtained by 2-dimensional fitting with $\cos\theta^*$ and $\cos\psi^*$. For the case of $\tau^- \to a_1^- \nu_\tau$, the number is obtained by fitting with the optimal variable. Even though $\tau^- \to a_1^- \nu_\tau$ has a lower branching ratio than other channels, its weight is about the same as the leptonic channels.

Channel	S	B.R.	W
$e^-\overline{\nu}_e\nu_\tau$	0.22	0.18	0.13
$\mu^-\overline{\nu}_\mu\nu_\tau$	0.22	0.18	0.13
$\pi^-\nu_\tau$	0.58	0.12	0.22
$\rho^-\nu_\tau$	0.49	0.25	0.39
$a_1^-\nu_\tau$	0.44	0.09	0.13

Table 3.1: Sensitivity, the branching ratio and the weight of each decay channel for the tau polarization measurement. The weights are normalized. Note that we didn't include event selection efficiency, i.e., the detector effect, in the calculation.

Chapter 4

The L3 Detector

CERN was established in 1950's for research in nuclear and elementary particle physics. LEP is one of the underground accelerators at CERN, located between Lake Geneva in Switzerland and the Mountains of Jura in France. It is the largest synchrotron machine in the world with a circumference of 37 Km. There are four experimental facilities around the LEP ring, ALEPH, DELPHI, L3, and OPAL [25] (see Figure 4.1).

At the L3 site there is one underground experimental cave and several side-buildings above the ground. The LEP ring runs through the cave, about 50 m below the ground level. The diameter and the length of the cave are 21.4 m and 26.5 m, respectively. One side of the cave is open up to the ground level to give access to the detector inside. The shaft between the cave and the ground level is 52 m high and 23 m in diameter. After the largest parts of the L3 detector were assembled in the cave, a four-story control building was built inside the shaft. During data acquisition, concrete beams are placed at the mouth of the cave to shield radiation coming from the LEP ring and protect the control building. Two block houses are build at the foot level of the cave to store radiation sensitive readout electronics and slow control electronics.

The L3 detector is designed to detect muons, electrons and photons with high momentum and energy resolutions, respectively [26,27]. Most parts of the detector are positioned inside the main solenoid [26], which has a length of 11.90 m and the inner radius of 5.93 m. To support inner subdetectors, a steel tube of 32 m length and 4.45 m in diameter is installed between the center and the inner wall of the solenoid. The detector is divided into two areas, the barrel region and the endcap region. In the barrel region, subdetectors are installed around the beam pipe in a

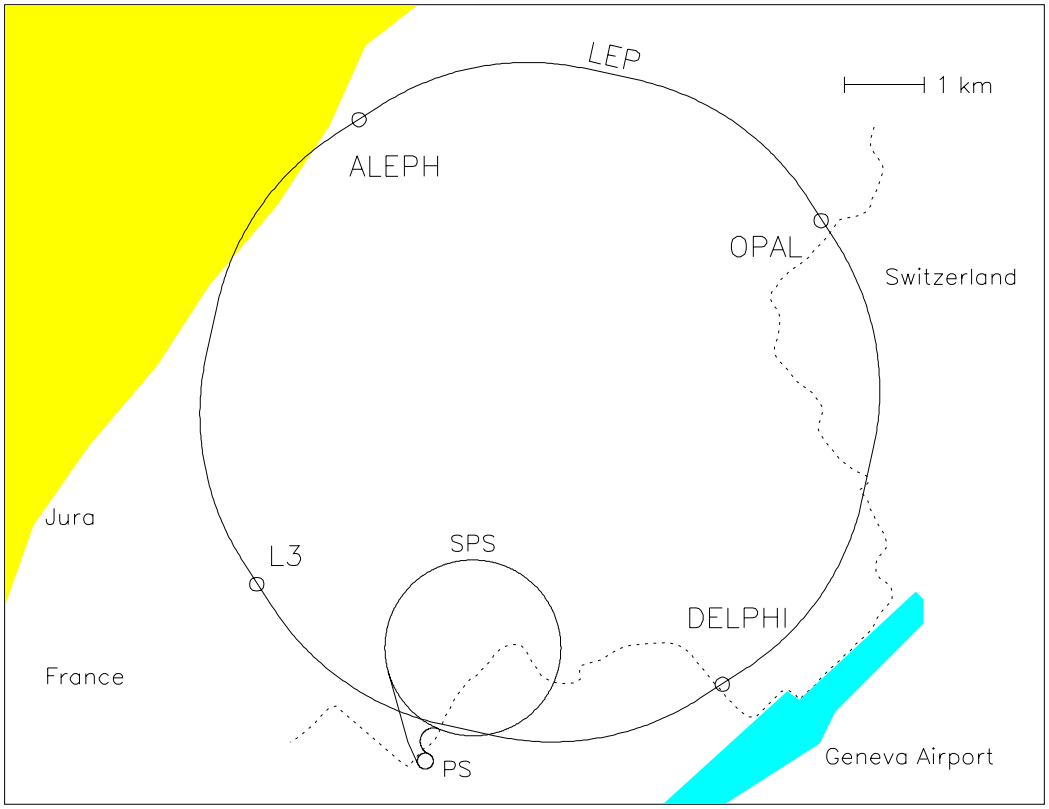

Figure 4.1: A perspective view of the LEP site

concentric order at the center of the detector. Their alignment is parallel to the solenoid field. In the endcap region, subdetectors face forward or backward with respect to the beam directions, in order to improve hermetricity of the detector.

Starting from the beam interaction point to the main solenoid in the radial direction, the barrel piece subdetectors are installed in the following order:

- The central tracking system measuring momentum of charged particles.
- The electromagnetic calorimeter measuring energy of electromagnetically interacting particles.
- The scintillator devices measuring interaction time of particles to reject cosmic events caught in the detector.
- The hadron calorimeter system measuring energy of strongly interacting particles.
- The muon spectrometer system to measure momentum of muon candidates.

The endcap subdetectors are positioned in a similar order. The endcap tracking system and the endcap calorimeters are housed within the main solenoid. The forward-backward muon chambers are mounted around magnet doors. Luminosity and radiation monitors are located farther from the main solenoid facing the incoming beams.

4.1 The Magnet

The main part of the L3 magnet [26] is a 7800 ton solenoid designed to give 0.5 T field at the central region. The relatively weak field strength is chosen to optimize muon momentum resolution. The octagonal shaped solenoid coil is wrapped in a support yoke made of iron. At each side of the pole, a pair of half-doors are installed to give access to inner subdetectors.

The solenoid coil is made of specially treated aluminum plates welded step by step. First, a group of plates are welded together to make a 6 turn package, which weighs 40 t. Then 28 such packages were bolted together with four cooling circuits, which result in a 168-turn coil. A thermal shield is placed on the inner wall of the coil to protect inner subdetectors. The nominal current of the coil is 30 kA.

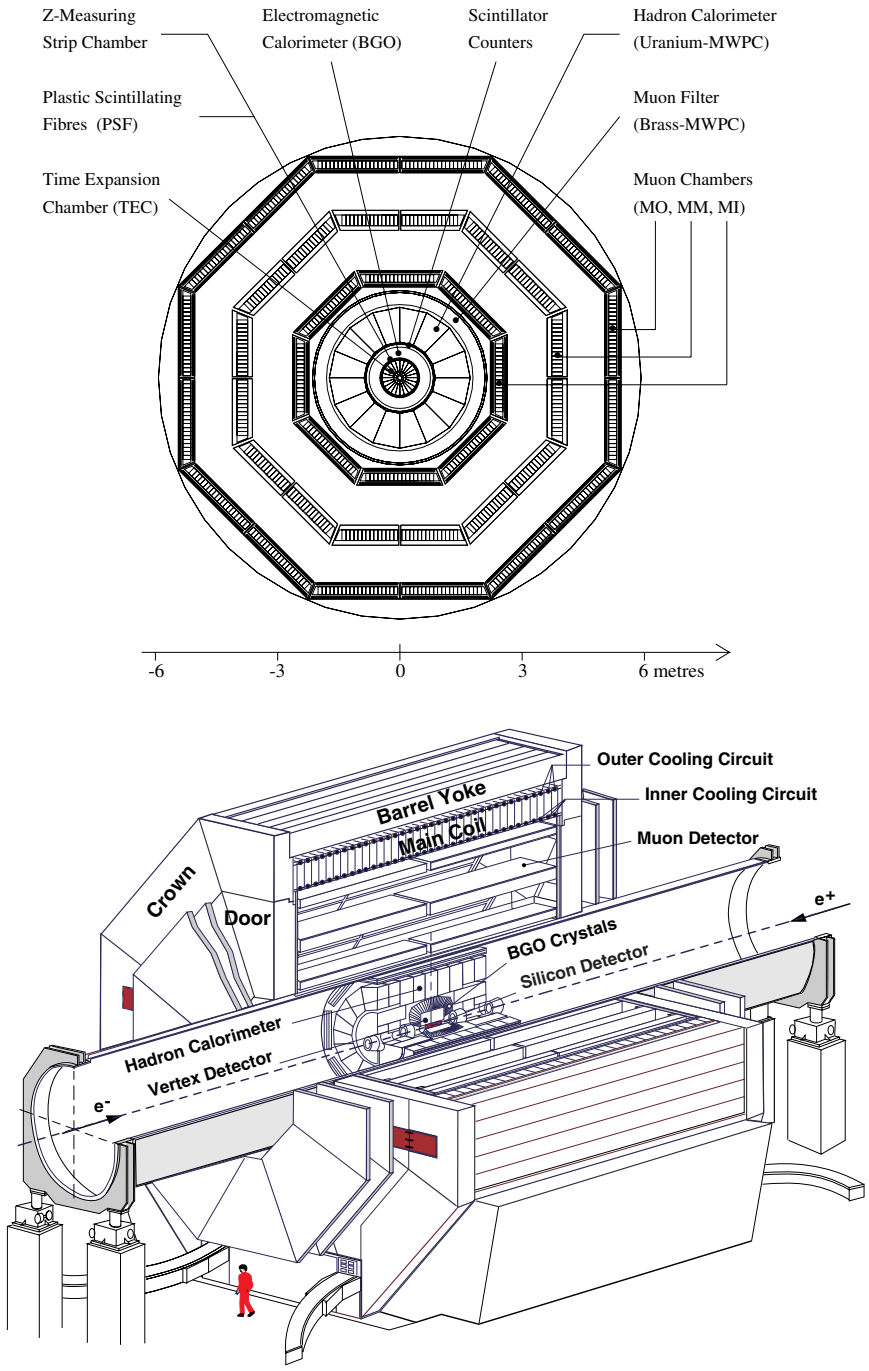

Figure 4.2: (a) A view of L3 in $r - \phi$ plane (b) An L3 perspective view

The magnet structure is made of soft iron with 0.5% carbon. The poles are self-supporting structures made of 1100 t steel. Each pole consists of a crown and a pair of half-doors. The poles are filled with 5600 t soft iron plates to return the magnetic flux.

Nuclear magnetic resonance (NMR) probes are installed to measure the absolute value of magnetic fields. In addition to this, Hall plates are installed inside the support tube and magnetoresistors are embedded in the muon chambers.

The support tube [26] is a 32 m long, 50 mm thick, 4.45 m diameter steel cylinder. The part of the tube positioned inside the magnet is made of non-magnetic stainless steel and the part outside the magnet is made of carbon steel. At each end of the tube, a flange support is built to transfer loads to the ground. Two torque tubes are mounted around the the support tube to position muon spectrometer modules.

4.2 The Central Tracking System

Direction and momentum of a charged particle is measured by the tracking system. The L3 tracking system provides good momentum resolution for low energy charged particles. For high energy charged particles, information from both the tracking system and calorimeters is used to assign particle energy. Since calorimeters and the muon spectrometer are positioned inside the solenoid, available volume for the central tracking system is relatively small. The tracking system consists of a Time Expansion Chamber (TEC) [28], a Z-detector (Z-chamber), Forward Tracking Chambers (FTC), Plastic Scintillator Fibers (PSF) and a Silicon Micro Vertex Detector (SMD) [26, 27, 30]. All of the subsystems are barrel pieces except the FTC. Detailed information on the central tracking system is described in Reference [29].

The principal element of the system is the TEC [26], which measures transverse momentum and direction of a charged track in the two dimensional $r - \phi$ space. The lever arm length of the TEC is 31.7 cm. Dimuon events and Bhabha events are used to calibrate the TEC. The transverse momentum resolution measured by the TEC, $\delta(P_t)/P_t$, is 0.018. [1]

During data acquisition, the TEC is filled with a 80% CO_2 and 20% iC_4H_{10} gas mixture at a pressure of 1.2 bar. The gas mixture gives a small diffusion coefficient,

[1] With SMD hits, the resolution improves to 0.012. Private communication with Ghita Rahal-Calot.

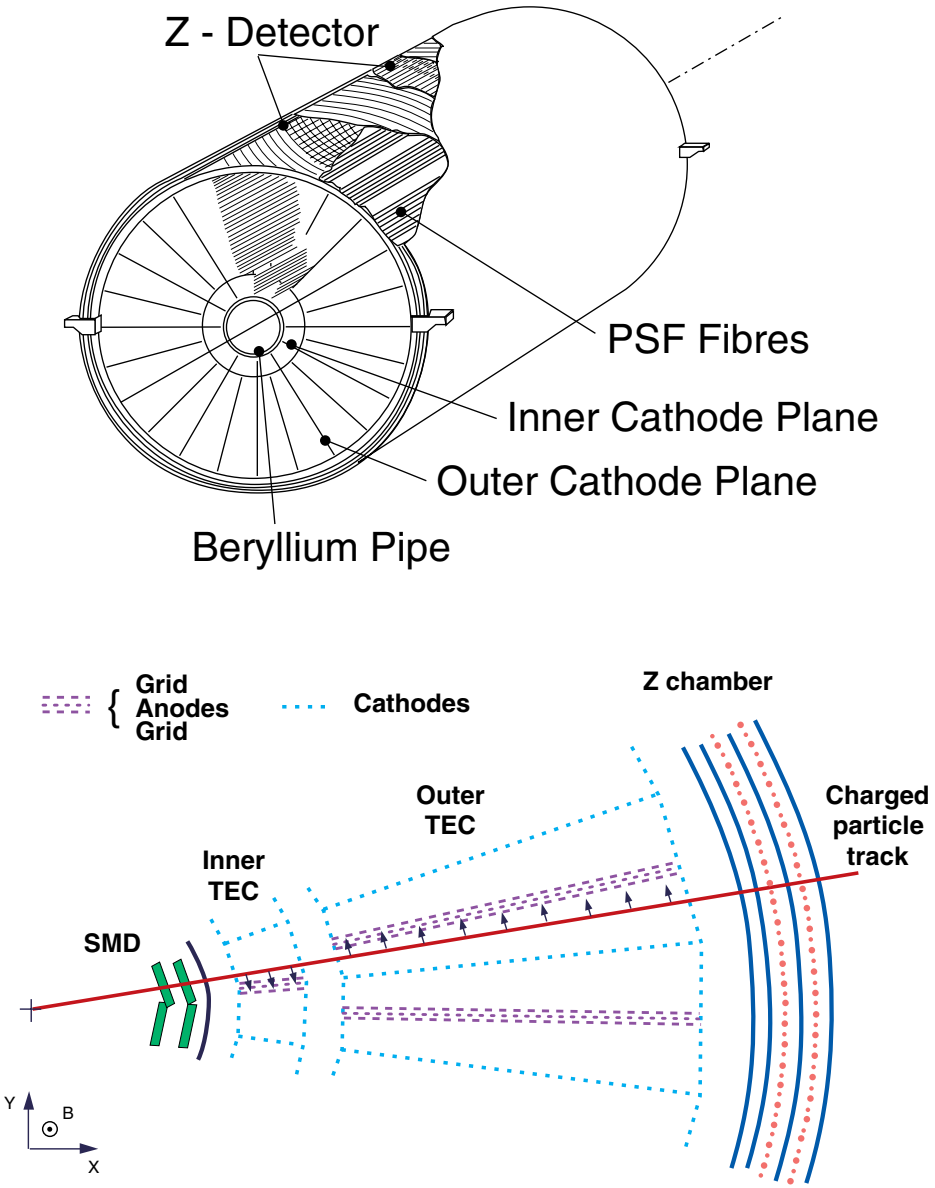

Figure 4.3: (a) A TEC perspective view (b) One sector of the TEC

a low drift velocity of 6 $\mu m/ns$, and a small Lorentz angle of 2.3 deg. To reach the desired resolution with the drift length limited up to 5 cm, drift time is measured by the center of gravity method. Flash Analog to Digital Converters (FADC) are used to sample the anode pulses. Ion tails are cancelled from the shape of the pulses [26].

The TEC anode and cathode wire planes are arranged alternatively in radial direction, dividing the detector volume into 12 sectors at the inner circle and 24 at the outer circle (see figure 4.3). Each inner and outer sector has 8 and 54 readout wires, respectively. Each inner sector is designed to face two corresponding outer sectors, in order to resolve direction ambiguity coming from mirror tracks generated by the symmetry of the outer sector shape.

The PSF is positioned between the TEC and the Z-chamber. On the outer face of each TEC segment, one PSF ribbon is placed. The PSF is used to verify the TEC calibration as an alternative method [27].

The Z-chamber is positioned outside the TEC volume [26]. It consists of two coaxial cylindrical proportional chambers with a cathode strip readout system. The proportional chambers are built on three support cylinders. Four copper strip layers encase the cylinders to produce cathodes. Two anode wire planes are placed between the cylinders. The inner chamber has the cathode strips inclined with respect to the beam direction (z direction) by 69 deg in one plane and by 90 deg in the other plane, and the outer chamber by $-$ 69 deg and by 90 deg, respectively. The Z-chamber is mainly used to get the direction and the impact parameter of a charged particle going into calorimeters in the z dimension. It can also give additional information in $r-\phi$ reconstruction of the charged track by the the slanted cathode planes. The effective length of a cathode strip is 1068 mm. During data acquisition, a gas mixture of 80% argon and 20% CO_2 is filled in the Z-chamber. periods. The resolution of the z coordinate measurement is 400 μm at the center of the detector.[2]

The FTC [27] measures the position and the direction of a charged particle leaving the central tracker via its endflanges. The FTC consists of two parts, each sandwiched between one TEC endflange and one BGO endcap front. The spatial resolution and the angular precision of the FTC are better than 200 μm and 10 mrad, respectively [27].

During the winter shutdown of '92-'93, the SMD [30] was installed between the beam pipe and the TEC, and it became fully operational in '94. It consists of two

[2]Private conversation with Elmar Lieb.

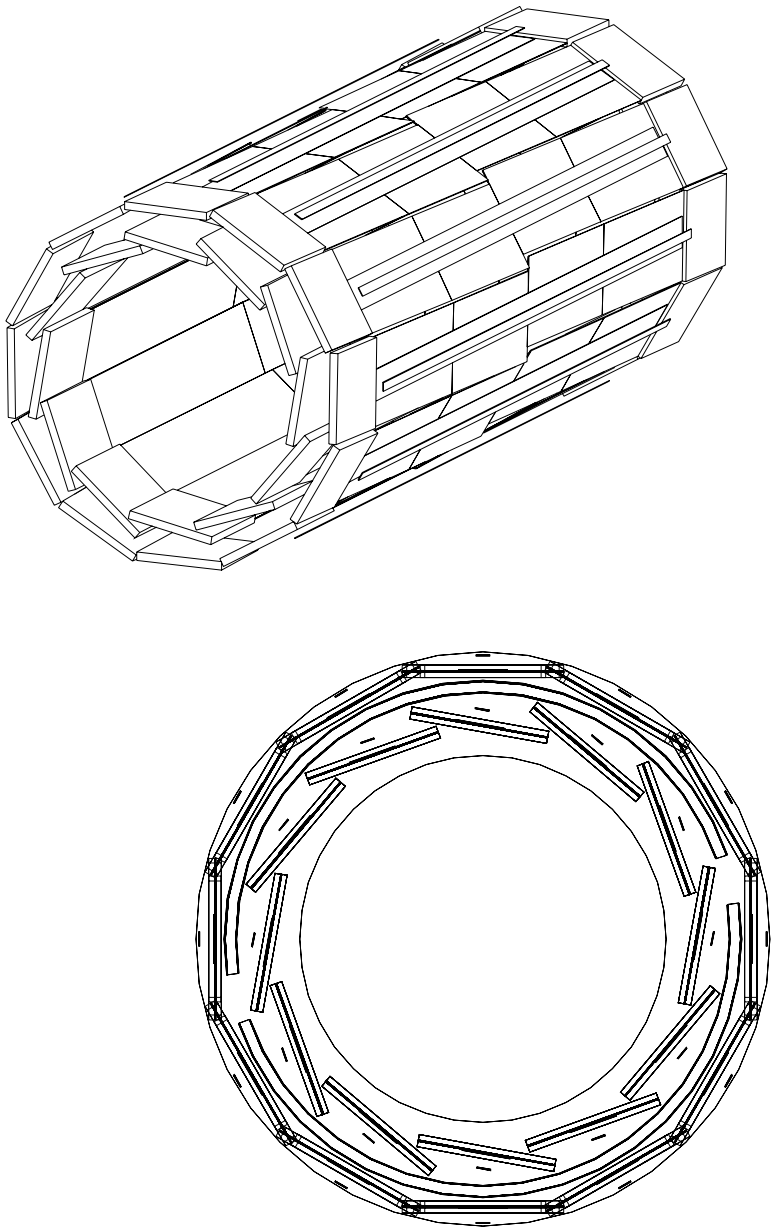

Figure 4.4: (a) A perspective view of the SMD (b) The face of the SMD in xy plane

cylindrical layers having 12 ladders respectively (see figure 4.4). Each ladder has four double-side silicon wafers and 24 SVX readout chips[3]. Each wafer has $r-\phi$ coordinate readout strips on the outer face and z coordinate readout strips on the inner face. The coordinate measurement resolution is 10 μm at the $r-\phi$ face and 25 μm at the z face.[4]

The additional 3-dimensional hits from the SMD increase the lever arm of the TEC by 4.8 cm. With the good position resolution of the hits, the augmented lever arm improves TEC calibration, enhances transverse momentum resolution of charged tracks, and supports secondary vertex reconstruction in multi-track events.

4.3 The Electromagnetic Calorimeter

The electromagnetic calorimeter is located outside the central tracking system and consists of one barrel piece and two endcap pieces [31]. It is designed to give good resolution over a wide range of energy from 100 MeV to 100 GeV. Bismuth germanate oxide(BGO) crystals are used as showering and detecting materials at the same time. The BGO crystal has a short radiation length for photons and electrons and has a large nuclear interaction length. It is sensitive to electromagnetic-interactive particles and has a good hadron/electron rejection ratio of 1000:1.

The BGO crystals are cut in pyramid shapes. The dimension of the front face is 2 cm$\times$2 cm, that of the tail face is up to 3 cm$\times$3 cm, and the length of the crystal is 24 cm. Two magnetic field insensitive photodiodes and optical fibers from xenon lamps are attached to the tail face of each crystal. The photodiodes are connected to preamplifiers and the preamplifiers to the readout system. Since the amount of light collected at the tail face is proportional with respect to the distance between the light source and the tail face, a reflective coating gives the crystals a flat light collection efficiency (see Figure 4.5).

The cylindrical barrel piece covers the range of $-0.72 < \cos\theta < 0.72$ [5] with 7680 crystals. The inner radius of the cylinder is 52 cm and the length is 100 cm. One slice of the calorimeter includes 24 crystals and 160 slices are put on each half-cylinder parallel to the beam direction. To protect crystals from cracking,

[3]The name SVX originates from "Silicon VerteX", i.e., the CDF microvertex detector at Fermi National Accelerator Laboratory.

[4]From '94 data, after the local alignment.

[5]θ is the polar angle with respect to the beam axis.

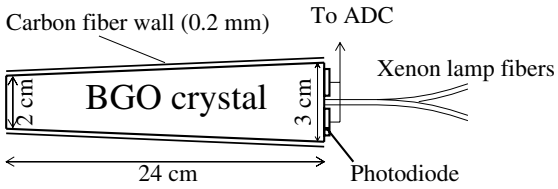

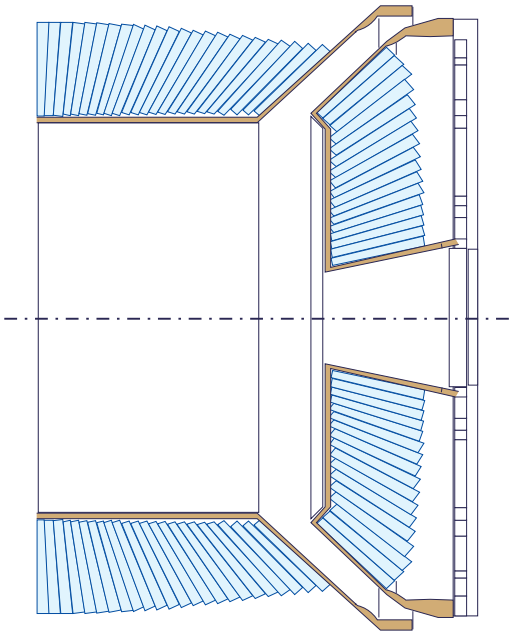

Figure 4.5: (a) A BGO crystal (b) Half of the barrel detector and one endcap detector

each crystal is separated from the neighbors by carbon fiber composite cell walls. All crystals are aimed to the beam interaction point with a small angular offset to suppress photon leakage.

The endcap pieces cover the range of $0.80 < |\cos\theta| < 0.98$ with 3054 crystals. They are installed outside The FTC and each piece is split into two halves. The crystal structure and the readout system are identical to those of the barrel piece (Figure 4.5).

BGO crystals are aging and it takes several days to recover full transparency from a strong radiation dose. Two methods are used to calibrate the crystals accurately. One uses Bhabha events and the other uses a xenon light monitoring system [32]. The energy resolution of the calorimeter is 5% at 100 MeV and better than 2% between 1 GeV and 100 GeV [27]. The dimension of each crystal is smaller than the Molière radius (2.3 cm in BGO), giving a broad shower profile spread over crystals. Hence, a good centroid position can be obtained and discrimination between hadrons and electrons is enhanced. The position resolution is about 4 mm at 1 GeV and 1 mm at 45 GeV [26].

4.4 The Scintillators

The scintillation counters [26] are located between the electromagnetic calorimeter and the hadron calorimeter. There are 30 plastic counters under the barrel hadron calorimeter ($|\cos\theta| < 0.83$), and an additional 16+16 counters were installed over the endcap hadron calorimeter in '95. At each end of a barrel counter and at the outer end of a endcap counter, a Hamamatsu photomultiplier tube is mounted, which gives high quantum efficiency and good time resolution [26].

The system is used to trigger hadronic events with scintillator hit multiplicity, and it is useful to reject cosmic muon events with time of flight information. A cosmic muon passing near the beam interaction point can be misidentified as a dimuon event coming from e^+e^- interactions, but it takes 6 ns for a cosmic to traverse opposite counters. Real dimuons hit the opposite counters almost at the same time. The time resolution of counters measured by dimuon events is 460 ps [27].

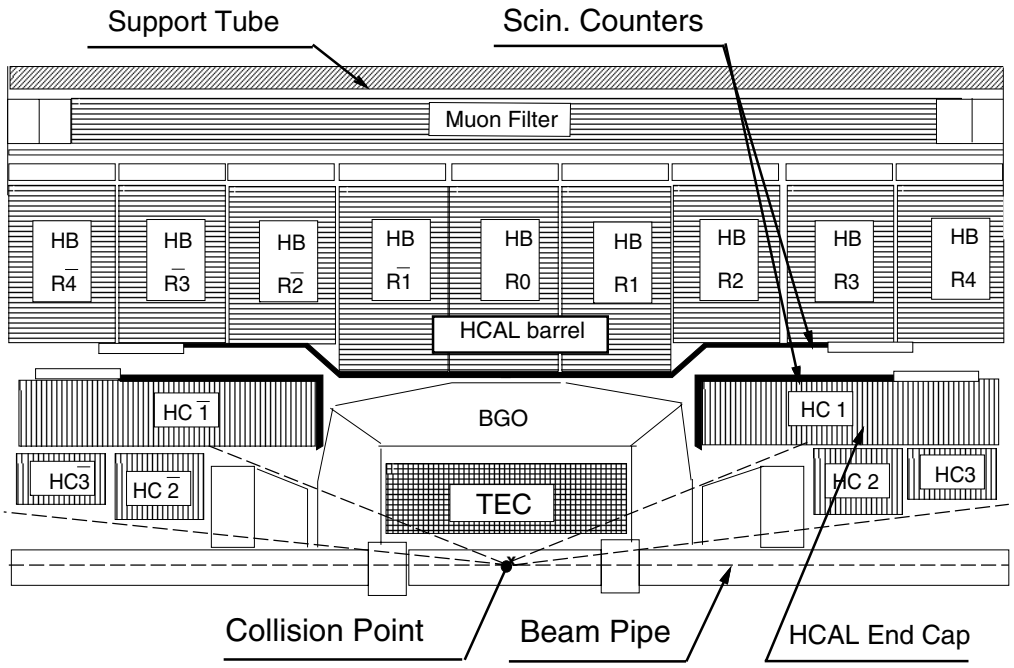

Figure 4.6: The hadron calorimeter, the muon filter and the scintillator counters

4.5 The Hadron Calorimeter and the Muon Filter

In L3, energy of hadronic particles is measured by a total absorption technique using both the electromagnetic calorimeter and the hadron calorimeter [33]. The calorimeters are acting as a filter and only non-showering particles survive the filter to make hits in the muon spectrometer. The uranium hadron calorimeter consists of the barrel part and the forward-backward part. The barrel part covers the range of $35\,\mathrm{deg} < \theta < 145\,\mathrm{deg}$, and the forward (backward) parts cover the range of $5.5\,\mathrm{deg} < \theta < 35\,\mathrm{deg}$ ($145\,\mathrm{deg} < \theta < 174\,\mathrm{deg}$). Uranium has a short absorption length. It is suitable to be used in the limited inside space of the L3 magnet and acts as a built-in γ ray source for calibration.

The barrel part is a modular structure consisting of 9 rings. Each ring has 19 modules. One module is an alternating structure of depleted-uranium plates and gas wire proportional chambers. The readout wires from the gas chambers are grouped in tower shapes, and each tower covers $\delta\phi$, $\delta\theta$ of 2 deg. Together with the support structure, the central 3 rings give 3.52 absorption lengths and the outer rings give 3.15 absorption length for pions.

Each endcap part consists of three separate rings, and each ring is split into two halves. They are removable to give access to inner L3 subdetectors. Particles that originate at the beam interaction point and pass through the endcap pieces experience 6 to 7 absorption length.

The muon filter [26] is located between the barrel hadron calorimeter and the support tube, giving an additional absorption length of 1.03. The filter consists of 8 octants made from brass absorption plates and gas proportional chambers. Together with the electromagnetic calorimeter, the scintillators, the barrel hadron calorimeter, the muon filter, and the support tube, the total absorption length for pions is 6.01 at the central barrel and 5.64 at the outer barrel [26] (see figure 4.6).

The position resolution of jets in the calorimeter systems is about 2.5 deg. The combined energy resolution of the TEC and the calorimeter systems for charged pions is better then 20% above 15 GeV [26].

4.6 The Muon Spectrometer

The L3 muon spectrometer [34] is designed to have the momentum resolution of better than 3% at 50 GeV in 0.5 T magnetic field in the barrel region [26]. The barrel spectrometer consists of two ferris wheels, each having 8 modular units or octants. Each octant consists of 5 momentum measuring chambers, two in the outer, two in the middle, and one in the inner layer. In addition to these, there are z coordinate measuring chambers attached on the top and bottom of the inner and outer chambers (see Figure 4.7).

Since a muon having momentum more than 3 GeV will be confined to only one octant, only alignment between chambers of the same octant is critical. But the large volume of the octants makes the alignment system complicated, which consists of optical and mechanical measurements, UV lasers and cosmic ray verification.

The momentum measuring chambers, or P-chambers are constructed with aluminum frames and aluminum side panels. There are 3000 wires in one chamber

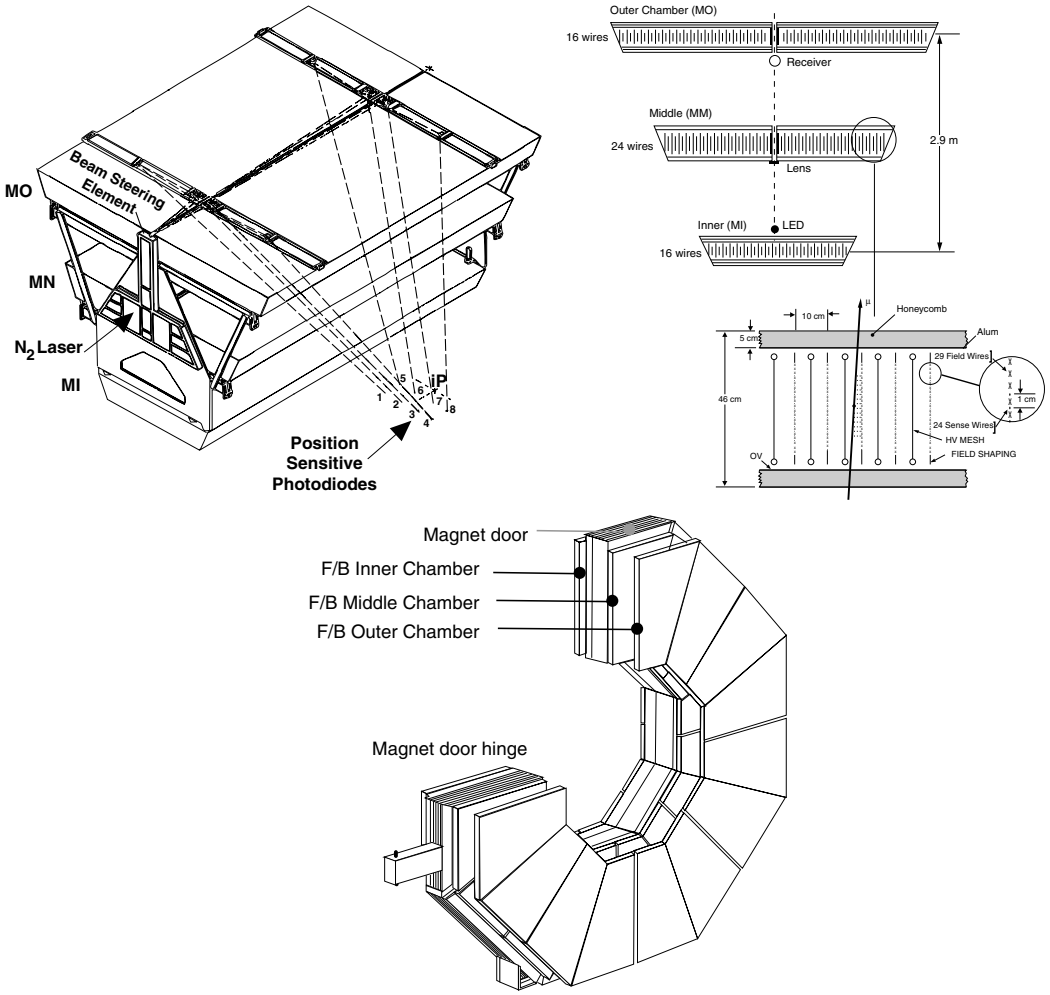

Figure 4.7: (a) An octant of the barrel muon spectrometer (b) A profile of P-chambers from an octant (c) The forward-backward muon detector

including 320 signal wires, and the wires are supported by Pyrex glass and carbon fiber bridges. The z coordinate measuring chambers, or Z-chambers consist of two layers of drift cells closed by aluminum sheets. The position resolution measured by a test beam is about 500 μm.

During '93-'94 and '94-'95 winter shutdowns, the forward-backward muon detector was installed, which increases the muon acceptance in the range of $24\,\mathrm{deg} < \theta < 44\,\mathrm{deg}$ [35]. 16 detector modules are mounted on each L3 magnet door. One module includes 3 layers of trapezoidal drift chambers. One of the layers is installed facing inner L3 subdetectors on the magnet door and other layers are installed on the opposite side of the door facing outwards (see Figure 4.7).

In the range of $36\,\mathrm{deg} < \theta < 44\,\mathrm{deg}$, momentum of muons is measured with 2 P chambers from the barrel spectrometer and the inner-most layer of the forward-backward detector. The expected momentum resolution is 4 to 23%, assuming the alignment accuracy of 120 μm for the forward-backward chamber [35].

In the range of $24\,\mathrm{deg} < \theta < 36\,\mathrm{deg}$, muons are measured with the forward-backward detector. Since the solenoid field alone cannot saturate the magnetic doors in the enough strength, additional toroids coils are turned around the magnetic doors. With 6300 A of currents, the toroids supply 1.2 T of magnetic field. The momentum resolution is limited to 34 % due to multiple scattering.

4.7 The Luminosity Monitor

To record the event rate, two sets of luminosity [27] monitors are installed in either side of the L3 detector (figure 4.8). Each set consists of a BGO calorimeter and a silicon tracker (SLUM). Each calorimeter has 304 BGO crystals covering the range of $24.9 < \cos\theta < 69.9 mrad$ and 2π over ϕ, and each SLUM consists of two θ (polar angle) measurement layers and one ϕ (azimuthal) angle measurement layer. At this small polar angle range, the e^+e^- process is dominated by t-channel scattering, which is an advantage to luminosity measurement since QED process in the channel is well understood. From the Bhabha events collected at the monitor, the absolute luminosity is measured with the experimental precision of 0.08% [26].

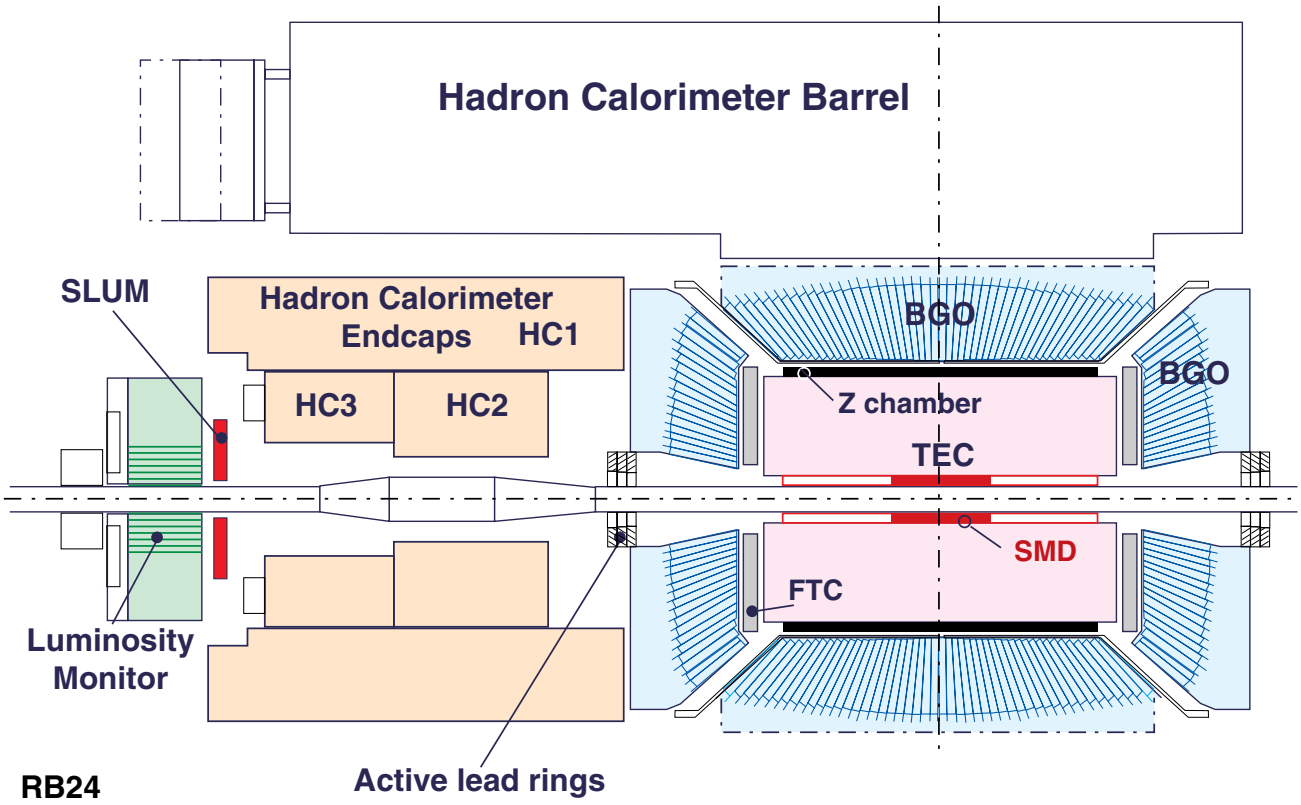

Figure 4.8: The BGO calorimeter and the SLUM as the luminosity monitor

4.8 The Trigger

The purpose of the L3 trigger system is to select events coming from e^+e^- interactions with high efficiency and to reject backgrounds coming from cosmic, beam gas, electronic noise, etc. The LEP beams cross each other per 11.1/22.2 μs depending on the beam mode, 4 $\times$ 4, and 8 $\times$ 8 bunches, respectively. The only dead time in the system occurs during the digitization and the readout period which takes at least 500 μs. During '94, the typical trigger rate was about 5 Hz. The contents of triggered events are as follows [37]:

- 1 Hz of physics events, mainly Z^0 decay.
- 2.5 Hz of Bhabha events for luminosity measurement.
- 1.5 Hz of background events.

The trigger system consists of three levels. In each level, several selection criteria are applied with OR logic [36].

The Level-1 Trigger There are five subtriggers in the first level, depending on the response of each subdetector; the TEC trigger, the muon trigger, the scintillator trigger, the energy trigger and the luminosity trigger. The Level-1 trigger uses a coarse data stream separated from the main data stream as its input.

The TEC trigger: The TEC trigger is used to select interesting physics events with charged tracks and also used as a backup for other subtriggers. It looks at analog wire signals from the outer TEC (14×24) and searches for tracks from hit patterns. Tracks should have transverse momentum of more than 150 MeV, and there should be at least two tracks with acollinearity of less than 60 deg. The typical trigger rate is 4 Hz, but it depends a lot on beam luminosity and beam conditions.

The muon trigger: The muon trigger selects events with at least one particle that penetrates muon chambers. It scans each muon cell wires and looks for a track pointing to the interaction point with transverse momentum of more than 1 GeV. At least 2 P-chamber hits and 1 Z-chamber hits in the muon spectrometer are required. The trigger rate goes down from 10 Hz to 1 Hz if at least one good scintillator hit is required.

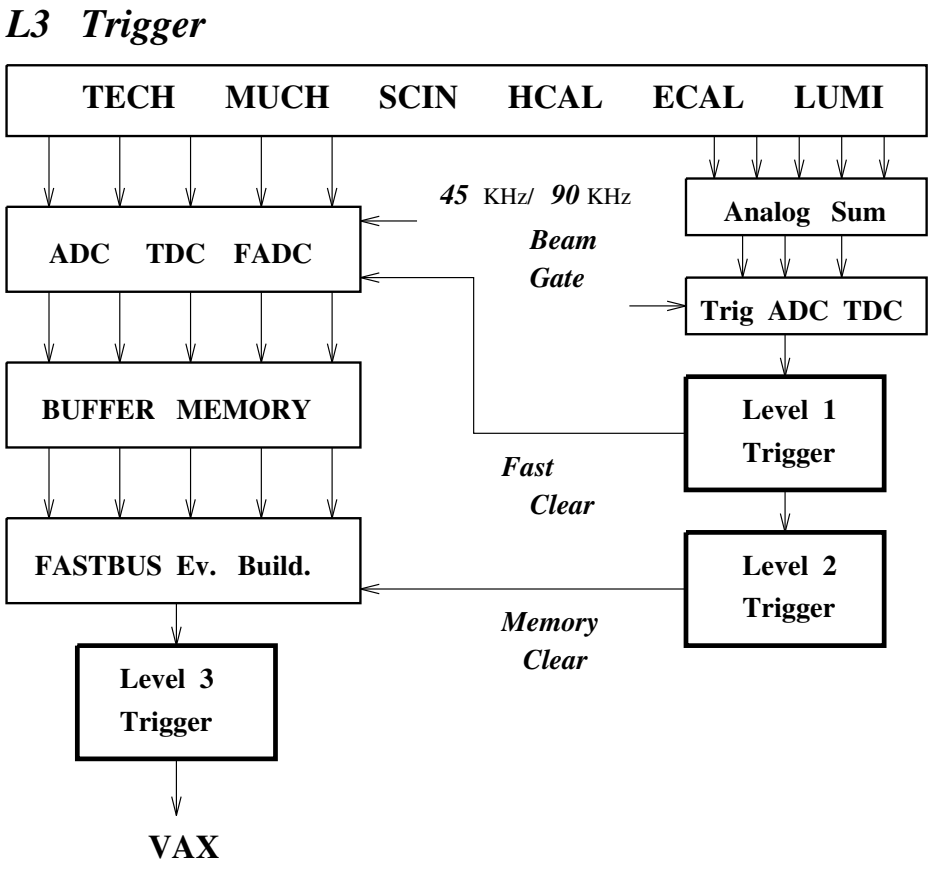

Figure 4.9: The L3 trigger structure

The scintillator trigger: The scintillator system selects high multiplicity events. if there are at least 5 scintillator counter hits spread over 90 deg. The information from the system is also used for the muon trigger. The typical scintillator trigger rate is 0.1 Hz.

The energy trigger: The energy trigger is based on information from the BGO calorimeter and the hadron calorimeter. Its purpose is to select e^+e^-, $\tau^+\tau^-$, hadronic and $\nu\nu\gamma$ final states. The BGO calorimeter is grouped into $32\phi \times 16\theta$ channels and the hadron calorimeter is divided into 16×11 channels for inside layers with less than one absorption length and into 16×13 channels for outside layers. An event is accepted if the total energy from the calorimeters is more than 20 GeV, if the total energy from the barrel BGO and the hadron layers is more than 15 GeV, if the total energy from the barrel and the endcap BGO is more than 20 GeV, or if the total energy from the barrel BGO is more than 10 GeV. Besides, the system checks energy of clusters formed at the same ϕ and θ cell in two calorimeters. If one of the matching clusters has energy more than 7 GeV, the event is accepted. If there is a corresponding TEC track, the threshold is lowered to 3 GeV. The typical energy trigger rate is 2.5 Hz.

The luminosity trigger: The analog sum from two luminosity monitors is the input to the trigger system. A luminosity event is selected if both monitors have more than 15 GeV of energy or if one has more than 25 GeV and the other has more than 5 GeV. The typical trigger rate is 2.5 Hz and it is visible that the rate depends on the beam luminosity.

The Level-2 Trigger The purpose of the second level trigger system is to reject backgrounds events selected by level-1. It uses the coarse data used in level-1 and the level-1 result itself. Since level-2 spends more time to analyze data and it correlates individual level-1 results, it is effective to filter energy triggers from electrical noises and TEC triggers generated by beam-gas, beam-wall interaction, and synchrotron radiation. If the level-2 result is positive, the event is passed to the next step. Otherwise, the memory used for the event is cleared. If an event is selected by more than one level-1 subtriggers, it is passed to the next step directly.

The Level-3 Trigger If the level-2 result is positive, the complete digitized data is passed on to the level-3 to recheck the event with more precisely defined criteria.

Energy from the calorimeters is recalculated and the electrical noises are rejected further. Muon triggers are filtered with more stringent scintillator coincidence time. And TEC tracks are required to have corresponding energy of more than 100 MeV in the calorimeters and are required to have a common vertex per event.

4.9 The Offline Computer Facilities

In L3, data is processed via two steps, the online production and the offline production. The online production is done at the L3 control building located over the L3 detector. In the control building, event information from subdetectors filtered by the trigger system is stored on tapes to be sent to the offline production team. Status of the detector and calibration parameters are stored in the online database, which is copied to the offline database periodically. In the offline production, information from each subdetector is analyzed and basic reconstruction of each event is performed. The result is written down on tapes or stored on disks to be used by L3 physicists.

The structure of the L3 offline computer facilities is explained in the following categories [37]:

- Interfaces for users, consisting of workstations and terminals.
- A mainframe and its emulators for data handling and major computing power.
- CERN-Site Networks.

There has been a major upgrading of the facilities starting from '94, to compensate the vast amount of Z^0 data made by the good performance of LEP I machine and to prepare for the LEP II physics [37].

Interfaces for users: During 1980s, individual physicists used Apollo workstations for analysis. Since Apollo workstations were aged and faded out in the market, interface computers are upgraded to Hewlett-Packard (HP) and Silicon Graphics (SGI) workstations early 1990s.

The mainframe: To manage the vast amount of data efficiently and to provide enough computing power to users, L3 keeps the mainframe connected with the individual interface workstations by the network. Users get access to the data either from disks mounted on the mainframe (in case of the Challenge machine) or from tapes via the mounting facility connected to the mainframe, and they submit batch jobs to the mainframe. Before the upgrade, an IBM 3090 machine was used as the mainframe and additional Apollo DN10000 machines were provided for batch jobs. During the upgrade, the IBM machine was exchanged with a SGI Challenge XL with the capacity of up to 36 processors [37]. A 160 Gbyte disk system was installed late '94.

The network: The size of one L3 data set on disks or tapes can be as large as 200 Mbytes, while the data transfer speed of Ethernet is about 1 Mbytes/s and that of Fiber Distributed Data Interconnect (FDDI) is about 10 Mbytes/s. Hence, it is vital to prevent traffic jams between the mainframe and workstations and among the workstations. During the Apollo machine days, this task was handled by Apollo Token Ring (ATR), Ethernet, Stollmann, and FDDI systems. During the upgrade, the network structure was simplified to Ethernet and FDDI, and the second Ethernet line was installed for the sake of dedicated L3 physics analysis [37].

Chapter 5

Data Analysis

Since the L3 detector is a complicated system, it is difficult for one person to handle the entire data structure alone. Hence, the basic data structure is provided by coordinated work of the entire L3 group people and the detailed analysis is performed by small groups of relevant people or by individuals. In short, each stage of the τ polarization measurement is explained in the following article.

1. The L3 group reconstructs events and stores event information in common formats. Data events collected by the L3 online system are stored in DAQ, DRE, DSU and DVN formats, where the latter has more reconstructed information and the former has more raw data information. MC events are produced by generators [38], are processed by GEANT 3.14 [39] to get the ideal detector response, then are reconstructed and stored in the DSU and DVN formats. The real detector simulation is given as a reconstruction option, where we can kill dead clusters in the subdetectors according to the online information recorded in the L3 database and we can smear kinematic observables to match the corresponding MC resolutions with the data resolutions.

2. The τ group aligns subdetectors with respect to the TEC system, using Bhabha event tracks stored in the DSUs. This alignment method [40] covers the TEC endflange area, which is not included in the nominal L3 alignment.

3. A second reconstruction [40] is done on events stored in the DSUs to produce ntuples, a data storage set, for both data and MC events. The main purpose of the second reconstruction is a better separation between charged and

neutral particles in the BGO calorimeter. The τ group alignment constants obtained in the previous stage are applied during the second reconstruction. To enhance transverse momentum resolution, the fill vertex constraint is applied in the second TEC track reconstruction.

4. We identify decay particles from τ events. If it is necessary, further adjustment of energy scales and more smearing of kinematic observables are done.

5. Fitting in the individual τ decay channel is performed and the measurement of τ polarization asymmetry is finalized.

In this chapter, detector alignment and event selection procedures will be summarized. The procedure of energy assignment for each identified particle and the measurement of τ polarization asymmetry will be handled in separate chapters. (Note: If possible, event selection is performed in both the barrel and endcap regions of the L3 detector. But the final fit is done only in the barrel region.)

5.1 Detector Alignment

The polar angle of a charged track passing through the barrel region of the central tracking system is obtained from hit information of the Z-chamber. In case of a charged track passing through the endcap region, one way to obtain the polar angle is using information from FTC hits. Another way to obtain the polar angle in the endcap area is to measure the angle between the average beam collision point and the last hit position of the charged track near the TEC endflanges. Or we can use both sources of information by merging two numbers into one with corresponding weights.

The τ group coordinate system and the L3 group coordinate system are the same in the $r-\phi$ plane, where the TEC $r-\phi$ plane is used as the reference. The difference between the τ group and the L3 group coordinate systems comes from the z coordinate. The τ group aligns subdetectors with respect to the TEC endflanges and the origin of the z coordinate is positioned at the center of the TEC. The L3 group aligns them with respect to the Z-chamber and the origin of the z coordinate is positioned at the center of the Z-chamber.

The τ group alignment [40] is done in the following way.

1. The z coordinate of the average beam collision point is measured, using charged tracks passing though the endcap region.

2. The BGO calorimeter is aligned with respect to the TEC, both in the $r-\phi$ plane and the z coordinate.

3. The Z-chamber is aligned with respect to the BGO calorimeter.

We used a sample of '94 Bhabha event tracks to obtain the alignment constants.

5.1.1 The Fill Vertex

The collision point of incident electron and positron beams is controlled by the LEP machine group using optics located in front of the L3 detector at each detector side. The average collision point during each fill of beams is calculated by the TEC offline group and stored in the database as the fill vertex. The usual spread of beam collision points during a fill is in the order of $150\mu m$, $25\mu m$ and $2cm$ in the direction of x, y and z coordinates, respectively.

During '94, the movement of the fill vertex in the x and z coordinates was small, and the movement in the y coordinate was also small, except a jump after a technical shutdown period[1]. Considering the spread of the collision points, x and y coordinates of each fill vertex and z coordinate of the entire year average are used as the reference point during detector alignment.

We used the radiative Bhabha event tracks going into the endcap area to measure the z coordinate of the year average collision point. The polar angle of each track is reconstructed from position information of the last hit of the track in the TEC endflange area only.

5.1.2 Alignment of the BGO Calorimeter

Alignment of the BGO calorimeter is performed separately for each piece of the subdetector, which consists of 2 pieces in the barrel and 4 pieces in the endcap region. We don't expect a big change in their positions, unless they reposition the endcap pieces during the technical shutdown periods. The BGO calorimeter is assumed to have an ideal geometry of a cylinder and its axis is assumed to be parallel with respect to the main TEC axis. The small polar angle difference between the BGO axis and the TEC axis is regarded as secondary and ignored. First, alignment in the $r-\phi$ coordinates is performed with two translational constants and one rotational constant for each piece. The aim is to match coordinate

[1] Private conversation with Vuko Brigljevic

measurements done by the BGO calorimeter to measurements by the TEC system. We used Bhabha event tracks to compare two measurements. Each Bhabha event generates two opposite TEC tracks with a corresponding shower in the BGO calorimeter for each track. We adjusted the alignment constants until the impact point extrapolated from each TEC track matches the shower center in the BGO calorimeter. Second, the translational constant in the z coordinate is measured for each BGO detector piece. We adjusted the constant until the z coordinate of the average beam collision point measured by the shower centers in the BGO calorimeter becomes the same as the reference value explained in Subsection 5.1.1.

5.1.3 Alignment of The Z-Chamber

The Z-chamber has 4 readout layers. Alignment is done for each layer with respect to the BGO calorimeter. Each layer is divided into 10 areas and each area is given two alignment constants, one with respect to the polar angle and the other with respect to the azimuthal angle. We adjusted the constants until the extrapolations from the Z-chamber hit positions match the shower centers in the BGO calorimeter. Considering the spatial resolution of the Z-chamber and the BGO calorimeter, this method is satisfactory for the polarization measurement using 1-prong τ decay with particle energy as the fit variable. In case of the measurements using either 3-prong τ decay or using acollinearity of $\tau^+\tau^-$, we need a more rigorous alignment method, possibly including SMD information.

5.2 Event Selection

Selection of $e^+e^- \rightarrow \tau^+\tau^-$ events is processed in three stages. First, low multiplicity, back-to-back events are preselected to obtain a pure sample of dileptons from Z^0 decay. Second, classification of τ decay modes is performed. The detector area is divided into two hemispheres by a plane perpendicular to the thrust axis of the event. Each hemisphere is treated independently in the selection. The decay mode classification in each hemisphere is based upon topological properties of energy depositions in the BGO and hadron calorimeters. Of a charged particle, a matching track in the central tracking system is required. In each tau decay mode, the background from other decay modes is suppressed at this stage. Finally, the non-tau background is rejected and the size of the remaining non-tau background is estimated to be used in the polarization fit later. Since we use particle energy

as the fit variable, we have to identify particles independent of their particle energy. Our identification technique is relatively independent of energy of τ-decay products, so the bias on tau polarization is minimal.

5.2.1 Preselection

The primary aim of preselection is to reject hadronic decay of Z^0 particles. The following criteria are applied to get low multiplicity events:

- The number of good TEC tracks in one hemisphere is less than or equal to 3, while that of the opposite hemisphere is less than or equal to 5. The total number of good TEC tracks should be less than or equal to 6.
- The number of BGO bumps should be less than or equal to 25.

Most of hadronic events are rejected by the requirement. Hence, after each τ decay mode is identified, the background contribution from hadronic Z^0 decay becomes negligible.

A part of cosmic backgrounds is rejected by comparing activities between the upper muon spectrometer and the lower muon spectrometer. If a track has the DCA (Distance to Closest Approach) farther than 15cm from the beam collision point, the track is excluded from the selection. This limit is chosen to give just enough cosmic events to be used in the polarization fit.

Two photon interaction background is filtered by looking at information on the acollinearity and the transverse energy imbalance. The cuts imposed on them are carefully adjusted to provide a background sample for later study. The following cut limits are applied:

- The minimum acollinearity between all the calorimeter objects in the entire detector area should be more than 2.0 rad, or
- The transverse energy imbalance between them should be more than 3 GeV.

The final preselection efficiency over 4π obtained by a τ Monte Carlo sample study is 93.03%.

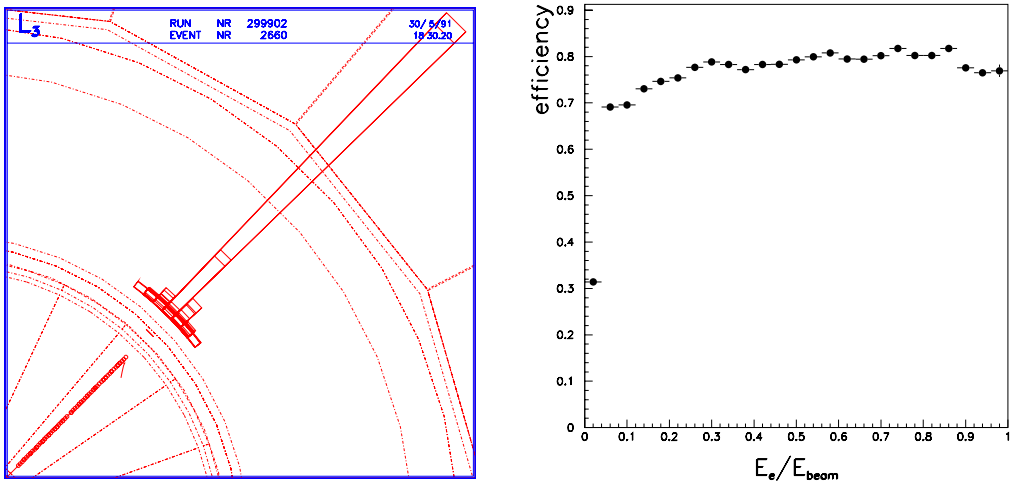

Figure 5.1: (a) An electron candidate (b) The selection efficiency of $\tau^- \rightarrow e^- \overline{\nu_e} \nu_\tau$

5.2.2 Electron Identification

An electron is expected to have a single shower bump in the BGO calorimeter with a matching TEC track (Figure 5.1 (a)). The shower profile of an electron in the BGO calorimeter is sharp and symmetric. We define χ^2_{EM} as compatibility of the observed shower profile in 3 $\times$ 3 BGO crystals around the shower maximum with the reference profile. An electron candidate is required to have χ^2_{EM} less than 30 for 8 degrees of freedom. The reference profile is defined by the average shower shape obtained from Bhabha events. Also the shower of the candidate should consist of at least 3 BGO crystals. It is found in the test beam that the shower shape is relatively independent of particle energy over 1 GeV [41].

A photon has the same shower profile as an electron in the BGO calorimeter. To avoid the situation where a hadronic τ decay with a photon is mistaken as an electron, the angle between the BGO shower center of an electron candidate and the extrapolation of the corresponding TEC track is required to be within 5σ of the detector resolution. The probability that energy deposited in the BGO calorimeter and momentum measured by the TEC system originate from a single particle is required to be more than 0.00005.

The energy deposition in the hadron calorimeter should be less than 3 GeV

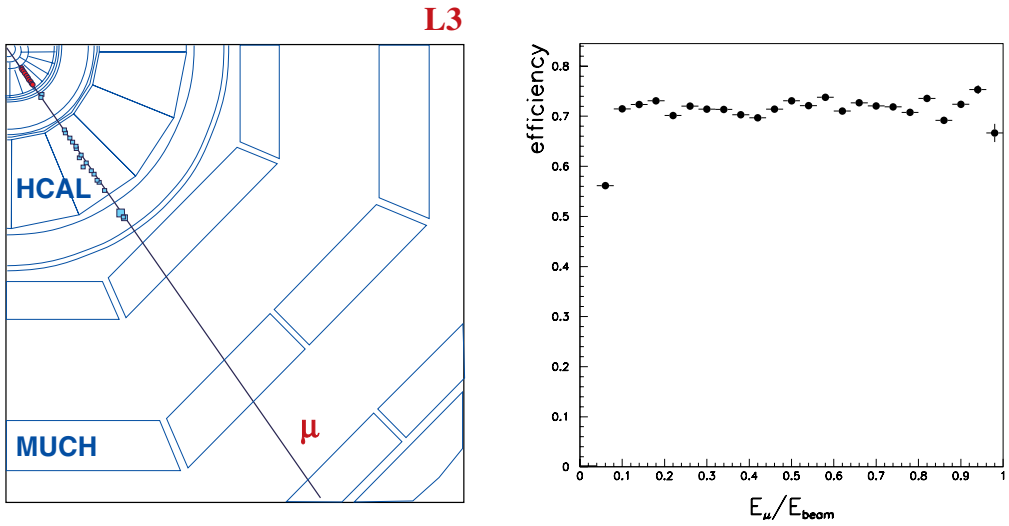

Figure 5.2: (a) A muon candidate (b) The selection efficiency of $\tau^- \rightarrow \mu^- \overline{\nu_\mu} \nu_\tau$

and it should look like a tail of an electromagnetic interaction coming out of the BGO calorimeter.

5.2.3 Selection of $\tau^- \rightarrow e^- \overline{\nu}_e \nu_\tau$

The major background in this decay mode is Bhabha events, so selection is limited in the barrel region of the detector ($|\cos \theta_{thrust}| < 0.7$). To cut down Bhabha events further, the total energy in the BGO calorimeter is required to be less than 80% of the total incident beam energy. To reduce the remaining two photon interaction background after the preselection, it is required that either the difference in the transverse energy between the two hemispheres be more than 2 GeV or the total transverse momentum of the two hemispheres be more than 10 GeV or the total energy of the BGO calorimeter be more than 15% of the total incident beam energy.

The selection efficiency for $\tau^- \rightarrow e^- \overline{\nu}_e \nu_\tau$ is relatively independent of particle energy and is 75% in the fiducial volume (Figure 5.1 (b)). The backgrounds are 1.5% from other τ decay modes, 1.8% from Bhabha events and 2.0% from the two photon interactions.

5.2.4 Muon Identification

A muon is a minimum ionizing particle in the L3 detector. Based on this fact, a requirement is made on topology of the energy deposition in the calorimeters to select muons (Figure 5.2 (a)).

- The energy deposition of the track in the BGO calorimeter < 1 GeV.
- The number of hadron calorimeter cells with nonzero energy deposition should be at least 50% of all cells along the track.

In addition to them, at least two hits in the P-chambers and one hit in the Z-chambers are required in the muon spectrometer. The extrapolation of the reconstructed track from the muon spectrometer hits to the beam interaction point should be within 5σ of the spatial resolution of the spectrometer at the interaction point. These additional requirements are redundant as selection rules, but necessary to get the momentum of the candidate with good resolution.

5.2.5 Selection of $\tau^- \rightarrow \mu^- \overline{\nu}_\mu \nu_\tau$

Selection of this mode is done in the barrel muon spectrometer only. The forward-backward muon chamber was not fully active in '94, so the area with $|\cos\theta_{track}| > 0.82$ is excluded from the selection. The major background in the $\tau^- \rightarrow \mu^- \overline{\nu}_\mu \nu_\tau$ mode is dimuon events. The following rejection rules are applied to curtail them.

- The opposite hemisphere has an identified muon with the energy more than 40 GeV.
- The opposite hemisphere has an identified muon and the total energy of two muons is more than 60 GeV.
- The opposite hemisphere has an identified muon by calorimeter information, but whose energy cannot be measured correctly.

The background from two photon interactions is reduced by requiring that the transverse energy imbalance between two hemispheres be more than 1 GeV. The following requirements are to reduce the cosmic background. The DCA reconstructed from TEC information should be less than 1.5 cm and the hit in the scintillators should be within the time window of 10 sec. The selection efficiency is 70% in the fiducial volume (Figure 5.2 (b)). The background estimation is

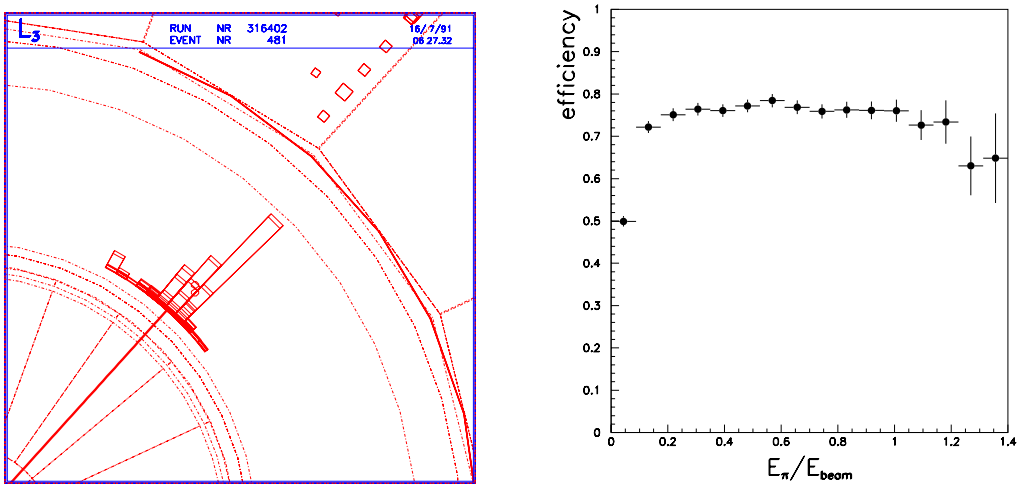

Figure 5.3: (a) A hadron candidate (b) The selection efficiency of $\tau^- \rightarrow \pi^-\nu_\tau$

1.0% from other τ decay modes, 7.1% from dimuon events, 0.4% from two photon interactions and 0.1% from cosmics.

5.2.6 Selection of $\tau^- \rightarrow \pi^-\nu_\tau$

Identification of $\tau^- \rightarrow \pi^-\nu_\tau$ needs different guidelines from other hadronic τ decay modes, where the number of neutral clusters in the BGO calorimeter gives the signature of the decay mode. Selection starts with a candidate having a single track in the TEC system, with hits in both the BGO and the hadron calorimeters (Figure 5.3 (a)). The shower profile of a charged pion in the BGO calorimeter is wide and asymmetric. A candidate with a sharp shower profile in the BGO calorimeter is identified as an electron and rejected. A charged pion leaves a visible energy deposition in the hadron calorimeter. A candidate which behaves as a minimum ionizing particle through the BGO and the hadron calorimeters is rejected as a muon. There should be no neutral clusters near the candidate and the shower center in the BGO calorimeter should match the extrapolation of the track reconstructed from TEC hits. The probability that calorimeter energy assigned to the particle and momentum measured by the TEC originate from a single particle should be more than 0.003 in the barrel and more than 0.01 in the endcap region.

The requirement to suppress non-τ backgrounds is as follows:

1. The energy assigned to the opposite hemisphere particle as an electron < 40 GeV. The total BGO calorimeter energy should be less than 68 (62)% of the total incident beam energy in the barrel (endcap) region.

2. The identified muon in the opposite hemisphere should have particle energy less than 40 GeV.

3. The angle between the candidate and the opposite hemisphere particle should be more than 2.8 (2.9) rad. Either the candidate or the opposite hemisphere should have energy more than that of a typical two photon interaction event.

The selection efficiency of $\tau^- \to \pi^-\nu_\tau$ is 72% in the barrel (Figure 5.3 (b)). The background in the barrel is 11.4% from other τ decay modes, 0.8% from Bhabha events, 1.7% from two photon interactions, 0.3% from dimuon events, and 0.6% from cosmics.

5.2.7 Neutral Pion (Photon) Identification in Hadronic τ Decay

Most cases of hadronic τ decay have accompanying neutral pions. In case of a high energy π^0 coming from τ, the two photons decayed from the π^0 particle are boosted together and form a single neutral cluster in the BGO calorimeter. A neutral cluster in the BGO has a sharp symmetric shower profile like that of an electron. To assign energy accurately to particles from τ decay, it is necessary to separate the clusters in the BGO calorimeter into charged pion clusters and neutral clusters in the correct way.

1. The impact point of a charged pion in the BGO calorimeter is predicted from the extrapolation of the corresponding TEC track (Figure 5.4 (a)).

2. The expected shower profile of the charged pion is subtracted from the entire shower bumps (Figure 5.4 (b)).

3. In the remaining shower bumps, local maxima are assumed to be neutral particles and the expected neutral shower profiles are subtracted from the shower (Figure 5.4 (c)).

4. Procedure 2 and 3 are iterated until the stable shower profiles are obtained for each particle (Figure 5.4 (d)).

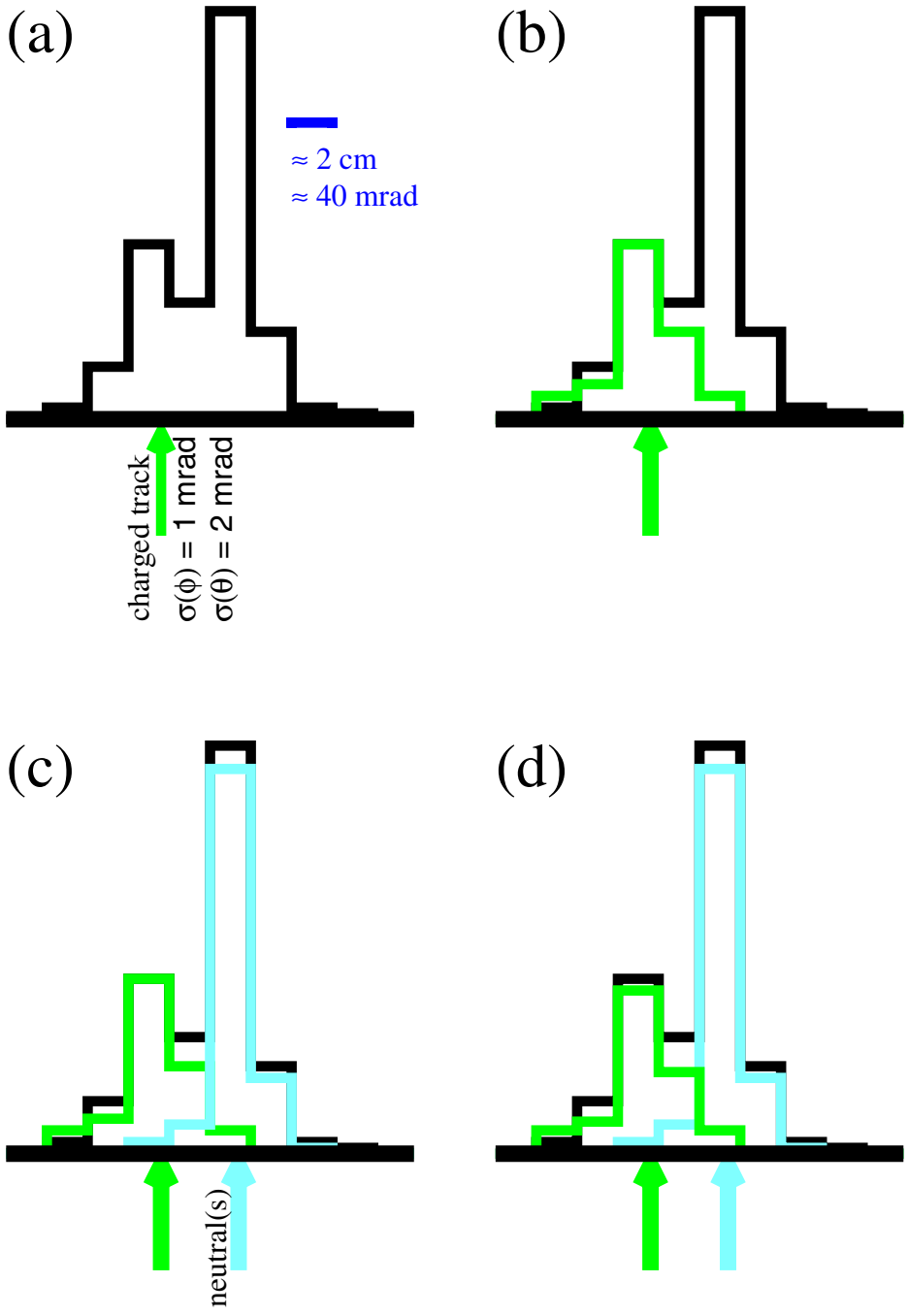

Figure 5.4: The algorithm used to separate the charged cluster and the neutral cluster in the BGO calorimeter

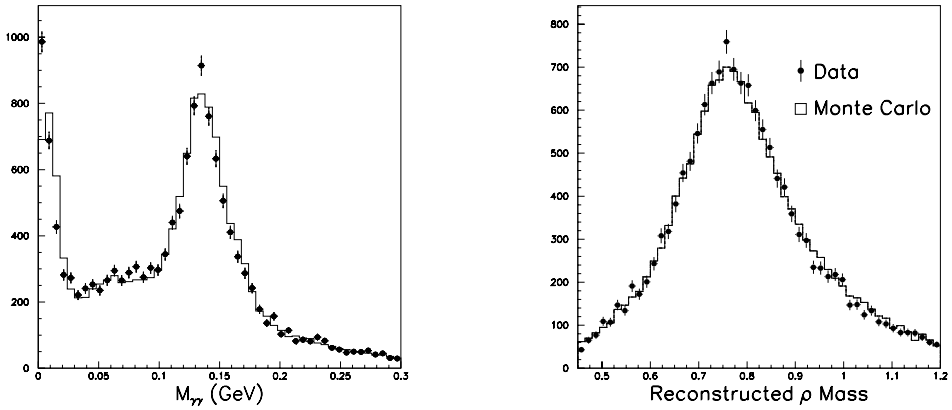

Figure 5.5: (a) The reconstructed mass of π^0 in ρ^- candidates. (b) The reconstructed mass of ρ^- candidates.

5.2.8 Selection of $\tau^- \rightarrow \rho^- \nu_\tau$

A $\tau^- \rightarrow \rho^- \nu_\tau$ decay candidate consists of a charged pion and a neutral pion. Since this channel has the largest branching ratio among τ decay modes, the selection effort is concentrated at the reconstruction of the correct number of neutral pions. There are three cases where only one neutral pion can be found properly.

- When only 1 neutral BGO calorimeter cluster is found near the charged pion candidate: Particle energy of the neutral cluster should be more than 1 GeV. Either χ^2_{EM} is less than 50 over 8 degrees of freedom or the invariant mass obtained by fitting the neutral cluster with two electromagnetic shower profiles should be between 0.1 and 0.2 GeV[2]. The neutral cluster should be located in the active region of the BGO calorimeter.

- When 2 neutral BGO calorimeter clusters are found near the charged pion candidate: The energy of each neutral cluster should be more than 0.5 GeV. The invariant mass of the two neutral clusters should be within 30 MeV $\sim$ 60 MeV of 0.14 GeV, depending on the total energy of the neutral clusters.

[2]The numbers given here are limited for very high energy neutral clusters. The actual selection numbers depend on particle energy of the neutral cluster.

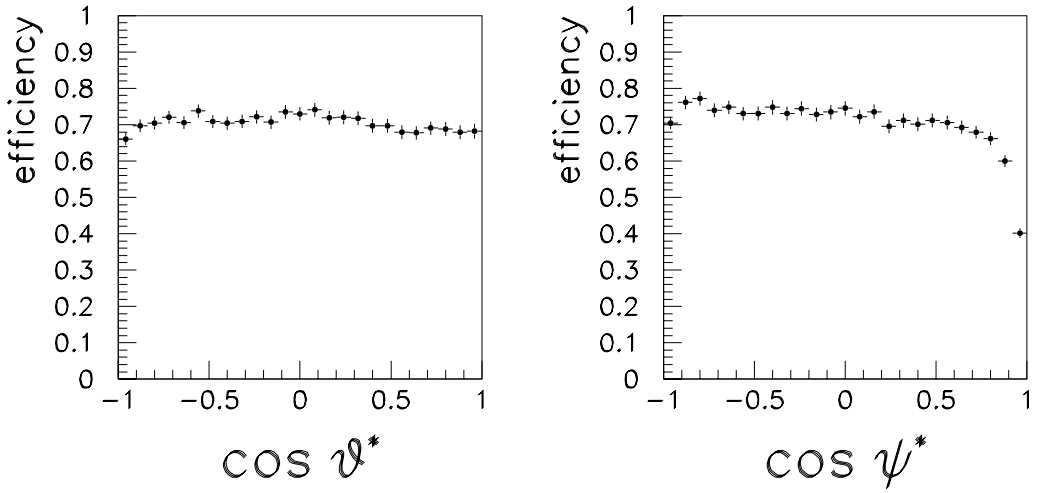

Figure 5.6: The selection efficiency of $\tau^- \to \rho^-\nu_\tau$ in terms of $\cos\theta^*$ and $\cos\psi^*$, the kinematic variables used in the polarization fit. Their meaning is explained in Section 3.3.

- When no neutral cluster is reconstructed in the BGO calorimeter: It does not happen often, but it can be a ρ candidate. There should be a high energy BGO calorimeter cluster, which is unusual in $\tau^- \to \pi^-\nu_\tau$. When the cluster is assumed to be an electromagnetic bump, its particle energy should be more than 15 GeV. χ^2_{EM} should be less than 50 over 8 degrees of freedom and the invariant mass obtained by fitting the neutral cluster with two electromagnetic shower profiles should be between 0.1 and 0.2 GeV[3].

The reconstructed ρ mass should be between 0.45 (0.5) GeV and 1.2 GeV in the barrel (endcap) region. Figure 5.5 shows the reconstructed masses of π^0s in ρ^- candidates and ρ^-s.

The requirements for the charged pion and the non-τ background rejection are not as strict as those of the $\tau^- \to \pi^-\nu_\tau$ case. The following requirements are applied in the barrel (endcap) region.

[3]The numbers also depend on the bump energy.

- The probability that total calorimeter energy assigned to the charged pion and momentum measured by the TEC system originate from a single particle should be more than 0.001 (0.01).
- The DCA of the TEC track for the charged pion < 2 cm. (In the endcap there should be more than 11 outer TEC hits.)
- The energy of the opposite hemisphere particle as an electron < 43 (40) GeV. The total BGO calorimeter energy < 90 (75) % of the total incident beam energy. (The total BGO bump energy inside the 30 degree cone of the TEC track should be less than 42 GeV in the endcap.)
- The identified muon energy at the opposite hemisphere < 43 GeV. (In the endcap, the efficiency of muon identification is not so good. The muon rejection cut is not applied in the endcap region.)
- The angle between the candidate and the opposite hemisphere track should be more than 2.5 (2.8) rad.

The selection efficiency is 70 (51)%. Figure 5.6 shows the efficiency in the barrel region. The background is 10.2 (14.3)% from other τ decay modes, mainly from $\tau^- \to \mathrm{a}_1^- \nu_\tau$ decay, 0.2 (1.5)% from Bhabha events and 0.5 (1.5) % from dimuon events.

5.2.9 Selection of $\tau^- \to \mathrm{a}_1^- \nu_\tau$

a_1 can decay either in a 1-prong mode or a 3-prong mode. The 3-prong mode will be handled in a separate article in Chapter 8. Selection of the 1-prong mode will be explained. As in the case of $\tau^- \to \rho^- \nu_\tau$, the main point of the reconstruction is to find two π^0s coming from 1-prong a_1 decay. To enhance purity of the final a_1 sample, selection is done in two stages. The preselection and the neural network selection.

In the preselection stage, leptonic τ decay is rejected as well as non-τ background. The neutral pions are searched in the following order:

1. A good π^0 reconstructed from two neutral BGO clusters. The reconstructed mass should be within $30 \sim 70$ MeV of the π^0 mass, depending on the reconstructed energy of π^0.

2. Assume that each remaining neutral BGO cluster is a π^0, until the total number of reconstructed π^0 reaches 2.

3. Still there are neutral BGO clusters remaining, combine each of them with the nearest neutral BGO cluster.

There should be two π^0 found as the result. Other preselection requirements are following. There should be a single track in the candidate hemisphere with at least 30 hits in the TEC, as a charged pion candidate. Each ρ mass reconstructed from each π^0 candidate and the charged pion candidate should be between 0.15 and 1.5 GeV. Shower centers of the charged pion and the neutral pion candidates in the BGO calorimeter should be in the active region of the detector. Total calorimeter energy from both hemisphere should be more than 14 GeV, to suppress two photon interactions. The angle between the candidate and the opposite hemisphere particle should be more than 2.4 rad. Bhabha events are rejected by asking less than 80 GeV of the total BGO energy and less than 40 GeV of the BGO energy in the opposite hemisphere. To suppress dimuon events, the identified muon energy of the opposite hemisphere is required to be less than 42 GeV. After all the preselection cuts, the candidate sample becomes consisting of $\tau^- \to \rho^- \nu_\tau$, $\tau^- \to \mathrm{a}_1^- \nu_\tau$ and $\tau \to n\,\pi^0\,\pi^- \nu_\tau$ $(n > 2)$ with roughly the same ratio.

After the preselection, a neural network [42] with 10 input nodes and 1 hidden node [43] is used to cut out $\tau^- \to \rho^- \nu_\tau$ background from the candidate sample. The final purity is 72% with the selection efficiency of 34% in the barrel region[4]. After the neural network is applied, non-τ background becomes negligible.

[4]The purity and the selection efficiency are subject to the neural network selection. About 10% of change is expected in the numbers depending on tuning of the neural network.

Chapter 6

Energy Scale and Resolution

Since we measure the τ polarization by fitting with the energy spectrum, the accuracy of the energy scale becomes the major source of the systematic errors. In this chapter, the methods to determine the energy for each particle, the energy scale and the resolution of energy are summarized.

6.1 Energy Determination of Electrons and Neutral Particles

Electrons and π^0s leave a sharp prominent shower in the BGO calorimeter. Their energy is measured from the shape of the showers [40, 44]. The energy scale at 45 GeV is checked by the Bhabha events, with the beam energy as the reference. The accuracy is estimated as 0.1%. The energy scale at 1 GeV is checked by the peak position of the π^0 mass spectrum (Figure 5.5 (a)) and the accuracy is estimated as 1%.

The energy resolution curve for electrons and photons with respect to the energy is shown in Figure 6.1.

6.2 Momentum Determination of Muons

The momentum of muons is measured by the hit information in the muon spectrometer, with correction of the energy lost in the calorimeters. If a muon track hits 3 P-chambers (called a triplet) in the muon spectrometer, the momentum

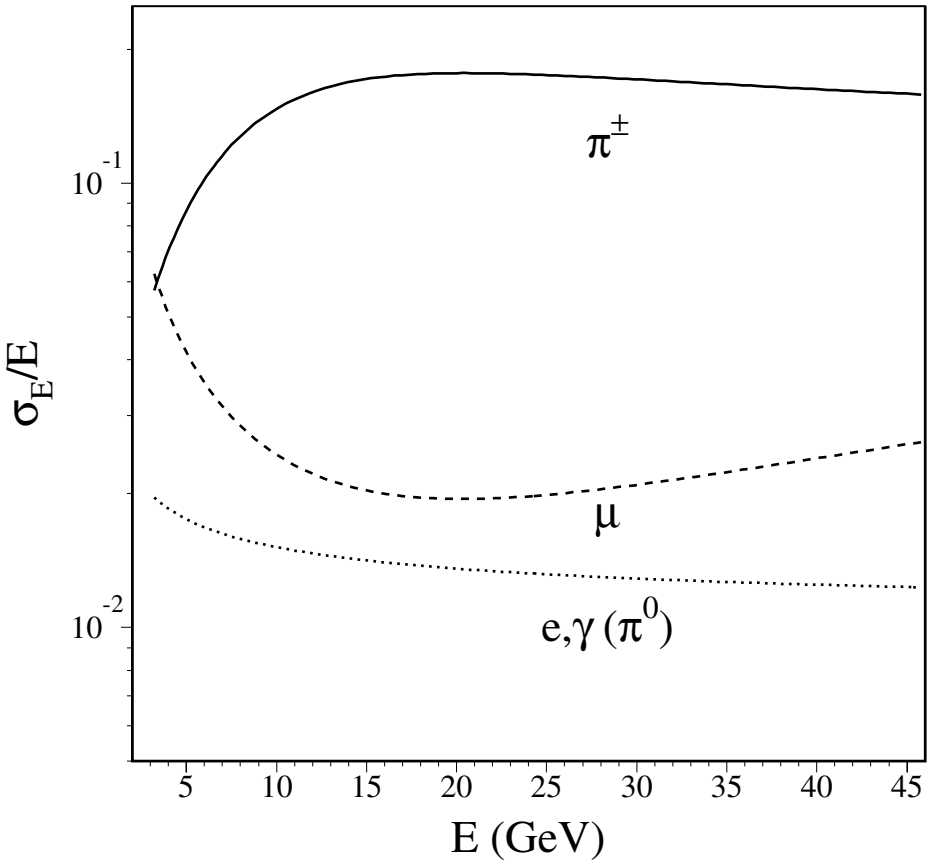

Figure 6.1: The energy resolution of the L3 detector for various particles.

is measured by the track sagitta. If it hits 2 P-chambers (called a doublet), the momentum is calculated from the difference of the track slopes in the 2 chambers. The momentum resolution at 45 GeV is determined from the dimuon events, 2.5% for triplets and 20% for doublets. The resolution at the lower energy is estimated by MC study and shown in Figure 6.1.

The accuracy of the momentum at 45 GeV is obtained from the dimuon events and is estimated to be 0.2%. The momentum scale at the lower energy is studied by comparing the momentum measured by the muon spectrometer to the momentum measured by the TEC, using $\tau^- \rightarrow \mu^- \overline{\nu}_\mu \nu_\tau$ events. Since lower energy muons lose more energy in the calorimeters, the accuracy worsens.

6.3 Energy Determination of Charged Pions

The information on the energy of a charged pion is obtained from two sources, the momentum measured by the central tracking system and the energy deposited in the calorimeters. If the particle energy is below 15 GeV, the central tracking system has better resolution, while over 15 GeV, the calorimeters give better resolution[1]. Hence, we measure the energy of a charged pion by maximizing the probability of two measurements coming from the same energy ϵ:

$$\begin{aligned} P &= P(E_C; \epsilon, \sigma_C(\epsilon)) \cdot P(1/P_T; \epsilon, \sigma(1/P_T) \\ &= \frac{1}{\sqrt{2\pi}\,\sigma_C^2(\epsilon)} \exp(-\frac{(E_C - \epsilon)^2}{2\,\sigma_C^2(\epsilon)}) \frac{1}{\sqrt{2\pi}\,\sigma_{1/P_T}^2} \exp(-\frac{(1/P_T - 1/\epsilon\,\sin\theta)^2}{2\,\sigma_{1/P_T}^2}) \end{aligned} \tag{6.1}$$

The TEC transverse momentum resolution σ_{1/P_T} and the calorimeter resolution $\sigma_C(\epsilon)$ will be explained in the next articles.

6.3.1 TEC Momentum Resolution

In the first order of approximation, resolution of the inverse of the TEC transverse momentum, σ_{1/P_T}, does not depend on the transverse momentum itself. Dimuon events are used in measuring σ_{1/P_T}, by comparing $1/P_T$ measured by the TEC to the expected transverse momentum, $1/(E_{beam} \cdot \sin\theta \cdot sign)$, where $\sin\theta$ and $sign$ of the track are given by the muon spectrometer measurement. To avoid additional charge confusion, only the track with 3 P-chamber hits in the muon spectrometer

[1] If SMD hits are included in the TEC track reconstruction, the border is at 22 GeV.

is used. Figure B.1 in Appendix B shows σ_{1/P_T} as a function of local TEC phi coordinates. The resolution at 45 GeV is estimated as $\sigma_{1/P_T} = 0.018\ GeV^{-1}$. The tracks going into the endcap area has worse resolution than the barrel tracks, since less hits are produced in the TEC. The $\cos\theta$ dependency of the resolution in the endcap is checked by the Bhabha samples, by counting the charge confusion ratio. If SMD hits are included in the TEC track reconstruction, we obtain much better momentum resolution. The detailed analysis is summarized in Appendix B.

The TEC momentum scale at 45 GeV is checked by looking at the distribution of $1/P_T^{TEC} - 1/P_T^{MUCH}$ in dimuon events [45]. The shift in the scale is estimated as 1.3%. At lower energy, the scale is checked using muons from $\tau^- \rightarrow \mu^-\overline{\nu}_\mu\nu_\tau$ and electrons from $\tau^- \rightarrow e^-\overline{\nu}_e\nu_\tau$ [45].

6.3.2 The Calorimeter Gains

The primary calibration for the BGO and the hadron calorimeter gain for the charged pions are obtained from a test beam data, since we don't have an independent sample of pions from Z^0 decay to calibrate. The test beam setup consisted of the BGO crystals, the hadron calorimeter modules, and the same trigger condition used in the online. It is found that a charged pion can act in the calorimeters in two ways. In the first case, the charged pion behaves as the minimum ionizing particle in the BGO calorimeter. In the second case, the charged pion interacts, makes a visible shower, and loses some of its energy in the BGO calorimeter. Nearly 40% of the charged pion events fall in the first category [46]. Hence, the gain curve is formulated in two equations [46]:

$$\epsilon = g_H(\theta,\phi)g_H(\epsilon)H + g_B(\epsilon)B \quad if\ B < 1\ GeV \tag{6.2}$$

$$\epsilon = g_H(\theta,\phi)g'_H(\epsilon)H + g_B(\epsilon)B \quad if\ B > 1\ GeV. \tag{6.3}$$

The first equation is for the first case and the second equation is for the second case. ϵ is the energy of the incident charged pion, H and B are the observed energy in the hadron and the BGO calorimeter, respectively. $g_H(\theta,\phi)$ is the part of the gain depending on the geometry of the detector. We obtained $g_H(\theta,\phi)$ from the MC study. $g_H(\epsilon)$, $g'_H(\epsilon)$, $g_B(\epsilon)$ are the energy dependent gains determined by the test beam study. The overall energy resolution of the charged pions in the calorimeter found by the test beam is

$$\frac{\sigma_C(\epsilon)}{\epsilon} \sim \frac{55\%}{\sqrt{\epsilon}} + 8\% \tag{6.4}$$

Year by year we recheck the energy dependent gains, since changing detector environments requires additional correction in the gains. It is done by looking at the peak position of the reconstructed mass spectrum of the $\rho^{\pm}$ candidates. The accuracy of the energy scale obtained from $\rho^{\pm}$ mass spectrum study is about 1.5%.

Chapter 7

The Measurement of τ Polarization

We will describe the fit procedure to get the τ polarization asymmetry in this chapter. In Section 7.1, the fit method used for the individual τ decay mode is explained. The method of the charge assignment is explained in Section 7.2. The result of the fit for each τ decay channel will be described in Section 7.3. And the final fit to get A_τ and A_e will be explained in Section 7.4.

7.1 The Fitting Method

The first step of the fit is to get the τ polarization asymmetry in each decay mode of τ. The detector volume is divided into 7 bins in the barrel with respect to $\cos\theta_{thrust}$ ($|\cos\theta_{thrust}| < 0.72$)[1]. The bin size is adjusted to distribute even numbers of events over 7 bins. The lower and upper limits of each bin are shown in Table 7.4. Fitting and error estimations are done in each bin.

In each $\cos\theta_{thrust}$ bin, the data distribution is fitted with the linear combination of the helicity positive MC distribution, the helicity negative MC distribution and the non-τ background distribution. Since the τ background distribution also depends on the polarization, it is included in the helicity positive(/negative) MC distribution. The purpose of the fit is to determine the combination which maximizes the likelihood function. For example, in a 1-dimensional fit, the combination

[1]In this analysis, only the barrel region events are used in the fit. In fact, it is possible to include the endcap area events in the analysis, i.e., $|\cos\theta_{thrust}| < 0.92$ with 9 fit bins.

can be described as

$$\begin{aligned} \frac{1}{N_d}\frac{dN_d}{dx} &= \frac{1}{N_{mc}}\left(\frac{1+\mathcal{P}_\tau^f}{1+\mathcal{P}_\tau^g}\frac{dN_+}{dx} + \frac{1-\mathcal{P}_\tau^f}{1-\mathcal{P}_\tau^g}\frac{dN_-}{dx}\right) \\ &+ \textit{non}\text{–}\tau\ \textit{backgrounds}, \qquad (x \in [0.,1.]) \\ N_{mc} &= N_+ + N_- \end{aligned} \tag{7.1}$$

where $\frac{1}{N_d}\frac{dN_d}{dx}$ is the data distribution, $\frac{1}{N_{mc}}\frac{dN_+}{dx}$ and $\frac{1}{N_{mc}}\frac{dN_-}{dx}$ are the helicity positive and negative MC distribution, respectively. $\mathcal{P}_\tau^f$ is the fitted polarization number while $\mathcal{P}_\tau^g$ is the polarization number used to generate MC events.

Likelihood Function The number of MC events we used for this analysis is 8 times the number of data events we collected in '94. Since we don't have infinite number of MC events, a binned[2] maximum likelihood function is used to accommodate the fluctuations in both data and MC distributions [47].

The Poisson probability to observe n_d^i events in the i-th bin of the data distribution is

$$P(n_d^i|\mu_d^i) = e^{-\mu_d^i}\frac{(\mu_d^i)^{n_d^i}}{n_d^i!}. \tag{7.2}$$

The underlying mean μ_d^i is yet unknown. We assume that it is described in the manner of Equation 7.2.

$$\mu_d^i = \frac{\mu_+^i}{r_+} + \frac{\mu_-^i}{r_-} + \frac{\mu_b^i}{r_b}, \tag{7.3}$$

where μ_+^i, μ_-^i and μ_b are the underlying means of the helicity positive MC events, the helicity negative MC events and the non-τ background events, respectively. r_+, r_- and r_b are the corresponding normalization factors. The probability to get μ_d^i from the observed combination of events n_+, n_- and n_b is

$$P(\mu_d^i)d\mu_d^i = e^{-\mu_+^i}\frac{(\mu_+^i)^{n_+^i}}{n_+^i!}e^{-\mu_-^i}\frac{(\mu_-^i)^{n_-^i}}{n_-^i!}e^{-\mu_b^i}\frac{(\mu_b^i)^{n_b^i}}{n_b^i!}d\mu_+^i d\mu_-^i d\mu_b^i. \tag{7.4}$$

Hence, the probability to observe n_d^i from the combination of n_+^i, n_-^i and n_b^i will be given by the following integration over the unknown underlying means:

$$P(n_d^i|n_+^i,n_-^i,n_b^i) = \iiint P(n_d^i|\mu_d^i)\cdot P(\mu_d^i|n_+^i,n_-^i,n_b^i)d\mu_+^i d\mu_-^i d\mu_b^i. \tag{7.5}$$

[2] **binned** with respect to the 1-dimensional fit variable, x.

The likelihood function is given by the products of Equation 7.5 over all the bins of the data distribution.

$$\mathcal{L} = -\sum_i \ln P(n_d^i | n_+^i, n_-^i, n_b^i) \tag{7.6}$$

We minimize this likelihood function to obtain the τ polarization and the overall normalization of MC events. The **MINUIT** software package was used for the actual minimization [48]. The detailed calculation of the likelihood function is done in reference [47].

The Fit Error The fit error is estimated by varying the likelihood function by 0.5, which corresponds to the 1 σ variation of a χ^2 fit. The statistical errors from the data and the finite MC events are calculated from the fit error, using the following relation,

$$\sigma_{fit}^2 = \sigma_{data}^2 + \sigma_{MC}^2 \simeq \sigma_{data}^2 (1 + \frac{1}{r}), \tag{7.7}$$

where r is the overall normalization of the MC events obtained from the fit.

7.2 Charge Assignment

The helicity of τ^+ is opposite to that of τ^- in $Z^0 \to \tau^+\tau^-$ interactions. Hence,

$$\mathcal{P}_{\tau^-}(\cos\theta) = -\mathcal{P}_{\tau^+}(\cos\theta) = \mathcal{P}_\tau(\cos\theta) \tag{7.8}$$

where $\cos\theta$ is defined by the thrust axis. We need the charge identification of the selected τ candidates and the events coming from τ^+ decay should be assigned to the opposite $\cos\theta$ bins. If at least one hemisphere is identified as having a μ decayed from a τ, its charge can be defined from its curvature in the muon spectrometer unambiguously. Otherwise, the charges should be defined by the TEC track information from both hemispheres.

If there is no identified muon but each hemisphere has exactly one track, the charge can be estimated from the both TEC curvatures weighted by their TEC resolutions:

$$q_1 = -q_2 = sign[\frac{C_1}{\delta C_1} - \frac{C_2}{\delta C_2}] \tag{7.9}$$

where $C_i = 1/P_{T,i}$ is the curvature of the track and δC_i is its resolution. For all the other events, charges are not assigned and they are to be used for the A_τ measurement only.

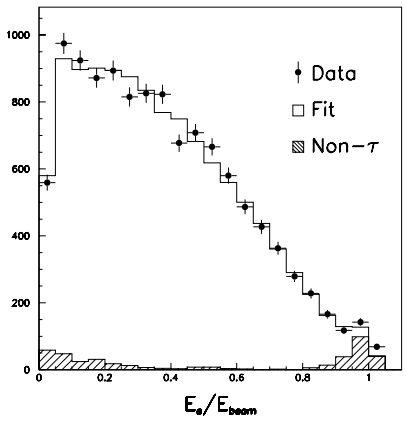

Figure 7.1: A cross-check of the measurement of τ polarization in $\tau^- \to e^-\overline{\nu_e}\nu_\tau$ channel. The $\mathcal{P}_\tau$ fit using the entire barrel region events is shown [49].

Systematics Coming from Charge Confusion The sign of $\cos\theta$ can be assigned in the wrong way due to charge confusion of the τ candidate, causing the event to migrate from one $\cos\theta$ bin to the opposite bin. Since the P_T distribution depends on the polarization, the charge confusion depends on the polarization also and results as the migration rate depending on the polarization. Hence, a correction should be applied in the fit of the polarization due to the different migration rate between the data sample and the MC sample. The detailed correction procedure is explained in Reference [45].

7.3 The Measurement of τ Polarization

7.3.1 Fitting in $\tau^- \to \mathrm{e}^-\overline{\nu}_\mathrm{e}\nu_\tau$

The events are selected with the requirement explained in Section 5.2.3. The 1-dimensional fit variable is defined as E_e/E_{beam}. Considering the detector resolution, the fit range is set between 0 to 1.1, with 22 equal-sized bins. The non-τ background sample is made in the following way and fitted together with the helicity positive and negative MC events.

- Bhabha sample: The selection requirement is the same as the data sample except that the ratio of the total BGO calorimeter energy over the total beam energy should be between 0.77 and 0.89.

- Two photon interaction sample: The selection requirement is the same as the data sample except that the angle between the electron candidate and the opposite hemisphere particle is at the range of 1.7 and 2.7 rad.

To suppress the small contribution from the real τ events in the non-τ background samples, they are subtracted by the τ MC events survived the above requirement. The normalization of the Bhabha sample is a free parameter in the fit. That of the two photon sample is estimated by the fact that the distribution of the two photon interactions is flat over the angle between the electron candidate and the opposite hemisphere particle.

The systematic error coming from the calibration is estimated by varying the energy scale of the BGO calorimeter by the accuracy mentioned in Section 6.1. The systematics coming from non-τ background is estimated by varying the normalization by 20%.

7.3.2 Fitting in $\tau^- \to \mu^- \overline{\nu}_\mu \nu_\tau$

The events are selected with the requirement explained in Section 5.2.5. As in the case of $\tau^- \to \mu^- \overline{\nu}_\mu \nu_\tau$ channel, the 1-dimensional variable E_μ / E_{beam} is used in the fit with 22 equal-size bins ranged between 0 and 1.1. The non-τ background sample for the fit is made in the following way.

- Dimuon sample: The opposite hemisphere has an identified muon also. The total energy of two muons should be more than 55 GeV. Other selection requirements are the same as that of the data sample.

- Two photon interaction sample: The selection requirement is the same as the data sample except that the angle between the muon candidate and the opposite hemisphere particle is at the range of 1.8 and 2.7 rad.

- Cosmic event sample: The DCA reconstructed from TEC hits is at the range of 5 and 15 cm. All the other requirements are the same as the data sample.

Normalization of the dimuon background sample and the two photon interaction background sample is done in the same way as $\tau^- \to e^- \overline{\nu}_e \nu_\tau$ case. Normalization

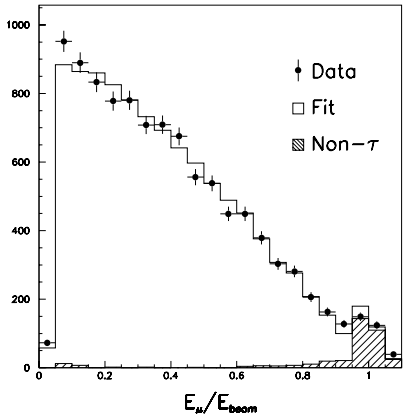

Figure 7.2: A cross-check of the measurement of τ polarization in $\tau^- \to \mu^- \overline{\nu_\mu} \nu_\tau$ channel. The $\mathcal{P}_\tau$ fit using the entire barrel region events is shown [49].

of the cosmic event sample is estimated by the fact that the distribution of the cosmic events with respect to the DCA is almost flat.

The systematic error coming from the calibration is estimated by varying the energy scale of the muon spectrometer by the accuracy mentioned in Section 6.2. Charge confusion is negligible in this decay mode. The systematic error coming from non-τ background is estimated from varying the normalization by 20%.

7.3.3 Fitting in $\tau^- \to \pi^- \nu_\tau$

Considering the detector resolution for the charged pion energy, the 1-dimensional fit is done with unequal-sized bins. The lower and upper limits of each bin are adjusted such that even numbers of charged pion candidates are distributed over 16 bins. The charged pion energy of up to 70 GeV is accepted in the fit. The two photon interaction background sample and the cosmic event background sample are obtained in the similar way explained in the previous sections. The normalizations of the Bhabha and the dimuon background samples are estimated from the corresponding MC events.

The systematic error coming from the calibrations is estimated by varying the gains in the BGO and the hadron calorimeter and the momentum scale of the

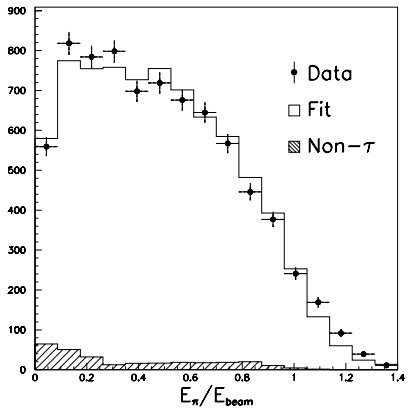

Figure 7.3: A cross-check of the measurement of τ polarization in $\tau^- \to \pi^-\nu_\tau$ channel. The $\mathcal{P}_\tau$ fit using the entire barrel region events is shown [49].

TEC. The systematics coming from the size of the non-τ background events is estimated by varying their normalization by 20%.

7.3.4 Fitting in $\tau^- \to \rho^-\nu_\tau$

Fitting in this channel is done with two kinematic variables, $\cos\theta^*$ and $\cos\psi^*$ with 15×10 bins [21]. The meaning of variables is explained in Section 3.3. The non-τ background sample is made in the following way:

- Bhabha sample: Opposite hemisphere has an identified electron with the energy more than 43 GeV. All the other selection rules are the same as those of the data sample.
- dimuon sample: Opposite hemisphere has an identified muon with the energy more than 43 GeV.

The normalization of the background sample is estimated from the corresponding MC events.

The systematic error coming from the calibration is estimated by varying the gain in the BGO and the hadron calorimeter, the momentum scale in the TEC for

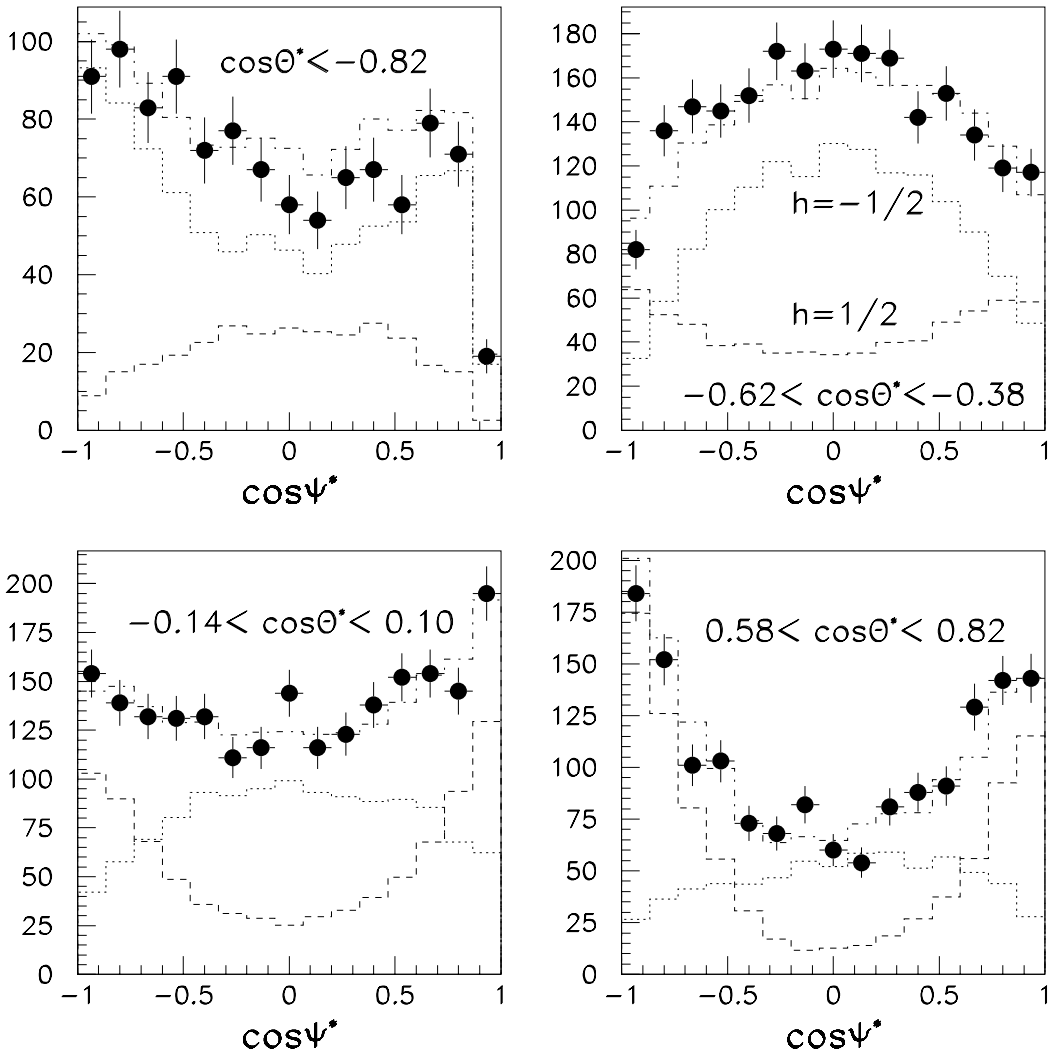

Figure 7.4: A cross-check of the measurement of τ polarization in $\tau^- \to \rho^-\nu_\tau$ channel, in 4 slices of $\cos\theta^*$. The $\mathcal{P}_\tau$ fitted from the entire barrel region events.

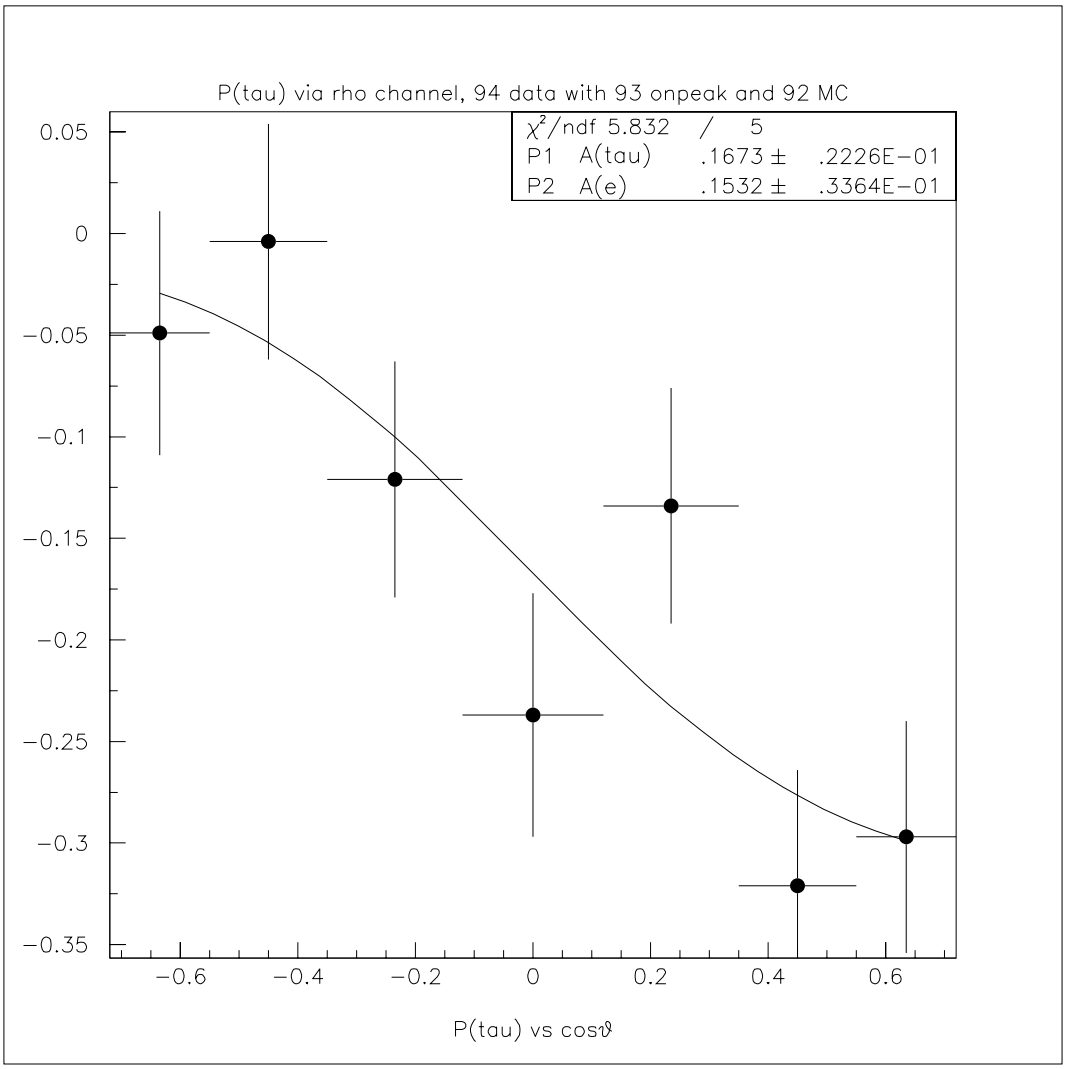

Figure 7.5: $\mathcal{A}_\tau$ and $\mathcal{A}_e$ from $\tau^- \to \rho^- \nu_\tau$ channel.

the charged pion and by varying the energy scale in the BGO calorimeter for the neutrals. The systematic error coming from the non-τ background is estimated in the same way as in other decay channels. Figure 7.4 is a cross-check of fitting in $\cos\theta^*$ and $\cos\psi^*$, where all the barrel events are used in the fit. Figure 7.5 is an example of the asymmetry fit, where events from $\tau^- \to \rho^-\nu_\tau$ used as the data points.

7.3.5 Fitting in $\tau^- \to a_1^-\nu_\tau$

To reduce the uncertainties coming from the mass parameters of a_1, the optimal variable [24] is used in the 1-dimensional fit for this channel. Non-τ background is negligible in this mode [43].

7.4 The Measurement of $\mathcal{A}_e$ and $\mathcal{A}_\tau$

After $\mathcal{P}_\tau$ from each decay channel is obtained, the final fit for the asymmetry is done. The central value in each $\cos\theta_{thrust}$ is the weighted mean of contributions from the four τ decay channels. The fitted result from $\tau^- \to a_1^-\nu_\tau$ is not included in the final fit[3]. The systematic errors from four channels are propagated to the final fit. The final systematic error is estimated about the same as the previous L3 measurement [54]. Table 7.4 shows the systematics from each source.

Handling of the correlated statistical errors Until now, we have handled two hemispheres separately in fitting of the polarization in each τ decay channel. In fact, the spin of τ in one hemisphere is correlated with the spin of τ in the other hemisphere. If we combine the fitted result obtained from each channel without considering correlation between two hemispheres, the final statistical error will be underestimated. Hence, we need reweighted averages and statistical errors including the correlation to perform the final fit.

Let's assume we observed $\tau \to \pi\nu_\tau$ events with a polarization measurement x in one hemisphere and $\tau \to \rho\nu_\tau$ with a polarization measurement y in the other hemisphere. Instead of a simple probability distribution, we have to consider the binomial distribution of two observables with correlation coefficient ρ and measured

[3]The result from this channel using '94 data is different from the previous L3 measurement [54] by several σs. It is thought that there is a error in the computer codes.

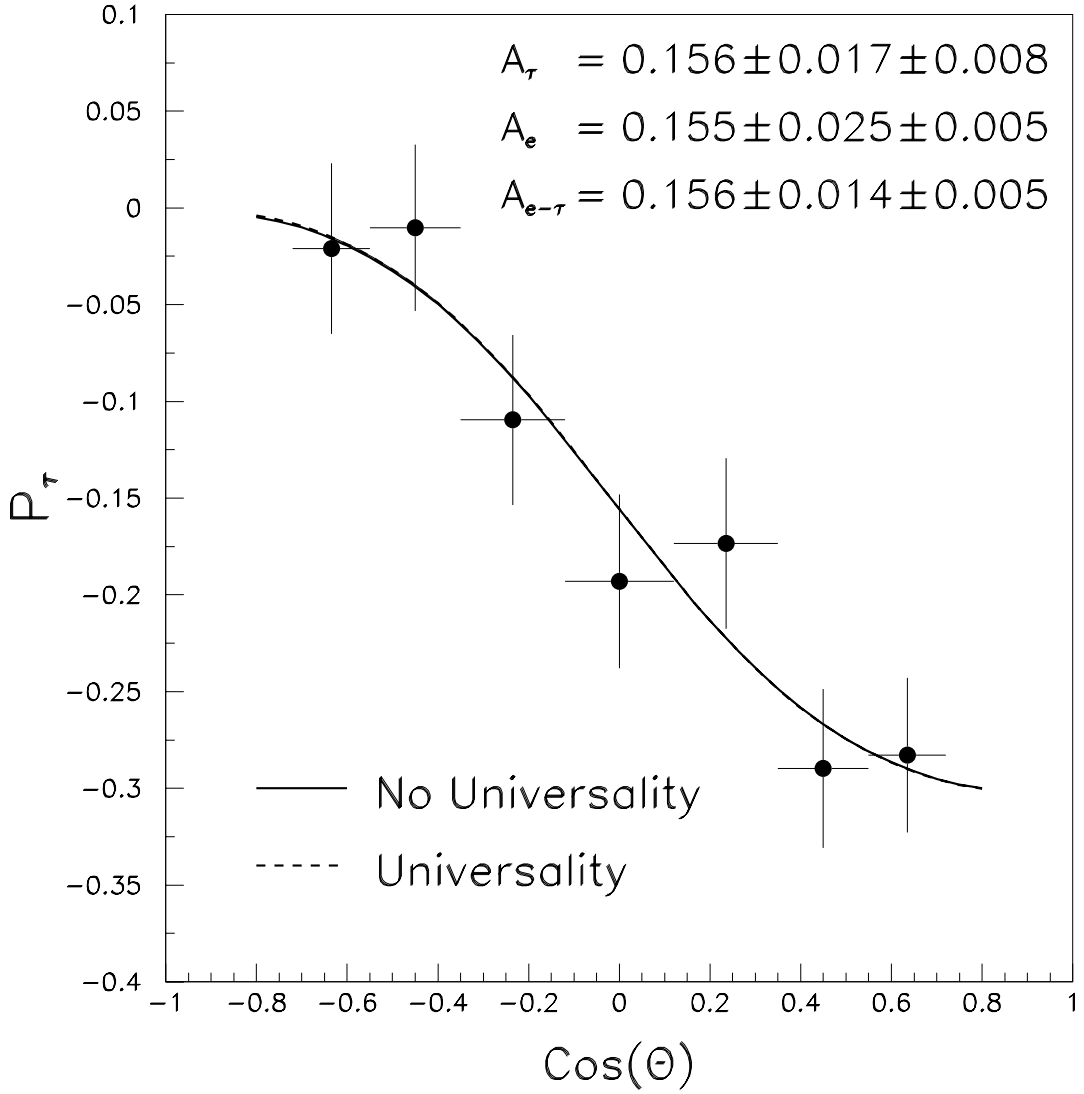

Figure 7.6: The final $\mathcal{A}_\tau$ and $\mathcal{A}_e$ from '94 data.

$\cos\theta$ range	$\mathcal{P}_\tau$	$\delta\mathcal{P}_\tau^{\rm QED}$	$\Delta\mathcal{P}_\tau^{\rm stat}$	$\Delta\mathcal{P}_\tau^{\rm sel}$	$\Delta\mathcal{P}_\tau^{\rm bg}$	$\Delta\mathcal{P}_\tau^{\rm cal}$	$\Delta\mathcal{P}_\tau^{\rm chrg}$	$\Delta\mathcal{P}_\tau^{\rm theor}$
$[-0.72,-0.55]$	-0.048	$+0.0000$	0.040	0.0045	0.0042	0.0126	0.00 21	0.0007
$[-0.55,-0.35]$	-0.002	-0.0010	0.038	0.0045	0.0042	0.0128	0.00 21	0.0007
$[-0.35,-0.12]$	-0.082	-0.0027	0.039	0.0046	0.0043	0.0129	0.00 15	0.0007
$[-0.12,+0.12]$	-0.112	-0.0045	0.036	0.0048	0.0038	0.0137	0.00 00	0.0007
$[+0.12,+0.35]$	-0.201	-0.0054	0.039	0.0046	0.0040	0.0127	0.00 15	0.0007
$[+0.35,+0.55]$	-0.308	-0.0054	0.037	0.0045	0.0042	0.0128	0.00 21	0.0007
$[+0.55,+0.72]$	-0.275	-0.0053	0.039	0.0045	0.0045	0.0130	0.00 21	0.0007
no charge	-0.143	-0.0045	0.032	0.0048	0.0046	0.0100	0.00 00	0.0007

Table 7.1: The combined dependence of $\mathcal{P}_\tau$ on $\cos\theta_{thrust}$. $\delta\mathcal{P}_\tau^{\rm QED}$ represents the radiative correction. The correction is to be added to the measured values of $\mathcal{P}_\tau$.

values x and y,

$$P(x,y) = \mathcal{N}\exp\{-\frac{1}{2(1-\rho^2)}[(\frac{x-\mu}{\sigma_x})^2 + (\frac{y-\mu}{\sigma_y})^2 - 2\rho(\frac{x-\mu}{\sigma_x})(\frac{y-\mu}{\sigma_y})]\}, \quad (7.10)$$

where μ is the expected value and $\mathcal{N}$ is the normalization. The estimation of μ can be obtained by minimizing $-\ln P(x,y)$ as

$$\mu = (\frac{1}{\sigma_x^2} + \frac{1}{\sigma_y^2} - \frac{2\rho}{\sigma_x\sigma_y})^{-1}\{\frac{x}{\sigma_x^2} + \frac{y}{\sigma_y^2} - \frac{\rho}{\sigma_x\sigma_y}(x+y)\}. \quad (7.11)$$

The combined statistical error is obtained from the second derivative of $-\ln P(x,y)$ as

$$\frac{1}{\sigma_{\pi,\rho}^2} = \frac{1}{1-\rho^2}(\frac{1}{\sigma_x^2} + \frac{1}{\sigma_y^2} - \frac{2\rho}{\sigma_x\sigma_y}). \quad (7.12)$$

σ_x can be estimated from the statistical error we obtained in the $\tau \to \pi\nu_\tau$ mode using all the π events. If the branching ratio and selection efficiency of $\tau \to \rho\nu_\tau$ is B_ρ and ϵ_ρ,

$$\sigma_x \sim \frac{\sigma_\pi}{\sqrt{B_\rho\epsilon_\rho}}. \quad (7.13)$$

Similarly, σ_y is estimated as $\sigma_\rho/\sqrt{B_\pi\epsilon_\pi}$. The correlation coefficient ρ is estimated from a simulation.

If the τ decay in the opposite hemisphere is not identified, there is no correlation between two hemispheres. For example, if we identified $\tau \to \pi\nu_\tau$ in one hemisphere but nothing interesting is selected in the other hemisphere, the corresponding error is estimated as

$$\sigma_{\pi,X} \sim \frac{\sigma_\pi}{\sqrt{1 - 2B_\pi\epsilon_\pi - \sum_{j\neq\pi} B_j\epsilon_j}}. \tag{7.14}$$

The number of particles selected in more than one τ decay mode at the same time is not so large, so we can obtain the combined statistical error using generalization of Equations 7.12 and 7.14 for all the decay modes.

$$\frac{1}{\sigma^2} = \sum_i^N \sum_{j=i}^N \frac{1}{\sigma_{i,j}^2} + \sum_i^N \frac{1}{\sigma_{i,X}^2}, \tag{7.15}$$

where N is the number of τ decay modes.

The QED Correction The QED correction is done with the package **ZFITTER** [52], which does the analytical calculation including the Z^0-photon interference, the photon exchange term and the radiative correction. More detailed explanation can be found in Reference [53].

Chapter 8

Conclusion and Discussion

8.1 Conclusion

With a data sample of 58,000 $e^+e^- \to \tau^-\tau^+(\gamma)$ collected in '94, we measured

$$\begin{aligned} \mathcal{A}_\tau &= 0.156 \pm 0.017 \pm 0.008 \\ \mathcal{A}_e &= 0.155 \pm 0.025 \pm 0.005, \end{aligned} \tag{8.1}$$

where the first error is statistical and the second one is systematic. The numbers are consistent with the lepton universality hypothesis. Assuming lepton universality, we obtain

$$\mathcal{A}_{e-\tau} = 0.156 \pm 0.014 \pm 0.005. \tag{8.2}$$

The numbers in Equations 8.1 and 8.2 are consistent with the previous L3 measurement from '90-'93 data [54]. Combining the '94 result with the '90-'93 measurement, we obtain $\mathcal{A}_\tau$ and $\mathcal{A}_e$ with the improved statistical errors as follows:

$$\begin{aligned} \mathcal{A}_\tau &= 0.152 \pm 0.010 \pm 0.009 \\ \mathcal{A}_e &= 0.156 \pm 0.016 \pm 0.005. \end{aligned} \tag{8.3}$$

From Equation 8.3, the ratios of the vector to the axial-vector weak neutral coupling constants for electrons and taus as the combined '90-'94 measurement are deduced as:

$$\begin{aligned} g_V^e/g_A^e &= 0.0787 \pm 0.0078 \pm 0.0025 \\ g_V^\tau/g_A^\tau &= 0.0763 \pm 0.0051 \pm 0.0044. \end{aligned} \tag{8.4}$$

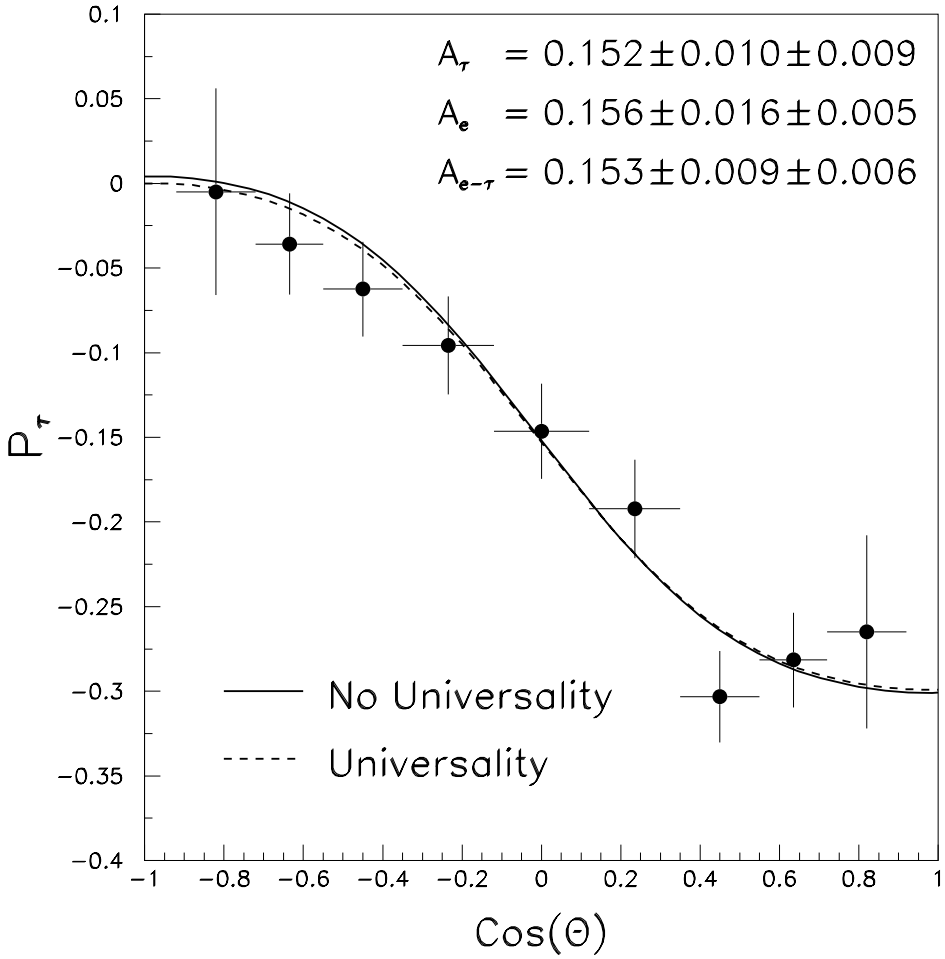

Figure 8.1: $\mathcal{P}_{\tau^-}(\cos\theta)$ from the '90-'94 combined L3 result, together with the fitted curves for $\mathcal{A}_\tau$, $\mathcal{A}_e$ and $\mathcal{A}_{e-\tau}$. The QED correction by the **ZFITTER** program is already applied. The errors at the data points include the data and MC statistics, and the systematics.

Assuming lepton universality, we derive the ratio of the vector to the axial-vector weak neutral coupling constants and the effective electroweak mixing angle as follows:

$$g_V/g_A = 0.0770 \pm 0.0043 \pm 0.0031 \quad (8.5)$$
$$\sin^2\theta_w^{eff} = 0.2308 \pm 0.0013. \quad (8.6)$$

The numbers are consistent with the measurements by other experiments within the errors [55]. In Figure 8.1, $\mathcal{P}_{\tau^-}(\cos\theta)$ from the combined '90-'94 L3 result is shown as the data points, together with the fitted curves for $\mathcal{A}_\tau$, $\mathcal{A}_e$ and $\mathcal{A}_{e-\tau}$.

8.2 Discussion

We'd like to discuss the inclusion of the 3-prong decay mode of τ^- leptons in the polarization measurement. The promising mode in this particular analysis is the one in which a tau lepton decays into 3 charged pions, one neutrino and no neutral pion. The theory assumes that this decay proceeds via a_1^- resonance. Other 3-prong decay modes proceed via more complex pathways, involving several resonances. The theoretical predictions for their decay structure and the branching ratio haven't been solidified yet, makes them unsuitable for the polarization measurement. The pros and cons in analyzing $\tau^- \to a_1^-\nu_\tau \to 3\pi^-\nu_\tau$ are summarized in the following articles.

The Experimental Method As mentioned before, a_1^- decays either to three charged pions or to one charged pion and two neutral pions. The former is called the 3-prong decay mode and the letter is called the 1-prong decay mode of a_1^-. Besides the mass difference between the charged pion and the neutral pion, the same decay kinematics applies to both decay modes. Hence, the branching ratio of the two decay modes should be the same. It's reflected in tau lepton decay, where the branching ratios of $\tau^- \to \pi^-2\pi^0\nu_\tau$ and $\tau^- \to 3\pi^-\nu_\tau$ are about the same level [56].

The same polarization analyzer used in $\tau^- \to a_1^-\nu_\tau$ (1-prong) events can be used in $\tau^- \to 3\pi^-\nu_\tau$, with the same sensitivity to the polarization measurement. The use of the optimal variable [24] is recommended here also, since the problems of the a_1^- mass parameters and the a_1^- structure function are still there.

Reconstruction The reconstruction program used in the previous analysis is optimized for 1-prong decay channels of the tau lepton, with the emphasis on discriminating the neutral pions from the charged pions in the BGO calorimeter, so it does not behave well in case of 3-prong decay channels of the tau lepton. We need another reconstruction program, with emphasis of reconstructing multi-tracks in the central tracking system. The spatial resolution of the TEC system in $r-\phi$ coordinates is good. But the spatial resolution of the Z-chamber is 400 μm at best, when there is only one z cluster. The spatial resolution of the Z-chamber becomes worse when there are multiple hits clustered at the same area. Since the charged pions coming from a_1^- are boosted together, reconstructing is more difficult than in the case of hadronic decay of Z^0 particles.

One way to improve the situation is to include the z position of the track measured by the SMD. It will add more information in reconstructing the polar angle, $\cos\theta$, which is currently reconstructed by the linear fit between the fill vertex and the z coordinate measured by the Z-chamber. The resolution of the z coordinate measurement by the SMD is 25 μm, in contrast to the spread of the beam collision point in z direction, 2 cm. Much better spatial resolution of the SMD points makes it possible to reconstruct secondary a_1^- decay points, providing the better constraint for the final track reconstruction. Still there is a limit to this method. It requires reconstruction of the same number of clusters in the Z-chamber as the number of tracks found on the TEC $r-\phi$ plane. If less than 3 clusters are reconstructed in the Z-chamber, the tracks corresponding to the 3 charged pions will be assigned incorrect polar angles.

Selection The major background to $\tau^- \to 3\pi^-\nu_\tau$ is other 3-prong decay modes of the tau lepton, with $\tau^- \to 3\pi^-\pi^0\nu_\tau$ as the most prominent one. There are two ways to reject this background. The first one is counting the number of neutral clusters in the BGO calorimeter. This requires precise track reconstruction in the central tracking system. If something is wrong with the reconstruction, we will get the wrong impact point at the BGO calorimeter. Hence, some charged pion clusters in the BGO calorimeter can be misidentified as neutral clusters and selection efficiency will go down. The other way is making a Dalitz plot of the a_1^- candidates, that is, the plot of the total invariant mass of the 3 particle system versus the invariant mass of the unlikely signed charged particles. The total invariant mass should fall into the range of the a_1^- mass spectrum and the invariant mass of the unlikely signed charged particles should fall into the range of the ρ^0 mass spectrum. However, since

we are not sure of the a_1^- mass parameters, this can bias the selection.

Systematic Errors Even if we can perform the same fit procedure used in fitting $\tau^- \to a_1^- \nu_\tau$ (1-prong) events, some sources of the systematic errors are different from those of the 1-prong mode. First, if a_1^- decays in the 1-prong mode, the important source of the calibration error is the BGO calorimeter, where neutral pion energy is assigned and the gain constants for charged pions are selected. If a_1^- decays in the 3-prong mode, the momentum of the charged particles are determined mainly by the central tracking system, hence, the calibration error of the tracking system becomes important. Second, the major τ background in the 1-prong mode is $\tau^- \to \rho^- \nu_\tau$ while that in the 3-prong mode is expected to be $\tau^- \to 3\pi^-\pi^0\nu_\tau$. The different background would result as the different bias on the fit variables.

Conclusion If we have a reliable reconstruction program, we can obtain additional contribution from the $\tau^- \to 3\pi^-\nu_\tau$ channel to the τ polarization measurement. If selection efficiency of this channel is reasonable, the contribution will be about the same level as from a leptonic decay channel of the tau lepton. Therefore, we expect improvement of the statistical error in the polarization measurement. In addition, we can compare a_1^- mass parameters obtained from the 1-prong decay mode to those obtained from the 3-prong decay mode of a_1^- particles. It will provide an interesting checking point for the a_1^- structure function study.

The reliable reconstruction program will be also helpful in other analysis fields. For example, it can be used in the tau neutrino mass study, where sensitivity to the neutrino mass becomes larger as the number of tracks coming from tau decay increases.

Appendix A

Helicity

In this article, we'd like to compare the definition of handedness (chirality) to that of helicity. For convenience, particle fields will be represented by four-dimensional spinors. Let's assume ψ is a four-dimensional spinor with two-dimensional components, u and v,

$$\psi = \begin{pmatrix} u \\ v \end{pmatrix} \tag{A.1}$$

The left-handed and the right-handed components of ψ will be defined as,

$$\psi_L \equiv \frac{1}{2}(1-\gamma^5)\psi = \frac{1}{2}\left[\begin{pmatrix} I & 0 \\ 0 & I \end{pmatrix} - \begin{pmatrix} -I & 0 \\ 0 & I \end{pmatrix}\right]\psi = \begin{pmatrix} u \\ 0 \end{pmatrix} \tag{A.2}$$

$$\psi_R \equiv \frac{1}{2}(1+\gamma^5)\psi = \frac{1}{2}\left[\begin{pmatrix} I & 0 \\ 0 & I \end{pmatrix} + \begin{pmatrix} -I & 0 \\ 0 & I \end{pmatrix}\right]\psi = \begin{pmatrix} 0 \\ v \end{pmatrix}. \tag{A.3}$$

The left-handed component depends only on u and the right-handed one depends only on v.

Now in the Weyl representation, the equation of motion for a free particle is written as,

$$\begin{pmatrix} -\vec{\sigma}\cdot\vec{p} & m \\ m & \vec{\sigma}\cdot\vec{p} \end{pmatrix}\psi = E\,\psi. \tag{A.4}$$

where $\vec{\sigma}$ are the Pauli matrices, m is the mass of the particle, $\vec{p}$ is its momentum and E is its energy. We can break down Equation A.4 into two component representations and rewrite it using u and v as,

$$\begin{aligned} -\vec{\sigma}\cdot\vec{p}u + mv &= Eu \\ mu + \vec{\sigma}\cdot\vec{p}v &= Ev. \end{aligned} \tag{A.5}$$

Sometimes in experiments, the mass of a particle is very small compared to its momentum. In such a case, we can simplify Equation A.5 by ignoring the mass term as follows:

$$\begin{aligned} \vec{\sigma} \cdot \hat{p} u &= -u \\ \vec{\sigma} \cdot \hat{p} v &= v, \end{aligned} \tag{A.6}$$

where $\hat{p}$ is the unit vector in the direction of the particle momentum. Equation A.6 indicates that in the massless limit, u and v or the corresponding parts of ψ_L and ψ_R become the eigenstates of the helicity operator, $\vec{\sigma} \cdot \hat{p}$. The physical meaning of the helicity operator is the projection of particle spin on the particle momentum. If a particle is in a negative helicity eigenstate, like u in Equation A.6, the direction of the particle spin is opposite to its momentum direction. If the particle is in a positive helicity eigenstate, like v in Equation A.6, the direction of the spin is the same as its momentum.

The mass of a tau lepton (1.78 GeV) generated in $Z^0 \rightarrow \tau^+\tau^-$ at LEP phase I is small compared to its energy, 45.6 GeV. Hence, it is possible to ignore the mass of tau leptons and measure the ratio of handedness by counting the ratio of helicity positive states over helicity negative states in the tau leptons as a good approximation.

Appendix B

The TEC Momentum Resolution with SMD Hits

In '94, the SMD was fully operational for most of the data acquisition periods. We studied the effect of SMD hits in the TEC resolution of the inverse transverse momentum ($1/P_T$) for the '94 data. In the first order, resolution of $1/P_T$ does not depend on P_T itself. Since the error on $1/P_T$ measured from muon spectrometer information is negligible with respect to that from the TEC measurement only, the resolution is computed by making a comparison between two values. To see the effect of SMD hits, four different resolution functions calculated by the corresponding TEC refit methods are shown in Figure B.1.

case 1 The track is refitted with TEC hits only, neither SMD hits nor the fill vertex are included in the fit.

case 2 In addition to TEC hits, the fill vertex is attached at the track.

case 3 In addition to TEC hits, SMD hits are included in the fit.

case 4 Both SMD hits and the fill vertex are included in the fit as well as TEC hits.

Since the purpose of the study is to provide a suitable refit method for the tau analysis group, the weight of the fill vertex is given by the quadruple addition of the tau decay length (0.1mm) and the size of the fill vertices. The TEC calibration and SMD alignment constants inserted into the database on 95.10.30 are used.

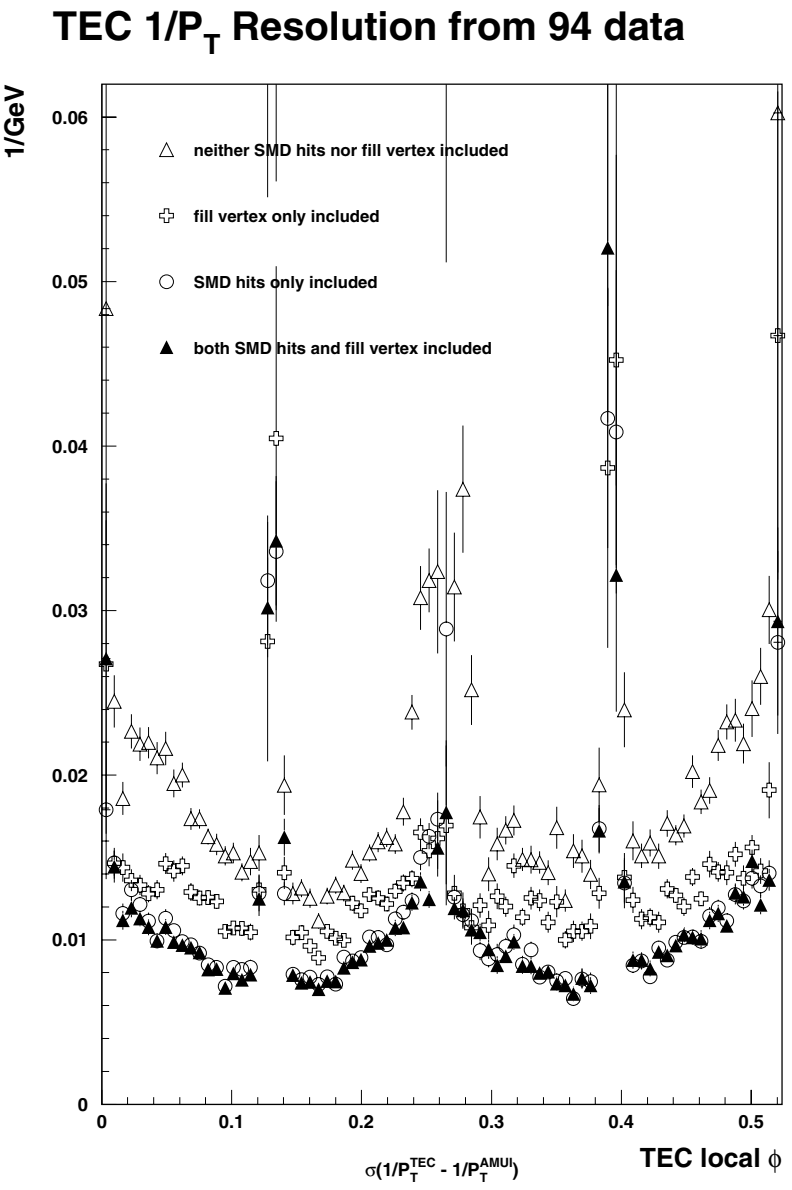

Figure B.1: TEC momentum resolution versus the local TEC ϕ with various reconstruction options.

A sample of good dimuon events is selected to check the resolution. The major selection criteria are as follows:

- Both charged tracks should be in the TEC barrel region, $|\cos\theta_{TEC}| < 0.70$, the total number of TEC hits should be more than 46 per track and there should be at least one inner TEC hit for each track.
- Both charged tracks should have hits in the P-chamber of the muon spectrometer. And the interesting track should have 3 P-chamber hits.
- Particle energy computed from muon spectrometer information for both charged tracks should be comparable to the incident beam energy, between 30 GeV and 71.25 GeV.
- The energy profile deposited in the BGO and hadron calorimeters and the muon filter should be interpretable as that of a minimum ionizing particle.

It is clear that including SMD hits in the track reconstruction improves $1/P_T$ resolution substantially. Since we use the momentum measured by the TEC system to determine energy of a charged pion, including SMD hits in the reconstruction would improve the systematic error in the measurement of tau polarization.

$1/P_T$ resolution of tracks going into the TEC endcap region is checked by the counting method [45] using a Bhabha sample. The last hit of the TEC track located less than 2 cm of the TEC endflanges is excluded from the reconstruction, since this region is not calibrated well. The resolution becomes worse as $|\cos\theta_{TEC}|$ becomes bigger, since there are less TEC hits generated by the track. It is found that the part of the $1/P_T$ resolution function depending on the polar angle, $|\cos\theta_{TEC}|$, made by the previous study without SMD hits [45], can be used for the tracks with SMD hits without a big modification.

Bibliography

[1] Nachtmann, O., *Elementary Particle Physics, Concepts and Phenomena.* Springer-Verlag, 1990.

[2] Bailin, D. and A. Love, *Introduction to Gauge Field Theory* (Adam Hilger, 1986)

[3] Halzen, F. and A.D. Martin, *Quarks and Leptons: An Introductory Course in Modern Particle Physics* (John Wiley & Sons, 1984)

[4] Fermi, E., *Ricera Scient.* **2**, issue 12 (1933)

[5] Weyl, H., *Z. Phys.* **56**, 330 (1929)

[6] Lee, T.D. and C.N. Yang, *Phys. Rev.* **104**, 254 (1956)

[7] For the electron neutrino helicity, look at Goldhaber, M. et al., *Phys. Rev.* **109**, 1015 (1958)

[8] Glashow, S.L., *Nucl. Phys.* **22**, 579 (1961)

[9] Weinburg, S., *Phys. Rev. Lett.* **19** 1264 (1967)

[10] Salam, A., in *Proc. 8th Nobel Symposium*, edited by N. Svartholm (Almquist and Wiskell, 1968)

[11] Higgs, P.W., *Phys. Lett.* **12**, 132 (1964)

[12] *Z Physics at LEP, Volume 1.*, 55 edited by G. Altarelli, R. Kleiss and C. VerzegnassI (CERN 89-08, 1989)

[13] *Z Physics at LEP, Volume 1.*, 203 edited by G. Altarelli, R. Kleiss and C. Verzegnassi (CERN 89-08, 1989)

[14] *Z physics at LEP, Volume 1.*, 235 edited by G. Altarelli, R. Kleiss and C. Verzegnassi (CERN 89-08, 1989)

[15] Altarelli, G. et al., in *Physics at LEP, Vol. 1*, 1 (CERN 86-02, 1986)

[16] Dydak, F. et al., *ECFA Workshop on LEP 200, Vol. 1*, 157 (CERN 87-08, 1987)

[17] Tsai, Y.-S., *Phys. Rev.* **D4**, 2841 (1971)

[18] Perl, M.L., *The Discovery of the Tau Lepton*, (SLAC-PUB-6584, 1994)

[19] ARGUS Collaboration, H. Albrecht et al., *Phys. Lett.* **B316**, 608, (1993); ALEPH Collaboration, D. Buscolic et al., *Phys. Lett.* **B346**, 379 (1995)

[20] Rougé, A., *Tau Decays as Polarization Analysers* in Proceedings of the Workshop on Tau Lepton Physics, Orsay, France, Edited by M. Davier and B. Jean-Marie, Sep. (1990)

[21] Hagiwara, K., A. D. Martin and D. Zeppenfeld, *Phys. Lett.* **B235**, 198 (1990); Rougé, A., *Z. Phys.* **C48**, 75 (1990)

[22] The OPAL Collaboration, *Measurement of the Hadronic Decay Current in* $\tau^- \to \pi^-\pi^-\pi^+\nu_\tau$, CERN-PPE/95-022, (1995) March 2

[23] Kühn, J. H. and E. Mirkes, *Phys. Lett.* **B286**, 381 (1992); Kühn, J. H. and E. Mirkes, *Zeit. Phys.* **C56**, 661 (1992)

[24] Davier, M. et al., *The Optimal Method for the Measurement of Tau Polarization*, X LPNHE 92-22 (1992)

[25] Most of the detector figures are obtained from the public directory of the L3 computer network.

[26] L3 Collaboration, *The Construction of the L3 Experiment*, *Nucl. Instrum. Methods* **A289**, 35 (1990)

[27] L3 Collaboration, *Results from the L3 Experiment at LEP*, *Phys. Rep.* **236** (1993)

[28] Anderhub, H. et al., *Nucl. Instrum. Methods* **A235**, 267 (1985)

[29] Beissel, F. et al., *Nucl. Instrum. Methods* **A332**, 33 (1992)

[30] Acciarri, M. et al., *Nucl. Instrum. Methods* **A351**, 300 (1994)

[31] Sumner, B. et al., *Nucl. Instrum. Methods* **A265**, 252 (1988)

[32] Bay, A. et al., UGVA-DPNC 1992/01-150 (1992)

[33] Adriani, O. et al., *Nucl. Instrum. Methods* **A302**, 53 (1991)

[34] Adeva, B. et al., *Nucl. Instrum. Methods* **A277**, 187 (1989)

[35] L3 FB Muon group, *The Forward Muon Detector of L3*, (CERN-PPE/) *to be published.*

[36] Cai, Xudong, Doctoral thesis, *Contribution à l'élaboration et à la mise en oeuvre du système de déclenchement et d'acquisition de l'expérience L3 au LEP*, (1994)

[37] Dalgeir, G. et al., *California Institute of Technology, Proposal for Grant Renewal for FY 95-99 and Report of Research Accomplishments and Future Goals in High Energy Physics (L3/CMS section)*, (1994)

[38] There are several of them. The ones used to generate $\tau^+\tau^-$ MC events is: Jadach, S. et al., *Comput. Phys. Comm.* **60**, 276 (1991); Jezabek, M. et al., *Comput. Phys. Comm.* **70**, 69(1992); Jadach, S. et al., *Comput. Phys. Comm.* **76**, 361 (1993)

[39] Brun, R. et al., *GEANT 3* CERN DD/EE/84-1, Sep. (1987)

[40] Following people contributed for the alignment and reconstruction method used by the L3 tau group in the τ polarization analysis: (in alphabetical order) P. Garcia, P. Kapinos, D. Kim, A. Kunin, T. Paul, I. Scott, I. Vorobiev

[41] Jézéquel, S., Karyotakis, Y. L3 Note 1272 (1992)

[42] Lonnblad, L., et al., *JETNET 3.0 - A Versatile Artificial Neural Network Package*, LU-TP 93-29

[43] Shukla, J., Ph.D. Thesis, Carnegie Mellon University (1994)

[44] Private communication with Igor Vorobiev.

[45] Paul, T.C., Ph.D. Thesis (1994)

[46] Scott, I.J., Ph.D. Thesis, Harvard University (1993)

[47] Adriani, O. et al., *A Measurement of τ Polarization*, L3 internal note 1637, Aug. (1994)

[48] James, F. *MINUIT Reference Manual*, CERN Program Library, long writeup D506 (1992)

[49] Courtesy by J. Gerald and A. Gougas

[50] Kühn, J. H. and E. Mirkes, *Z. Phys*, **C56**, 661 (1992); Isgur, N., et al., *Phys. Rev.*, bf D39, 1357 (1989); Feindt, M., *Z. Phys.*, **C48**, 681 (1990)

[51] Finkemeir, M., Ph.D. Thesis, University of Karlsruhe (1994); Privitera, P., *Structure functions in $\tau \to 3\pi\nu_\tau$ and the τ polarization measurement* , IEKP-KA/93-02, (1993)

[52] Bardin, D. et al., *FORTRAN package ZFITTER*, CERN-TH 6443/92; *Z. Phys.* **C 44**, 493 (1989); *Nucl. Phys.* **B 351**, 1 (1991); *Phys. Lett.* **B 255**, 290 (1991)

[53] Kirsch, S., Ph.D. Thesis *Neutral Current Physics with τ Leptons using the L3 Detector at LEP*, University of Berlin (1994); Internal Report DESY-Zeuten 94-04 (1994)

[54] L3 Collaboration, M. Acciarri et al., *Phys. Lett.* **B341**, 245 (1994); L3 Collaboraton, O. Adriani et al., *Phys. Lett.* **B294**, 466 (1994)

[55] The LEP Electroweak Working Group and the SLD Heavy Flavor Group, *A Combination of Preliminary LEP and SLD Electroweak Measurements and Constraints on the Standard Model*, LEPEWWG/96-02,ALEPH 96-107 PHYSICS 96-98, DELPHI 96-121 PHYS 631, L3 Note 1975, OPAL Technical Note TN 309, SLD Physics Note 52 (1996)

[56] Gentile, S. and M. Pohl, *Physics of Tau Leptons*, CERN-PPE/95-147 (1995)

[57] Particle Data Group, *Review of Particle Properties, Phys. Rev.* **D50**, 1173 (1994)

[58] Lamport, L., *LaTeX, User's guide & Reference Manual* (Addison-Wesley Publishing Company, 1986)

Vita

Doris Yangsoo Kim was born July 22, 1966, in Berkeley, California. She finished her basic education in Seoul, Korea. She got her Bachelor of Science degree at Seoul National University in February, 1989 and got her Master of Science degree at the same university in February, 1991, with a thesis in the field of theoretical high energy physics. She began her graduate study at the Johns Hopkins University, Baltimore, Maryland, in September, 1991 under Prof. Peter H. Fisher. In February, 1993, she moved to Geneva, Switzerland to participate in the L3 experiment at LEP and obtained her Doctor of Philosophy degree in October, 1996 under Prof. Aihud Pevsner.